# HEAT TRANSFER CHARACTERISTICS IN FILM COOLING APPLICATIONS

By

Dragos N. Licu

M. Sc. (Faculty of Aircraft) Polytechnic Institute of Bucharest

A THESIS SUBMITTED IN PARTIAL FULFILLMENT OF

THE REQUIREMENTS FOR THE DEGREE OF

DOCTOR OF PHILOSOPHY

in

THE FACULTY OF GRADUATE STUDIES

MECHANICAL ENGINEERING

We accept this thesis as conforming

to the required standard

THE UNIVERSITY OF BRITISH COLUMBIA

October 1998

In presenting this thesis in partial fulfilment of the requirements for an advanced degree at the University of British Columbia, I agree that the Library shall make it freely available for reference and study. I further agree that permission for extensive copying of this thesis for scholarly purposes may be granted by the head of my department or by his or her representatives. It is understood that copying or publication of this thesis for financial gain shall not be allowed without my written permission.

Mechanical Engineering
The University of British Columbia
2324 Main Mall
Vancouver, Canada
V6T 1Z4

Date: Oct. 6, 1998

# Abstract

The leading edge region of gas turbine blades and vanes experiences high thermal and mechanical stresses and has to be properly cooled. External cooling of the leading edge region is typically achieved by a film cooling technique. An investigation into the film cooling effectiveness of three different large scale leading edge geometries is presented in this study. One of the geometries investigated represents an original design and is an example of an improved film cooling layout. All geometries used have four rows of cooling holes placed symmetrically about the geometrical leading edge, but the layout of the cooling holes is different from one leading edge geometry to another. A broad range of variables is considered including mass flow ratio, coolant density, and jet Reynolds number. Film cooling effectiveness measurements were made in a low speed wind tunnel environment using a flame ionization detector technique and the mass/heat transfer analogy. These measurements significantly extend the insight into the effects of hole geometry on the film cooling characteristics of the leading edge of turbine blades and provide new data for design purposes.

The effect of geometry is more important for the case of double row injection where spanwise-averaged film cooling effectiveness is improved by the use of compound angle holes. The spanwise-averaged film cooling effectiveness is higher at lower mass flow ratios and decreases typically as the mass flow ratio increases. At higher mass flow ratios, the newly designed leading edge geometry produces higher spanwise-averaged film cooling effectiveness than the other two geometries investigated thus providing the necessary backflow margin at operating conditions more relevant to gas turbine use.

For the case of single row injection, the effects of geometry scale reasonably well when the

local mass flow ratio is used in the analysis of the spanwise-averaged film cooling effectiveness immediately downstream of the injection holes. The local momentum flux ratio is a more appropriate scaling parameter when coolants with different densities are used.

A film cooling effectiveness correlation was also developed for one of the geometries investigated based on an area-averaged film cooling effectiveness and on a newly defined blowing parameter. This correlation accounts implicitly for the particular geometrical layout used and explicitly for the main injection parameters investigated. The results can be now more directly used in existing design procedures.

A new experimental technique based on wide-band liquid crystal thermography and transient one-dimensional heat conduction has been developed and implemented. The technique combines a real-time, true colour imaging system with the use of a wide-band liquid crystal and multiple event sampling for the simultaneous determination of the film cooling effectiveness and heat transfer coefficient from one transient test. A comparison of different image capture techniques is also presented and computer codes are developed for data processing.

For a test case of compound angle square jets in a crossflow, very good agreement was obtained between the film cooling effectiveness calculated from the transient heat transfer experiments and the film cooling effectiveness measured in isothermal mass transfer experiments using a flame ionization detector technique. This new approach has been developed as a major part of this thesis and represents a significant contribution to the use of liquid crystal thermography in film cooling applications.

# Contents

# List of Figures

# List of Symbols

| | |
|---|---|
| $C$ | Concentration, mass fraction |
| $C_p$ | Pressure coefficient $\left(= \frac{p_\theta - p_\infty}{\frac{1}{2}\rho_\infty U_\infty^2}\right)$ |
| $D$ | Diameter of the leading edge |
| $D_{AB}$ | Mass diffusivity |
| $E$ | Flame ionization detector output voltage |
| $Gr$ | Grashof number $\left(= \frac{gL^3(T_w - T_\infty)}{\nu^2 T_\infty}$ for a perfect gas $\right)$ |
| $I$ | Jet-to-crossflow momentum flux ratio $\left(= \frac{\rho_2 U_2^2}{\rho_\infty U_\infty^2}\right)$ |
| $I_\theta$ | Local momentum flux ratio $\left(= \frac{\rho_2 U_2^2}{\rho_\infty U_\theta^2}\right)$ |
| $L$ | Characteristic length |
| $Le$ | Lewis number $(= \frac{Sc}{Pr} = \frac{\alpha}{D_{AB}})$ |
| $M$ | Jet-to-crossflow mass flow ratio $\left(= \frac{\rho_2 U_2}{\rho_\infty U_\infty}\right)$ |
| $M_\theta$ | Local mass flow ratio $\left(= \frac{\rho_2 U_2}{\rho_\infty U_\theta}\right)$ |
| $N$ | Number of data points in a sample |
| $Pr$ | Prandtl number $(= \frac{\nu}{\alpha})$ |
| $Q$ | Flow rate |
| $Re$ | Reynolds number $(= \frac{Ud}{\nu})$ |
| $S$ | Spanwise distance covered by the sampling probes |
| $S_{ar}$ | Spanwise spacing of holes in adjacent rows |
| $S_{LE}$ | Spanwise spacing of holes in adjacent rows about the stagnation line |
| $S_r$ | Spanwise spacing of holes in a row |
| $Sc$ | Schmidt number $(= \frac{\nu}{D_{AB}})$ |

| | |
|---|---|
| $St$ | Stanton number $(= \frac{h_f}{\rho c_p U_\infty})$ |
| $T$ | Temperature |
| $U$ | Mean velocity component |
| $c, c_p$ | Specific heat |
| $d$ | Diameter of the jet; size of a square jet |
| $g$ | Gravitational acceleration; calibration function, air-$CO_2$ mixture |
| $h_0^{'}$ | Heat transfer coefficient in a two-temperature situation - no cooling jets |
| $h^{'}$ | Heat transfer coefficient in a two-temperature situation - with cooling jets |
| $h_f$ | Film heat transfer coefficient |
| $h_{rad}$ | Radiation heat transfer coefficient $\left(= \epsilon\sigma(T_w + T_\infty)(T_w^2 + T_\infty^2)\right)$ |
| $k$ | Thermal conductivity |
| $\ell$ | Length of the cooling holes |
| $q$ | Heat rate |
| $t$ | Time; thickness of the leading edge |
| $x$ | Streamwise coordinate |
| $y$ | Spanwise coordinate |
| $z$ | Coordinate perpendicular to the surface |

**Greek**

| | |
|---|---|
| $\Delta$ | Finite change |
| $\bar{\Theta}$ | Calculated dimensionless temperature $\left(= \frac{1-\exp\left[\frac{h_f^2 t_a}{\rho c k}\right]\mathrm{erfc}\left[\frac{h_f\sqrt{t_a}}{\sqrt{\rho c k}}\right]}{1-\exp\left[\frac{h_f^2 t_b}{\rho c k}\right]\mathrm{erfc}\left[\frac{h_f\sqrt{t_b}}{\sqrt{\rho c k}}\right]}\right)$ |
| $\bar{\Psi}$ | Measured dimensionless temperature $(= \frac{T_w(t_a)-T_\infty}{T_w(t_b)-T_\infty})$ |
| $\alpha$ | Thermal diffusivity; angle on the $\bar{\Theta}$ curve |
| $\delta$ | Angle measured with a spanwise line on the surface; incremental change |
| $\delta T$ | Temperature increment $(= T_w(t,z) - T_\infty)$ |
| $\epsilon$ | Measurement uncertainty; emissivity |

| | |
|---|---|
| $\eta$ | Adiabatic film cooling effectiveness $\left(= \frac{T_{aw}-T_\infty}{T_2-T_\infty} = \frac{C_w-C_\infty}{C_2-C_\infty}\right)$ |
| $\bar{\eta}$ | Spanwise-averaged film cooling effectiveness. |
| $\bar{\bar{\eta}}$ | Area-averaged film cooling effectiveness |
| $\theta$ | Angle measured from the geometrical leading edge |
| $\lambda$ | Wavelength |
| $\nu$ | Kinematic viscosity (momentum diffusivity) |
| $\xi$ | Blowing parameter $\left(= \frac{\rho_2 U_2}{\rho_\infty U_\infty} + \left[\frac{\rho_2}{\rho_\infty}\right]^{-\frac{1}{1.41}} - 1\right)$ |
| $\rho$ | Density |
| $\sigma$ | Standard deviation; Stefan-Boltzmann constant |
| $\tau$ | Time increment |
| $\psi$ | Angle measured with a streamwise line through the hole centre |

**Subscripts**

| | |
|---|---|
| 0 | Refers to default output voltage |
| 1 | Refers to row of holes closest to stagnation line |
| 2 | Refers to coolant conditions; row of holes farther from stagnation line |
| $H$ | Refers to the Hue colour component |
| $L$ | Refers to a characteristic length |
| $a, b$ | Refer to time events |
| $aw$ | Adiabatic wall |
| $i$ | Refers to initial conditions; index for data point in a sample |
| $cond$ | Refers to heat conduction |
| $conv$ | Refers to heat convection |
| $rad$ | Refers to heat radiation |
| $ref$ | Reference conditions |
| $w$ | Refers to wall conditions |
| $\eta$ | Refers to film cooling effectiveness |

| | |
|---|---|
| $\infty$ | Refers to free stream conditions |

### Superscripts

| | |
|---|---|
| $i$ | Index for the sampling probes |

# Acknowledgements

I first of all wish to thank my research supervisors, Dr. Martha Salcudean and Dr. Ian S. Gartshore, for their enduring support throughout this undertaking. The financial contribution of Pratt & Whitney Canada and NSERC is fully appreciated. I also wish to thank Mr. Russell Booth and Mr. Steve Giffin from Thermographic Measurements Ltd. for manufacturing and generously supplying the liquid crystal used in this study. The assistance of John Inch from Powertech Labs Inc. with special coatings tools and equipment is gratefully recognized. I was also priviledged to share my time at UBC with a great group of people, and I thank my colleagues Dr. Matthew Findlay, Michael Savage, Petros Lappas, Sidney Chan, and Dr. Peter Mtui for an unforgettable experience. Last, but not least, I thank my immediate family for their encouragement and patiance during the completion of this work.

# Chapter 1

# Introduction

## 1.1 Generalities

Gas turbine technology has had a tremendous impact on the development of modern society, beginning with the first practical applications as early as 1939. That year, a 4MW gas turbine power generating unit was installed at Neuchatel, Switzerland, and the first aircraft powered by a turbojet flew in Germany [29] [33].

In 1995, 1.29 billion people used gas turbine powered airplanes as means of travel, and the forecast of the International Air Transport Association (IATA) predicts that worldwide air travel will more than double over the next 20 years, growing at an annual rate of at least 6%. Air cargo is also projected to grow at over 6% annually [3].

With the deregulation of the electric utility industry, gas turbines are also becoming a key player in the electric power generation. The combined cycle gas turbine power plants operate today at thermal efficiencies very close to 60%, with simple cycle gas turbines operating at more than 40% thermal efficiency; they have come a long way in the span of seven decades from the 18% efficiency of the first electric power gas turbine [29]. Such performance makes the gas turbine increasingly important in electric power generation. At the heart of such a power plant is a gas turbine driving an electric generator with the hot exhaust gas being used in a heat recovery steam generator. A steam turbine coupled with an electric generator

can be added to the system, thus providing additional electricity, or the generated steam can be used as such for various utility processes. The term cogeneration is widely used for such an arrangement.

Other major applications where aeroderivative gas turbines are used are marine propulsion, pumping in oil production platforms and for natural gas pipelines. Gas turbines are particularly attractive for use in offshore or remote oil and gas fields because they can use fuel directly from the source, deliver high power per unit weight, and typically require low maintenance.

With such a wide range of applications, the gas turbine industry has always been highly competitive. It encompasses research and development in many different engineering fields including aerodynamics, heat transfer, material sciences, structures and vibrations, cooling techniques, control theory, and instrumentation technologies. Aircraft propulsion remains the most exciting and demanding application of gas turbines. The combination of hostile thermal environment, high material stresses, and differential transient thermal stresses makes the design for long life extremely complex and difficult. New designs, materials, and manufacturing techniques have emerged over the last decades, steadily increasing the performance of the aircraft gas turbines. Current research programs aim to double the power of military aircraft engines by the end of the century while increasing reliability, and reducing repair costs and maintenance downtime [50]. The goals set by NASA for civil aviation are equally challenging, aiming to reduce the cost of air travel and travel time by a factor of two, emissions by a factor of five, and noise levels by a factor of four, all within the next 20 years [43].

## 1.2 Background

Gas turbines are air-breathing machines, operating on the basis of the Brayton cycle. Although the detailed layout design is different for land based units than for aircraft propulsion units, the principles of operation of the gas generator are the same for both applications.

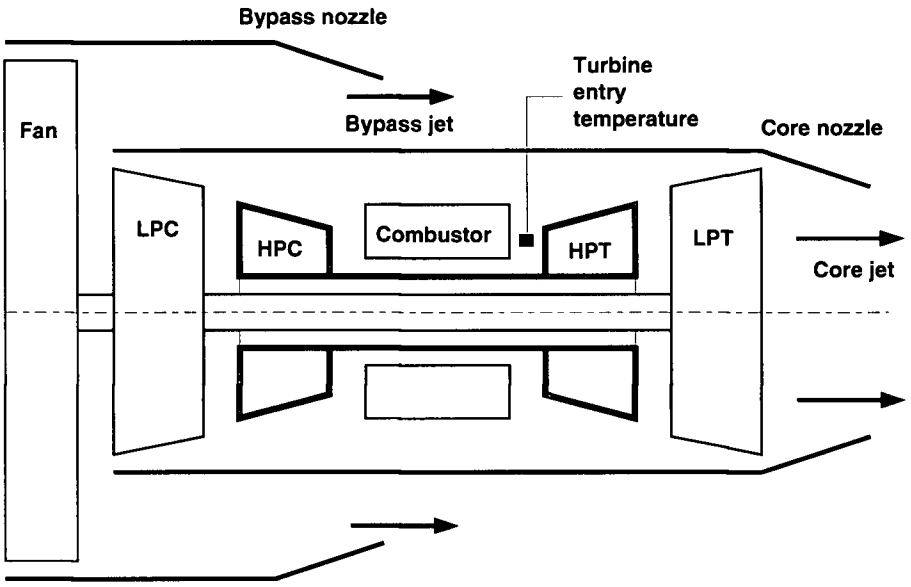


Figure 1.1: Two-spool turbofan engine schematic

The major components of the gas generator are the inlet, compressor, combustor, turbine, and nozzle. A more complex layout is the two-spool turbofan engine schematic presented as an example in Fig. 1.1, configuration widely used for aircraft propulsion.

Air from the atmosphere is guided through an aerodynamic shaped inlet into a first fan stage. Here, the air stream is divided into a core flow and an outer flow, or bypass flow. The core air flow in further compressed in a multistage compressor. The compressed core air is then introduced into a combustion chamber where fuel is injected and the mixture undergoes a quasi-isobaric combustion. The core hot gas expands in a multistage turbine producing shaft work to drive the compressor and fan, and then further accelerates in a nozzle. The outer stream typically flows around the core engine casing. The forward thrust is then computed as a summation of the jet propulsive forces generated from each air stream.

All components have to be designed for maximum efficiency and they also function in an integrated manner. Matching of so many different component characteristics at off-design operation is one of the most challenging problems in engineering. It is well understood that a modification to any of the components will affect the overall performance of the engine. Detailed analysis of various aircraft gas turbine cycles has been done elsewhere [23], [40]. Even

the simplest analysis accounts for the interaction of a large number of design parameters [10].

The large commercial aircraft engines use higher bypass ratios for higher propulsion efficiency, higher cycle pressure ratios (CPR) and higher turbine entry temperatures (TET) for increased thermal efficiency [10], [23], [40]. High propulsion efficiency is thus achieved by increasing the total engine airflow for a given net thrust, while high thermal efficiency is largely associated with the performance of the high pressure compressor and turbine system. A test study done by Rolls Royce for the development of the RB211 three-spool turbofan engine [54], showed that an increase of 20% in TET alone represents only a 5% reduction in the specific fuel consumption (SFC), at fixed component efficiency. Further reduction in SFC can only be achieved by increasing both TET and CPR. Considering that no loss of component efficiency is acceptable, this translates into a serious design and technological challenge.

## 1.3 Structural and Thermal Considerations

The need to increase the TET for high thermal efficiency has led to intensive research in the field of material sciences and cooling techniques. The steady increase of the TET was made possible by the development of new materials, coatings, and improved cooling systems.

High pressure turbine blades, especially the first stage nozzle guide vanes and rotor blades, are experiencing high temperatures (1600 K to 1800 K are not uncommon at the entrance to the first stage vanes), and high structural loads (rotor blades in particular). The blades are basically immersed in the hot gases and receive heat from these gases. These blades typically operate very close to their melting point temperature, and sometimes there are regions on the blades exposed to temperatures higher than their melting point. In order to maintain the structural integrity and fatigue life of the blades, heat has to be removed by means of cooling of the blades. Air bled from one of the compressor stages is typically used for cooling the blades.

The blade material used in advanced gas turbines is clearly of crucial importance. Single

crystal alloys are now used for the high pressure turbine blades together with advanced thermal barrier coatings, thus providing the necessary strength, oxidation and corrosion resistant properties needed for extracting the energy from the very hostile environment.

A rotor blade experiences large centrifugal forces decreasing from the blade root to the blade tip. In addition, there are bending forces, generated by the expansion of the hot gases, which create bending moments about the blade root. For these reasons the rotor blades are typically larger at the root and progressively thinner towards the tip. The failure of a turbine rotor blade can easily produce a very serious event; the broken pieces can easily penetrate the engine casing and cut through fuel or oil pipes. The design must therefore produce blades which will be highly reliable over their predicted lifetime.

The nozzle guide vanes (stator blades) experience less structural stress than the rotor blades. They are clamped at both ends, so the stresses on the vane platform sections will be less than for the rotor blade root sections. There will be radial stresses on the vanes, since they are integrated parts of the engine structural support system. The loads generated on the engine shafts are usually transferred through flanges to the nozzle guide vanes, and from here to the engine mounting pins and thence to the aircraft structure.

From a thermal point of view, the stators have to withstand the hottest combustor streak, with a non-uniform gas temperature profile, both radially and circumferentially, at the combustor exit. The maximum spanwise gas temperature distribution tends to peak at about half the blade span leading edge. The exact location of the maximum temperature on the blade surface will vary with different engine operating conditions.

The thermal impact on the rotor blades is typically less severe than on the stator blades. The rotation of the rotor assembly leads to a relative temperature of the rotor blade surface less than that experienced by the nozzle guide vanes.

Thermal stresses in the blade material, for both stator and rotor blades, are also caused by transient differential temperature between the blade core and the blade leading edge during take-off, landing, or sudden acceleration/deceleration maneuvers. These stresses can lead to low-cycle fatigue (LCF) in the blade material, and specific research has been conducted to

understand and predict this phenomenon [22].

The combination of the described mechanical and thermal loads on a turbine blade identifies the mid-span leading edge and the trailing edge regions as being critical for the integrity of the blade over its operational lifetime. Special attention is focused in the design process on reducing the stresses in these regions. Advanced cooling techniques are now used to reduce the thermal stresses everywhere in the blade and particularly in the leading edge and trailing edge regions.

## 1.4 Cooling Schemes

### 1.4.1 Overview

For the high TET used in today's aircraft engines, the nozzle guide vanes and rotor blades at the forward portion of the turbine need to be cooled in order to preserve the structural integrity and fatigue life of the airfoil. A modern cooling scheme employs both internal and external cooling of the blades and vanes. Cooling air is fed from the root of the rotor blades through interior passages to remove as much heat from the walls as possible, and discharged through discrete holes placed at predetermined locations on the airfoil surface. In the case of the stator blades, the cooling air can be introduced at both ends of the vanes, flowed through interior passages and ultimately discharged through the film cooling holes onto the airfoil surface. The cooling air, ejected from the film cooling holes, extends over the airfoil surface to provide a protective film layer which impedes the hot gases from contacting the surface of the airfoil, thus decreasing the heat transfer to the airfoil. This is known as the film cooling technique.

The interior cooling passages have to be designed to have high heat transfer coefficients, so that the cooling air can remove the maximum heat from the blade. At the same time, the pressure drop in the interior channels should be minimized to allow for the cooling air to be ejected onto the blade surface in regions of adverse pressure gradients, as is the case for the leading edge and the pressure side surface. The film cooling holes, on the other hand, have

to be designed to generate an effective film layer to reduce the external heat transfer rates.

The amount of the cooling air is limited from considerations of gas turbine cycle thermodynamic efficiency. Mixing of the film cooling jets with the main flow causes both stagnation temperature and pressure losses. Therefore, there is an incentive to use as much internal cooling as possible and to minimize the amount of disturbance to the main external gas flow from the cooling jets. There are also losses due to the heat extraction from the blade walls. Since the air used to cool the blades is bled from one of the compressor stages, there is the associated lost work if this air is not used in a combustion process. The use of high pressure cooling air cannot be avoided, in particular for cooling the leading edge region of blades and vanes. The greater the amount of such high pressure cooling air that is needed, the higher the associated losses in available work will be. Accordingly, for each TET there is a determined amount of usable cooling air beyond which the benefits of increased TET are lost. Such analyses have been done in [14], [31]. It was found that the use of film cooling improves performance significantly, and that an increase of the overall cycle efficiency is directly related to an increase in blade operating temperatures.

The key to improved efficiency lies therefore in the use of advanced high temperature materials, to increase the allowable blade operating temperatures, and more efficient internal and external cooling schemes, to reduce the cooling flow for given TET and blade operating temperature. A reduction by a factor of two of the cooling flow within the next 20 years, down to 10% from the 23% of the 1996 baseline engine, is actually one of the goals set for future large subsonic engines [43].

### 1.4.2 Leading Edge Cooling

Cooling of the leading edge of blades and vanes is a challenging problem. This region of the blade experiences high thermal and mechanical stresses and needs to be properly cooled. The interior of the airfoil leading edge typically shows a designated passage that behaves as a common plenum for the film cooling holes. This passage can be abutted by an impingement plate so that the cooling air, flowing through the interior passages, can be discharged into

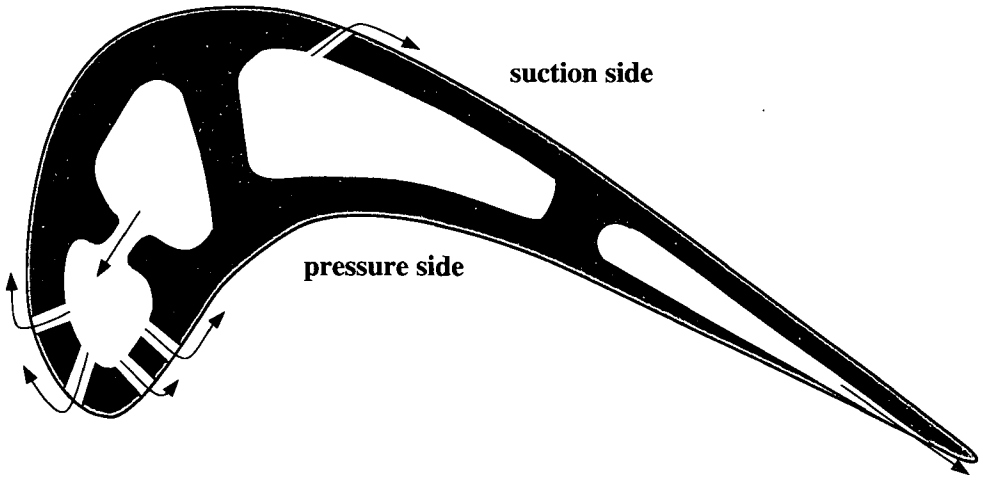


Figure 1.2: Film cooled airfoil section

the leading edge cooling passage through impingement onto the inner leading edge wall. This technique increases the heat transfer at the interior of the leading edge wall, thus removing more heat from this region. Such an arrangement is shown in Fig. 1.2.

The leading edge region cannot be adequately cooled by internal cooling only. The pressurized air from the leading edge passage is also ejected into the main hot gas boundary layer through discrete cooling holes, often arranged in multiple rows on either side of the stagnation line. The leading edge wall is thus cooled by convection through the film cooling holes as well. The film layer has to protect the airfoil for some region downstream of the cooling holes.

The leading edge film cooling holes are placed in the immediate proximity of the aerodynamic stagnation line. High pressure cooling air is required in the leading edge passage to make possible the ejection of the cooling air into the high pressure mainstream. In order to provide good cooling of the airfoil surface while minimizing the amount of cooling air used, the designer has to consider all the geometrical and flow field parameters of importance for the cooling process. This is a difficult task.

## 1.5 Concepts and Definitions

In a gas turbine environment, the maximum allowable metal temperatures are known and set by the appropriate selection of materials and coatings. The maximum hot gas temperatures could be set by considerations of high thermal efficiency and long service life of the high pressure turbine vanes and blades. There is a compromise between high turbine inlet temperatures and cooling air requirements, since the efficiency and thrust are reduced with increasing amounts of cooling air. The design requirement could then be to determine the minimum coolant flow and the related heat transfer rates to maintain the metal temperatures below critical levels. The internal cooling system must take up the external heat transfer rates in their entirety, but the following analysis focuses on the external cooling only.

The general formulation of the convective heat transfer, at an arbitrary location on a film cooled surface of interest, is expressed by Eqn. 1.1 as:

$$q_w = h_f(T_w - T_{ref}) \tag{1.1}$$

where $q_w$ is the convective heat flux [W/m$^2$], $h_f$ is the heat transfer coefficient in the presence of the film layer [W/(m$^2$K)], $T_w$ is the local surface temperature, and $T_{ref}$ is a reference or driving temperature, which may vary with position.

The selection of the reference temperature has a direct impact on the evaluation of the heat transfer coefficient. In this study, a well behaved heat transfer coefficient is sought. If the limiting case of an adiabatic (perfectly insulated) surface is considered, the heat flux is zero and the reference temperature must be equal to the resulting adiabatic surface temperature. The adiabatic wall temperature can thus be used as the reference, or driving temperature. The heat transfer rate equation then becomes:

$$q_w = h_f(T_w - T_{aw}) \tag{1.2}$$

For a film cooled surface, the adiabatic wall temperature distribution is generally un-

known and a function not only of the geometry and mainstream and cooling jets flow fields, but also of the temperatures of the cooling jets and crossflow and the degree of mixing between them. This is known in the literature as the three-temperature problem, namely referring to the temperature of the mainstream ($T_\infty$), temperature of the cooling jets ($T_2$), and the reference temperature ($T_{aw}$) at some location downstream of the injection holes. In this case both the mainstream and the jet flows are present, with different temperatures in the mainstream than in the cooling jets. In this study therefore, film cooling applications are also referred to as three-temperature problems, and use of the three-temperature analysis is understood to be indicative of a film cooling process.

If the flow properties can be assumed constant, the use of the adiabatic wall temperature in Eqn. (1.2) ensures that the heat transfer coefficient is independent of the temperature difference ($T_w - T_{aw}$) and is a function only of the geometry and character of the flow field:

$$h_f = \frac{q_w}{T_w - T_{ad}} \tag{1.3}$$

The heat flux is also naturally zero when the temperature difference goes to zero with no restriction on the heat transfer coefficient.

If any other temperature difference is selected (that is, the reference temperature is not the adiabatic wall temperature), the wall heat flux and the temperature difference do not go to zero simultaneously. The heat transfer coefficient then has to be zero when the heat flux is zero, and goes to either plus or minus infinity when the temperature difference moves through zero. This is the case when the mainstream temperature is used as the driving temperature in the heat rate equation, as pointed out in the past [11]. Previous studies have often tried to avoid the complications of measuring the adiabatic wall temperature or ensuring adiabatic wall conditions. A clear distinction has to be made in such situations between the film heat transfer coefficient $h_f$ defined by Eqn. (1.2) and the heat transfer coefficient $h_0^{'}$ defined by:

$$q_w = h_0^{'}(T_w - T_\infty) \tag{1.4}$$

In the absence of the film layer $T_{aw}$ would be equivalent to the mainstream temperature $T_\infty$, and for high speed flows the recovery temperature should be used. Equation (1.4) thus describes the convective heat transfer rates in a two-temperature problem when there is a temperature difference between the mainstream and the surface. In this case, in the absence of any cooling jets, $T_w$ and $T_\infty$ are the only temperatures involved. The heat transfer coefficient $h_0'$ at any location on the surface of interest is then determined by measurement of the two temperatures, $T_w$ and $T_\infty$, and of the heat flux $q_w$. In general, heat transfer coefficients ($h_0'$) defined on the basis of local wall and mainstream temperatures are dependent on upstream wall temperature distribution even in an essentially unchanging velocity field. For example, in the case of a two-dimensional flat plate laminar boundary layer, $h_0'$ was found to be some 36% different when calculated on the basis of constant wall temperature or constant wall heat flux [4]. However, these differences are only about 4-5% for a fully turbulent flat plate boundary layer [48]. It is therefore generally assumed that, for fully turbulent boundary layers, the values of heat transfer coefficients are essentially independent of the exact upstream wall temperature distribution, provided the flow field remains unchanged and the wall temperature gradients close to the point of measurement are small [4], [11]. This assumption is also made in the present thesis.

To further illustrate the complexity of the convection heat transfer coefficient, consider the situation when both the mainstream and the jet flows are present, and both are at the same temperature. The very presence of the cooling jets can enhance the turbulent transport especially near the injection holes, the consequence being in this case a higher heat transfer coefficient ($h'$) than that obtained without the presence of the jet cooling flow ($h_0'$). With the temperatures being equal in the mainstream and in the cooling jets, the heat transfer rate is expressed in a form similar to that in Eqn. (1.4):

$$q_w = h'(T_w - T_\infty) \tag{1.5}$$

where $T_\infty = T_2 = T_{ref}$, with the heat transfer coefficient $h'$ generally different from the heat transfer coefficient for the case of no injection $h_0'$. Such a formulation might be applicable in

the analysis of some internal cooling arrangements, but hardly useful when the cooling jets are present, and the temperatures are different in the two stream flows.

Since this study is concerned with the external cooling only, the adiabatic wall temperature represents the limiting value of the wall temperature when the heat transfer rate is zero, according to Eqn. 1.2. A non-dimensional representation of the adiabatic wall temperature is the film cooling effectiveness $\eta$, defined by the equation:

$$\eta = \frac{T_{aw} - T_\infty}{T_2 - T_\infty} \tag{1.6}$$

For constant property flows, the energy equation is linear in temperature so that the film cooling effectiveness is a function only of the generated flow field and of the position on the surface. The film cooling effectiveness varies from zero to unity, from locations far downstream where the adiabatic wall temperature approaches the mainstream temperature ($T_{aw} = T_\infty$), to injection hole locations where the adiabatic wall temperature approaches the temperature of the jet flow ($T_{aw} = T_2$) respectively.

The present study focuses on low speed, constant property flows, where the temperature field is uncoupled from the flow field and the energy equation is thus linear in temperature. Within these assumptions, the definition of the heat transfer coefficient $h_f$ by Eqn. 1.2, and the definition of the film cooling effectiveness $\eta$ by Eqn. 1.6 provide two well behaved parameters to completely describe the three-temperature situation on a surface of interest. From an experimental point of view, the linearity of the energy equation for small temperature differences implies that only the temperature difference between the cooling jets and the mainstream is of importance and not the absolute values of the two temperatures. Experiments can thus be performed with heated jets rather than cooled jets to obtain the desired temperature difference between the jet flow and the mainstream flow, giving flexibility to a particular experimental setup.

## 1.6 Literature Review

A comprehensive review of the film cooling technique, analysis and experimental studies, was reported by Goldstein [19]. This study summarizes the expertise in the field of film cooling up to 1970s, almost exclusively including flat plate arrangements. The study concluded that for three-dimensional flows, much more experimental work was needed to account for the effects of various parameters such as hole geometry, density difference between cooling jets and mainstream, and the effect of the interaction of individual jets on the adiabatic wall temperature distribution. Two parameters are typically used in the literature to quantify the discharge of the coolant into the mainstream, the mass flow ratio $M$ or the momentum flux ratio $I$ defined by:

$$M = \frac{\rho_2 U_2}{\rho_\infty U_\infty} \tag{1.7}$$

$$I = \frac{\rho_2 U_2^2}{\rho_\infty U_\infty^2} \tag{1.8}$$

Quite often, the actual heat transfer process was simulated by an analogous mass transfer process, so that measurements of $\eta$ could be made directly at the wall using mass fractions (concentrations) rather then temperatures [19]:

$$\eta = \frac{C_w - C_\infty}{C_2 - C_\infty} \tag{1.9}$$

The use of mass transfer analogy to heat transfer has the experimental advantage that large temperature differences can be readily simulated by using gases of different densities. The analogy is well established for constant property flows and was frequently used. Shadid and Eckert [47] extended the analogy to processes with temperature and concentration-dependent fluid properties. They concluded that the analogy is well satisfied for film cooling and impingement cooling especially for a binary mixture of $CO_2$ and air used in a mass transfer experiment, and for no heat/mass flux into the solid wall.

There is extensive literature dealing with film cooling on flat surfaces, in various configurations and arrangements. However, since the present study focuses on simulated leading edge geometries, only similar leading edge studies will be reviewed here.

A semi-cylindrical leading edge geometry was investigated by Salcudean *et al.* [44] using the heat/mass transfer analogy and a flame ionization detector technique . The geometry consisted of four rows of spanwise inclined fully staggered holes, symmetrically placed about the stagnation line, and fed from a common plenum. Measurements were made in a large subsonic wind tunnel, and results of the flow division between rows of cooling holes and film cooling effectiveness data were reported. Air was used as coolant. The authors found a lower limit of the overall mass flow ratio below which flow reversal occurs in the rows of cooling holes closest to the stagnation line. Film cooling effectiveness values were highest at lower mass flow ratios, close to the cutoff value for the first rows of cooling holes, and decreased abruptly with both increasing and decreasing mass flow ratio. Salcudean *et al.* concluded that alternate designs should be investigated to obtain more uniform cooling over a wider range of mass flow ratios, and to increase the mass flow ratio for maximum $\eta$, to avoid flow reversal in the rows of cooling holes closest to the stagnation line. The uncertainty in $\eta$ was estimated at $\pm 0.05$ at one hole diameter downstream of ejection, and the overall uncertainty in the measurement of mass flow ratios was estimated to be less than 4%.

The effect of the relative stagger of the rows of holes on $\eta$ was addressed by Salcudean *et al.* [45]. The method and the experimental setup used were similar to that in [44], and measurements of $\eta$ were taken at different mass flow ratios for different hole pattern arrangements. The row of holes closest to the stagnation line was displaced in the spanwise direction with respect to the row of holes further away from the stagnation line, from a fully staggered hole pattern to an in-line hole pattern. The authors found that there was an optimum mass flow ratio for highest $\eta$ downstream of the second row of cooling holes, for each relative position of the rows of holes. A fully staggered arrangement was better at lower mass flow ratios, while relatively higher spanwise-averaged $\eta$ was obtained for the in-line hole pattern and for a wide variety of mass flow ratios. The authors concluded that the in-line hole arrangement

was superior to the staggered arrangement as far as $\eta$ is concerned.

Mick and Mayle [37] reported measurements of $h_f$ and $\eta$ for a semi-cylindrical leading edge geometry containing three rows of spanwise inclined fully staggered holes. The model was placed in a low speed, open circuit wind tunnel, while a secondary system supplied air from a common plenum to the film cooling holes. The model surface was fitted with stainless steel heater strips and the surface temperature distribution was measured using thermocouples. The film cooling effectiveness values were calculated from a corrected one-dimensional heat balance on an element of the surface, since the test surface was not adiabatic. The heat transfer test used a constant heat flux boundary condition and $h_f$ was calculated from an energy balance on a heated surface element that included the effects of surface radiation and heat conduction through the wall. Immediately downstream of the cooling holes the spanwise-averaged $\eta$ was highest at the lowest mass flow ratio tested, and decreased with increasing mass flow ratio. Further downstream of the injection sites, highest values of spanwise-averaged $\eta$ were found for the intermediate mass flow ratio tested. Near the cooling holes, $h_f$ was found to be three times the values without injection, and slightly downstream of the holes $h_f$ dropped to values approximately 10% higher than the values without injection. Mick and Mayle also concluded that the regions of high effectiveness do not necessarily correspond to regions of high heat transfer coefficient, and this was more evident with increasing mass flow ratio. The uncertainty in both $\eta$ and $h_f$ data was estimated at 3.5% downstream of the leading edge, and was as high as 17% at locations around and immediately downstream of the cooling holes.

Mehendale and Han [32] studied the effect of high mainstream turbulence on $\eta$ and $h_f$ on a semi-cylindrical leading edge geometry, similar to that in [37] and [44]. Four rows of fully staggered spanwise inclined cooling holes were placed symmetrically about the stagnation line, and measurements were also made in a low speed wind tunnel. A method similar to that employed in [37] was used to calculate $h_f$ and $\eta$. The uncertainty in both parameters was estimated at around 15% in the region around the holes, and at less than 5% downstream of the round leading edge. The authors concluded that $\eta$ decreases with increasing mass

flow ratio, and decreases significantly with increasing mainstream turbulence at lower mass flow ratios. The film effectiveness was less sensitive to increased mainstream turbulence at higher values of the mass flow ratio. The heat transfer coefficient with film injection was found to increase with increasing mass flow ratio, the effect being more pronounced in the leading edge region than further downstream. For the intermediate mass flow ratio tested, the leading edge $h_f$ was found to increase with increasing mainstream turbulence, and no systematic effect of the mainstream turbulence on $h_f$ was found for the lower and higher mass flow ratios tested.

Ou *et al.* [39] used the same technique and geometry as in [32] to investigate the effect of high mainstream turbulence for the case of injection from individual rows of cooling holes. The authors reported that $\eta$ decreases with increasing mass flow ratio for both cases of injection through the rows of holes closest to the stagnation line, as well as for injection through the rows of holes further away from the stagnation line. Increasing mainstream turbulence decreased $\eta$ for both cases but the effect was more pronounced for the rows of holes closest to the stagnation line. The leading edge $h_f$ increased with increasing mass flow ratio, and the mainstream turbulence level generally increased $h_f$ for the rows of holes closest to the stagnation line, while increased $h_f$ was clearly observed for the case of injection through the rows of holes further away from the stagnation line.

Ou and Han [38] followed up the work described in [32], using inclined film slots to replace the original round cooling holes. The scope and the technique used are basically the same as in [32]. The results and conclusions were also consistent with those reported in [32].

The effect of periodic passing wakes on $\eta$ was addressed by Funazaki *et al.* [18] for a leading edge geometry similar to that used in [37], [32], and [44]. The surface temperature was measured by thermocouples embedded in the model surface. The method used in [37] was employed for calculation of $\eta$. The uncertainty in $\eta$ was estimated at about 6% over the leading edge region, and less than 12% for the regions further downstream of the injection holes. The authors identified an optimum mass flow ratio for almost full coverage of the surface and relatively high $\eta$. Periodic wake passage was found to deteriorate the spanwise

$\eta$, while increased mainstream turbulence had no systematic effect on the values of $\eta$. The surface temperature was also visualized by using a thermochromic liquid crystal, but no quantitative data was inferred from this data.

Thermochromic liquid crystals (TLC) can be used to monitor surface temperature distributions, as an alternative to more conventional thermal instrumentation. Hippensteele *et al.* [24] used narrow band liquid crystals on Mylar sheets to determine external heat transfer coefficients along the midchord of a scaled turbine blade model. The heat transfer coefficients were calculated from the liquid crystal monitored surface temperatures using an energy balance on the airfoil model. The uncertainty in the heat transfer coefficient was estimated at $\pm 6.2\%$. Clifford *et al.* [8] used low temperature phase change paints to record surface temperatures in transient convective heating experiments. Heat transfer coefficients were then calculated for internal blade cooling passages using a one-dimensional conduction formulation with appropriate boundary conditions. Heat transfer coefficients were assumed constant with time and insensitive to the upstream wall temperature effect. This latter assumption was based on test cases where heat transfer coefficients were calculated for different upstream wall temperature conditions. Metzger and Larson [36] used similar coatings in transient heat transfer experiments to record surface temperatures. Heat transfer coefficients were then calculated from the one-dimensional response of a semi-infinite medium suddenly exposed to a step change in the convected fluid temperature. The uncertainty in local Nusselt number was estimated at $\pm 12\%$ for a 95 percent confidence level.

The use of thermochromic liquid crystals to record surface temperatures is more common in the literature as applied to two-temperature situations. Such analyses were also done by Camci *et al.* [5], von Wolfersdorf *et al.* [52], Wang *et al.* [53], and Chyu *et al.* [7] to name a few.

The more complicated three-temperature situation, as applied to film cooling arrangements, was addressed by Vedula and Metzger [51] for the case of flat plate air injection through streamwise inclined holes, and Ekkad *et al.* [12] [13] for the case of flat plate air and

$CO_2$ injection through compound angle holes. Film cooling effectiveness and heat transfer coefficient were determined from two related transient tests using a method similar to that described in [36]. Relatively narrow band liquid crystals were sprayed onto the surfaces of interest to determine local temperatures. The uncertainty in $\eta$ was estimated in [51] at $\pm 12\%$ and that in $h_f$ at $\pm 8\%$, and the estimated uncertainty in [12] was $\pm 6.5\%$ for $h_f$ and $\pm 8.5\%$ for $\eta$.

In summary, very few studies have addressed the heat transfer characteristics ($\eta$ and $h_f$) in the leading edge region of turbine blades. In some of these studies, the heat and mass transfer analogy was used to obtain $\eta$ from an isothermal mass transfer experiment, while the other studies used steady-state heat transfer experiments with constant surface heat flux to obtain $h_f$, and with constant temperature secondary gas to obtain $\eta$. A couple of studies [51], [12] [13] reported values of $\eta$ and $h_f$ in three-temperature situations using the transient one-dimensional conduction response of a semi-infinite wall. In these latter cases, relatively narrow-band liquid crystals were used to monitor the time required for the surface temperature to reach predetermined values set by the colour change of the liquid crystal surface coating; two related tests were needed in these studies to obtain the required information for the simultaneous calculation of $\eta$ and $h_f$. This transient technique using narrow-band liquid crystals in film cooling applications has the disadvantage that two separate tests are needed to obtain the heat transfer characteristics, and improper choice of the liquid crystal colour change temperatures can lead to large errors in $\eta$ and $h_f$ [26].

## 1.7 Objectives and Scope

Cooled turbine blades and vanes are very expensive components since they require advanced high temperature materials and coatings, involve complicated cooling schemes, are hard to manufacture, and require special inspection techniques. The design of a high performance turbine blade is in itself a very costly undertaking. Multiple developments may have to be

made in order to correct deficiencies of a baseline design. Each design modification has to be finally certified through expensive and thorough rig testing. Due to the complexity of the modern turbine blade cooling systems, and the large number of flow field and geometrical parameters involved, accurate calculations of $\eta$ and $h_f$ over the regions of interest are yet to be made. The turbine designer relies heavily on experience and modeling.

One of the limiting factors in using higher turbine entry temperatures is thermal fatigue in the leading edge of turbine blades and vanes. Reduced thermal stresses in this region translate into longer blade rupture life, which means fewer blade replacements during the engine lifetime, and big financial benefits for the airline operators. Improvements in the design and performance of leading edge cooling could lead to either reduced cooling air for a given TET, or the TET could be increased for given amounts of cooling air, both situations being beneficial for the overall engine performance.

The literature still contains few studies of leading edge film cooling, the general agreement being that more research is required to analyse and quantify the effects of the many flow and geometrical parameters involved. The scope of the present work is to investigate several issues related to the performance assessment and film cooling design of the leading edge of turbine stator blades, or vanes.

Specifically, the objectives of the present experimental investigation are as follows:

1. To make a comparative assessment of two different leading edge geometries based on film cooling effectiveness measurements using a flame ionization detector technique. A broad range of variables will be considered including Reynolds number, mass flow ratio, coolant density.

2. To explore the effects of geometry in a new leading edge design, and to compare the film cooling effectiveness results measured using a flame ionization detector technique from this geometry with the results from the other two leading edge geometries.

3. To create simple correlations of film cooling effectiveness for some of the investigated cases, so that the measured results can be used more directly in existing design proce-

dures.

4. To develop, implement, and validate a transient heat transfer technique based on wide-band liquid crystal thermography. This technique uses the surface temperature history, which is calculated from the digitally recorded true-colour information during a single transient test, for the simultaneous determination of $\eta$ and $h_f$ in three-temperature situations.

The subsequent chapters of this study will provide details of the experimental setup, theory, and methodology used to achieve these goals. Chapter 2 presents a comparative investigation of three leading edge geometries based on a flame ionization detector technique in isothermal mass transfer experiments. Chapter 3 is dedicated to a new technique based on wide-band liquid crystal thermography. Chapter 4 presents an application of wide-band liquid crystal thermography and a comparison of film cooling effectiveness data calculated from the liquid crystal method with film cooling effectiveness data measured with a flame ionization detector technique. In Chapter 5 the conclusions of this study are presented and recommendations for future work are made.

# Chapter 2

# Measurements of Leading Edge Film Cooling Effectiveness Using a Flame Ionization Detector

This section describes the measurement of film cooling effectiveness for three leading edge geometries using the mass/heat transfer analogy in fluids with constant properties. The flame ionization technique and the wind tunnel setup used in the experiments are presented. To simulate the effect of different temperatures, and thus different densities, in the cooling jets and the mainstream in an adiabatic process, either air or $CO_2$ was used as coolant in the corresponding isothermal mass transfer process. The density of the $CO_2$ is approximately 1.5 times higher than the density of air thus simulating an absolute temperature ratio of about 1.5. Actual temperature ratios in the leading edge of an operating turbine may be higher, but the present experiments at least give trends of film cooling effectiveness as coolant density increases relative to mainstream density. A correlation was developed for the film cooling effectiveness data from the leading edge region of one of the geometries used and results are presented. An example of an improved coolable leading edge of a gas turbine blade is also shown in this section. This new leading edge geometry achieves higher film cooling effectiveness at mass flow ratios sufficiently high to provide a safe backflow margin.

This is accomplished by appropriate distribution of film cooling holes both in a spanwise and chordwise manner within given structural constraints. The experimental investigation is carried out at zero angle of attack with air as coolant medium at different mass flow ratios.

The experimental investigation described in this section was undertaken to provide basic insight into the film cooling injection through multiple rows of holes in the leading edge of turbine blades. The final leading edge design was discussed with Pratt & Whitney Canada.

## 2.1 Experimental Arrangements

### 2.1.1 Model and Wind Tunnel Setup

The experiments were performed in the Aerodynamics Laboratory at the University of British Columbia using a large open-circuit blower-type wind tunnel. The mainstream was driven by a 2.44 m diameter variable pitch 16-blade fan powered by a 125 HP motor. The test section was 2.44 m wide by 1.66 m high and was located downstream of a 4:1 area contraction section. The maximum tunnel air speed was above 20 m/s and was measured by Pitot tube. One of the wind tunnel side walls was made of clear plexiglass for observation purposes.

A large scale turbine blade model was manufactured from acrylic plastic and had a semi-cylindrical leading edge with a diameter $D$ of 127 mm, and an afterbody with parallel top and bottom sides 1.19 m long, and overall chordwise length of 2.28 m. The model did not follow the shape of a typical turbine blade except for the leading edge region where the measurements were taken. The model was mounted horizontally and spanned the test section at zero incidence so that the frontal blockage of the tunnel was 7.9%. To reduce or eliminate spanwise flow in separation bubbles, fences were placed on the model at spanwise positions $\pm 0.95$ m from the tunnel centreline. The overall arrangement of the model in the wind tunnel test section follows that in [44] and is shown in Fig. 2.1. Turbulence intensities and the uniformity of mean velocities in the wind tunnel test section were measured in [44] at the location of the model's leading edge but without the presence of the model in the test section. Turbulence intensities were less than $\pm 1\%$ and mean velocities were uniform to

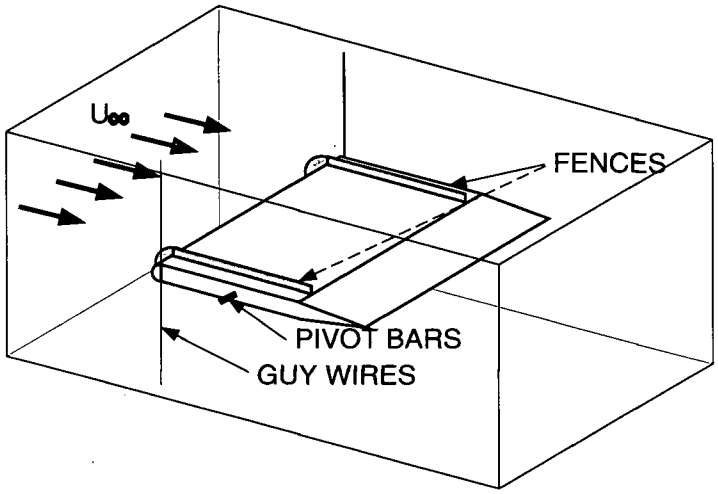


Figure 2.1: Wind tunnel turbine blade model.

within $\pm 1\%$.

The central region of the model was hollow and accommodated a plenum attached to a removable leading edge insert which contained the film cooling holes. The plenum was free to slide inside the model's afterbody for removal and attachment of the leading edge insert. This modular construction allowed for fast replacement of one leading edge insert with another, so that different film cooling hole patterns could be easily investigated without any modification to the overall wind tunnel setup. The plenum was fed with coolant gas (either air or $CO_2$) contaminated with trace amounts of propane through a 25 mm delivery hose near the trailing edge of the model. The plenum also contained a flow baffle and 2 fine screens for uniform delivery of the coolant gas to a perforated impingement plate attached to the leading edge insert, and thence to the film cooling holes located in the removable insert. Details of the plenum arrangement are shown in Fig. 2.2.

### 2.1.2 Baseline Leading Edge Geometry

The baseline geometry used in the present study follows the description in [44]. The model had a semi-cylindrical leading edge with a diameter $D$ of 127 mm and a uniform thickness $t$ of 25.4 mm. Four rows of cooling holes, located symmetrically at $\theta_1 = \pm 15^0$ and $\theta_2 = \pm 44^0$ from the stagnation line, were machined with an inclination of $\delta = 30^0$ to a spanwise line on

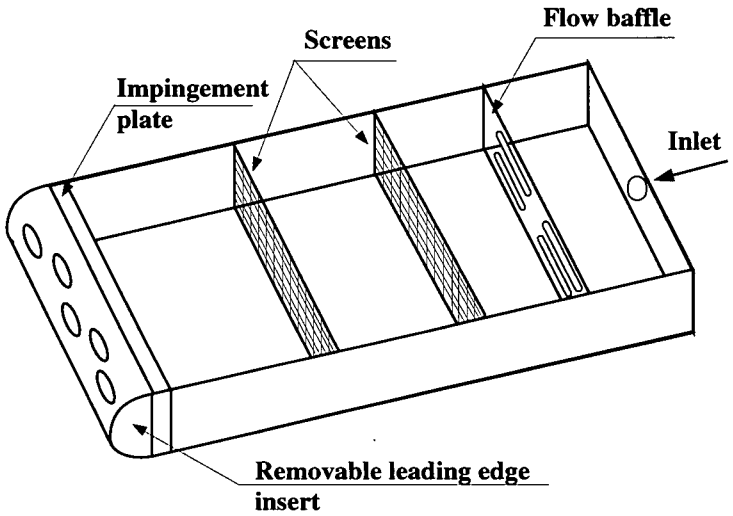


Figure 2.2: Plenum arrangement and removable leading edge insert.

the leading edge surface. The row of holes at $\pm 15^0$ is referred to as row $\theta_1$, and the row of holes at $\pm 44^0$ is referred to as row $\theta_2$. Each row consisted of 7 holes with a diameter $d$ of 12.7 mm located 4 hole diameters apart in the spanwise direction, or $S_r = 4d$. On each side of the stagnation line, the two adjacent rows of holes were staggered in the spanwise direction at a distance $S_{ar}$ of 2 hole diameters. This particular hole pattern was also referred to as a *fully staggered* arrangement. Perfect symmetry was achieved across the stagnation line so that $S_{LE} = 0d$, this hole arrangement being also referred to as an *in-line* pattern. Due to the $30^0$ hole inclination and the 25.4 mm thickness of the leading edge wall, the hole length along its centreline was $\ell = 4d$. Details of the baseline geometry are shown in Fig. 2.3.

### 2.1.3 Compound Angle - CA Geometry

A removable leading edge insert was machined with a compound angle hole pattern and this geometry is referred to as the CA geometry. The outer diameter and the thickness of the leading edge as well as the diameter of the holes were the same as for the baseline geometry ($D$ = 127 mm, $t$ = 25.4 mm, $d$ = 12.7 mm). All the other design parameters such as number and position of the rows of holes, hole location and hole inclination with respect to the spanwise direction were also the same as for the baseline geometry.

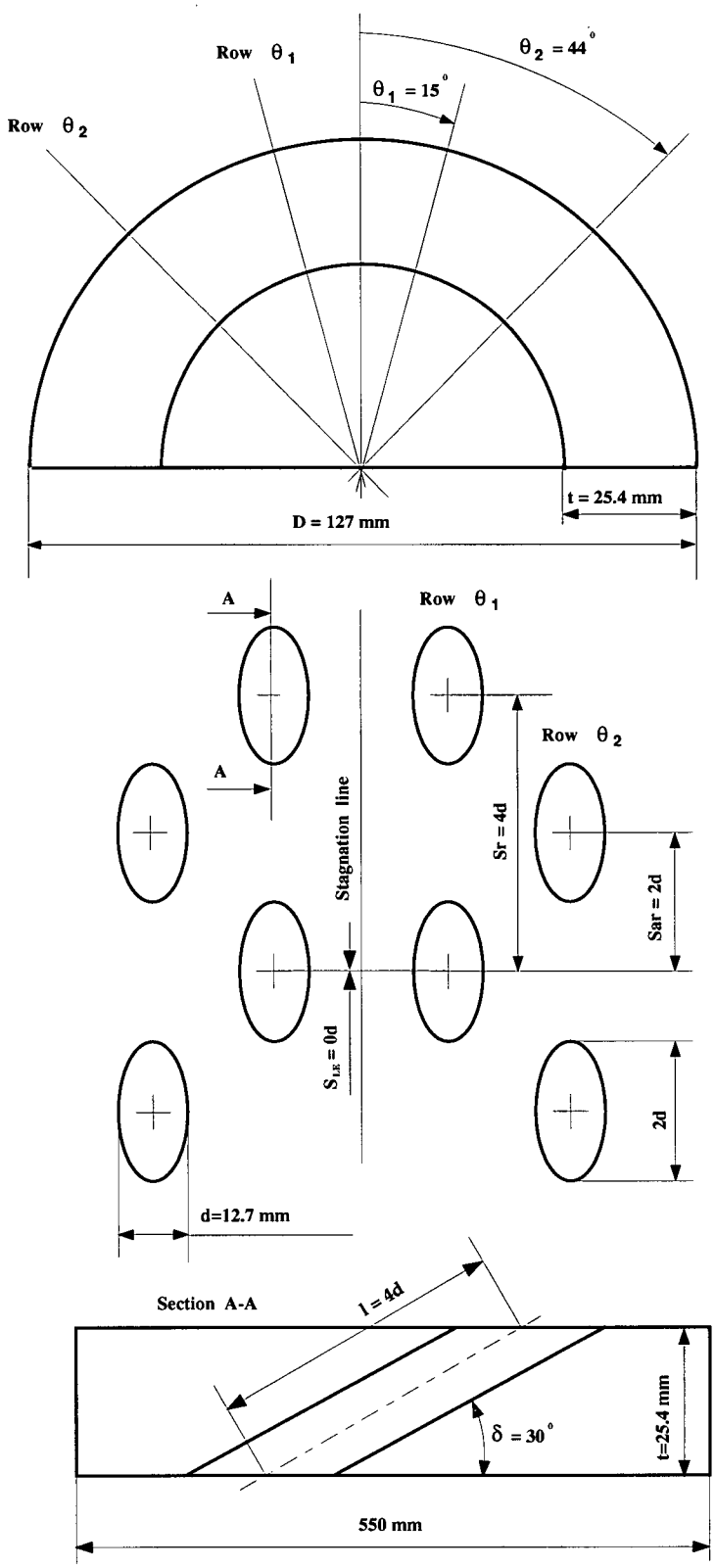


Figure 2.3: Baseline geometry.

The CA geometry was different from the baseline geometry only with respect to the inclination of the film cooling holes. In addition to the $\delta = 30^0$ angle with a spanwise line on the surface, the holes for the CA geometry were also machined with an inclination of $\psi = 33^0$ with a streamwise line passing through the centre of the holes (refer to Fig 2.4 on page 27 for the definition of $\psi$).

In this configuration, a group of 4 holes intersected each other at the inner side of the leading edge in a rather complicated pattern. This arrangement was a feature of this particular CA geometry and it should not be assumed that cooling holes intersect each other in real blade design. The common plenum of each group of 4 holes changed the flow entrance conditions for the CA geometry as compared to the entrance conditions for the baseline geometry. The hole length along its centreline was different from the holes in row $\theta_1$ to the holes in row $\theta_2$, and different from the baseline geometry case. For the CA geometry, $\ell = 5d$ for the holes in row $\theta_1$, and $\ell = 7.5d$ for the holes in row $\theta_2$.

### 2.1.4 Improved Leading Edge Geometry

#### 2.1.4.1 Background Information

Some of the issues regarding the cooling of the leading edge region of turbine blades have been reviewed in section 1.4.2 on page 7 of this study, and a typical cooling arrangement was shown in Fig. 1.2. The cavity in the most forward region of the blade, shown in Fig. 1.2, extends radially over the entire spanwise length of the blade and provides the necessary coolant flow to the film cooling holes in the leading edge of the blade. In this particular arrangement, the leading edge cavity is continuously supplied with coolant flow through holes in the inner wall enclosing the cavity. The coolant from the leading edge cavity is discharged through multiple rows of holes into the hot gas boundary layer to protect the skin of the blade for some region downstream of the injection sites.

The coolant flow in the leading edge cavity must be therefore at higher pressure than the pressure of the core hot gases which can also vary radially along the blade span. The

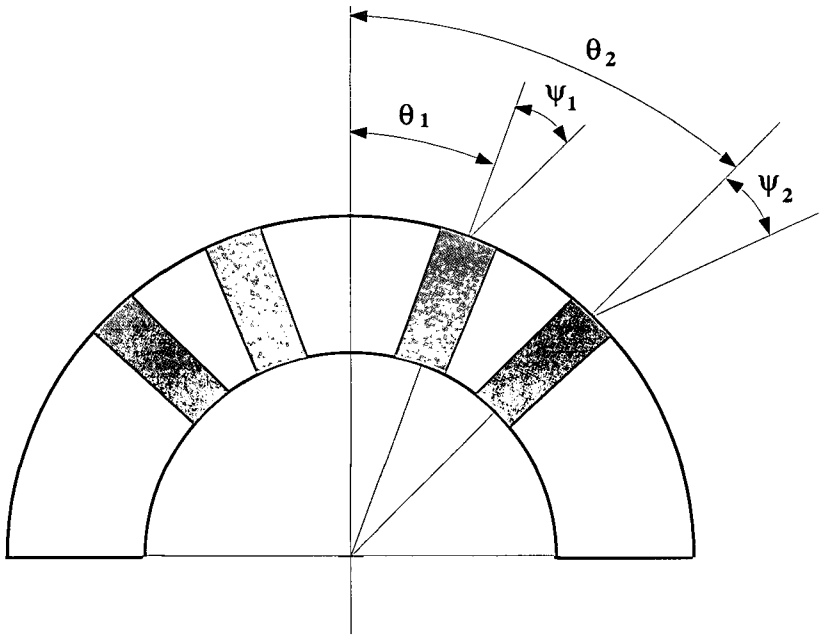


Figure 2.4: Geometrical nomenclature.

exact pressure and temperature distributions around the leading edge region of the blade are therefore required as inputs in the design of the blade cooling system. A potentially serious problem occurs if the coolant supply pressure in the leading edge cavity drops below the levels required to maintain a uniform coolant flow through all the discharge holes in the leading edge of the blade. In this situation, the mainstream hot gas can penetrate through the film cooling holes. This phenomenon is known as backflow and can drastically reduce the operating life of the blade or even cause the blade failure. The design of the cooling supply system to the leading edge cavity is not addressed in this study, but it is understood that a uniform cooling flow is required through the holes at the leading edge of the blade. In order to keep a safe backflow margin, a high enough coolant pressure must be maintained in the leading edge cavity and this translates into higher overall mass flow ratios through the film cooling holes.

The coolant removes heat from the leading edge wall by convection through the film cooling holes and then interacts with the hot gas boundary layer to form a protective film layer which reduces the heat transfer rates at critical points on the leading edge outside

surface. The arrangement of the film cooling holes around the leading edge region and the geometrical characteristics of the array of cooling holes are critical for maximizing the effectiveness of any particular cooling scheme. A strong interaction between the cooling jets and the crossflow can cause significant aerodynamic penalties with direct consequences on the overall efficiency of the gas turbine. The change in the relative position of the aerodynamic stagnation line with respect to the film cooling holes at various engine operating regimes also has to be considered. In a particular arrangement, the film cooling holes could be placed about the aerodynamic stagnation line corresponding to the most demanding engine operating conditions, but for any variation in the position of the aerodynamic stagnation line no backflow is allowed and the coolant still must be discharged through holes on either side of the stagnation line.

A good coverage of the leading edge region, both on the inner side and on the outer side of the leading edge wall, is typically achieved with multiple rows of cooling holes disposed at specified angles $\theta$ around the leading edge. The cooling holes are spaced at a distance $S_r$ apart in either row, could be spaced at a distance $S_{ar}$ apart in adjacent rows on either side of the stagnation line, and could be also spaced at a distance $S_{LE}$ apart in the adjacent rows about the stagnation line. These geometrical parameters were defined in Fig. 2.3 on page 25 for the particular case of the baseline geometry. The cooling holes could be generally placed at an angle $\delta$ with a spanwise line on the surface and at an angle $\psi$ with a streamwise line passing through the centre of the holes. The compound angle $\psi$ is defined in Fig. 2.4. More complicated cooling hole exit geometries can be obtained. In all cases, structural considerations prevail so that the cooling holes are not allowed to intersect each other and a critical wall thickness has to be maintained between holes.

#### 2.1.4.2 PVC Geometry

The development of the present PVC geometry included design modifications to different geometrical parameters such as row stagger about the geometrical leading edge $S_{LE}$, stagger of adjacent rows $S_{ar}$, and hole compound angle $\psi$ [30]. The leading edge thickness to hole

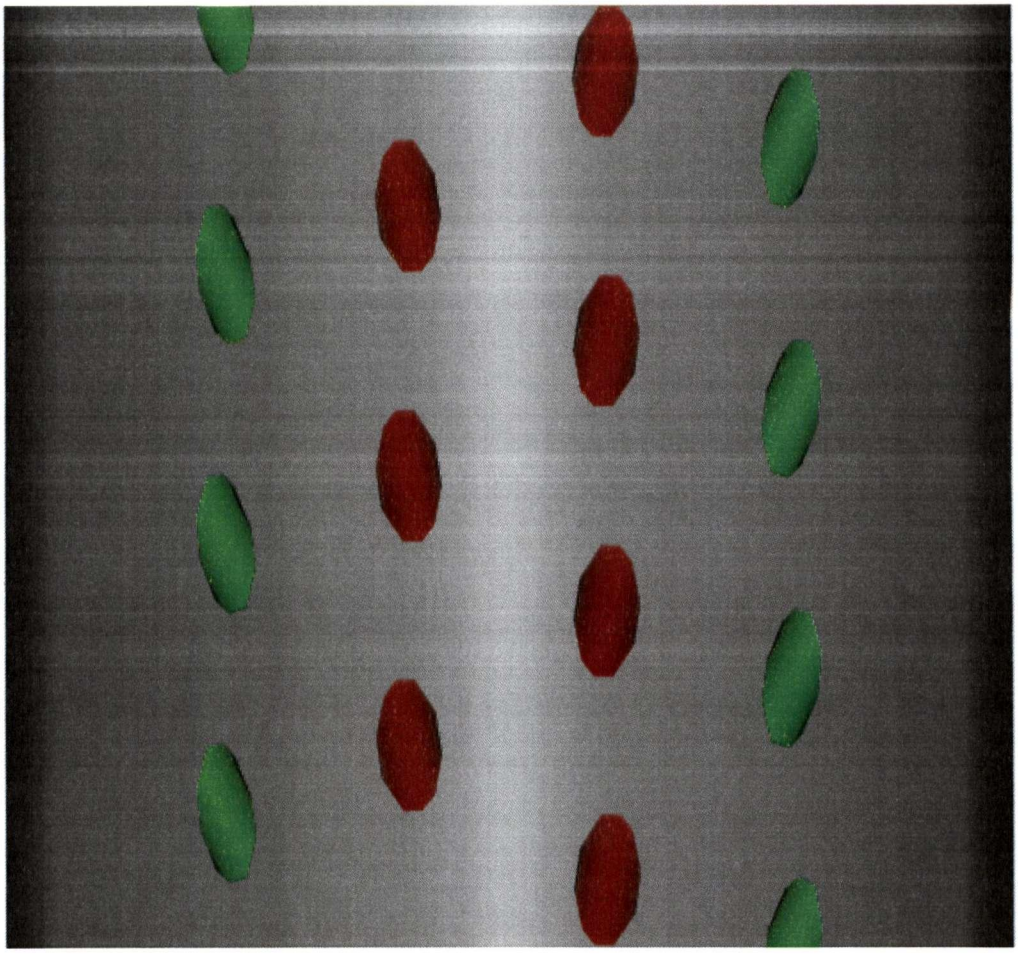

Figure 2.5: PVC geometry - outside view.

diameter ratio $t/d$ [42], the inclination angle with a spanwise line on the surface $\delta$, the hole pitch in a row of holes $S_r$, and the position of the rows of cooling holes defined by angles $\theta_1$ and $\theta_2$ were fixed in the design process. The parameters $S_{LE}$, $S_{ar}$, $S_r$, $t/d$, $\delta$, $\theta_1$ and $\theta_2$ were defined in Fig. 2.3 on page 25, and $\psi$ is defined in Fig. 2.4.

It is understood that in this particular arrangement, the cooling holes shown in Fig. 2.4 are neither placed in the same streamwise plane perpendicular to the leading edge, nor could they be defined entirely in such a plane due to the spanwise angle $\delta \neq 0$. The PVC geometry features 4 rows of cooling holes placed at $\pm\theta_1^0$ and $\pm\theta_2^0$ about the geometrical leading edge [42]. The holes in row $\theta_1$ and row $\theta_2$ are machined at an angle $\psi_1$ and $\psi_2$ respectively between the hole centreline and the local spanwise plane normal to the blade surface. All holes are machined at an angle $\delta$ with a spanwise line on the surface. The

outside layout of the cooling holes is shown in Fig. 2.5 and detailed technical specifications were provided to Pratt & Whitney Canada, a principal sponsor of this research [30].

## 2.2 Experimental Procedures

### 2.2.1 The Heat and Mass Transfer Analogy

Measurements of film cooling effectiveness (defined by Eqn. 1.6 on page 12) in a heat transfer process could be made by measuring temperature at an adiabatic wall, in the coolant and in the mainstream ($T_{aw}$, $T_2$, and $T_\infty$ respectively). It is often difficult to ensure adiabatic boundary conditions experimentally, but it is relatively easy to make the wall impermeable in a mass transfer process. If the corresponding non-dimensional transport equations have the same form, the same mechanism governs the transport of momentum, heat, and mass for a given configuration and the processes are said to be analogous. This is also known as the Reynolds analogy.

The analogy between heat and mass transfer processes proved very useful in film cooling applications since measurements of adiabatic wall temperatures are basically analogous with measurements of isothermal impermeable wall concentrations. Rather than having the jets at a different temperature (and hence, at a different density) from the mainstream in a heat transfer process, a gas of different composition is injected isothermally in a mass transfer process. As discussed by Goldstein [19], the film cooling effectiveness can be then calculated based on measured concentrations at an impermeable wall, in the coolant and in the mainstream ($C_w$, $C_2$, and $C_\infty$ respectively) according to Eqn. 1.9 on page 13.

Details of the derivation of the analogy between heat and mass transfer may be found in [46], and details of the similarity of the velocity, thermal and concentration boundary layers may be found in [25]. The restrictions associated with using the analogy were analysed in [47]. For the low speed constant property fluid situation, the heat and mass transfer analogy depends on having geometrical similarity and the Prandtl number ($Pr$) equal to the Schmidt number ($Sc$), or the Lewis number ($Le = Sc/Pr$) equal to one. The Prandtl number

is the ratio of momentum diffusivity $\nu$ to thermal diffusivity $\alpha$, and the Schmidt number is the ratio of momentum diffusivity to mass diffusivity $D_{AB}$. In the case of fully turbulent boundary layers, both the turbulent Lewis number and the molecular Lewis number should be unity for the analogy to be complete.

These conditions are satisfied for gases and in film cooling applications with adiabatic and impermeable walls respectively, since the temperature and concentration gradients at the wall are zero in such situations and thus the influence of molecular $Pr$ and $Sc$ is small.

### 2.2.2 The Flame Ionization Detector

A system used for measuring concentration values in turbulent flow was described by Fackrell [15], [16]. This system was designed to measure very low concentration levels, where conventional laboratory techniques could not be used. The technique uses a flame ionization detector (FID) that is sensitive to a hydrocarbon trace gas. The FID consists of a hydrogen and air flame which burns in an insulated flame chamber. A voltage is applied across the chamber and the introduction of a hydrocarbon trace gas into the flame, such as propane, leads to the production of ions. The small current which can pass through the contaminated gas is amplified to a suitable voltage output by an electronic amplifier. The analog signal can then be sampled by a data acquisition board for direct storage into a digital computer (PC).

Theoretically, the FID response is linear with the mass flow rate of hydrocarbons entering the flame chamber such that the output signal should be $E = aC\rho Q$, where $a$ is a constant, $C$ is the concentration, $\rho$ is the density of the hydrocarbon gas, and $Q$ is the flow rate through the chamber. However, the efficiency of the ionization process is a more complicated function of flow rate, such that the output signal is actually $E = aC\rho f(Q)$ but is still linear with concentration. Tests were done with different calibration gases, and it was found that the FID response is indeed linear with concentration for values up to 2000 ppm, and that the system was sensitive to concentration values as low as 1-2 ppm of propane [15].

For the present experimental investigation, propane was used as a trace gas and it was

thoroughly mixed with the coolant flow (which was either air or $CO_2$). The maximum concentration of propane in the plenum varied from one test to another, but it was never higher than 1000 ppmv (parts per million by volume). The very high sensitivity of the FID system to low levels of concentration was particularly useful in the present experimental procedure. The use of very low trace gas concentrations did not affect the restrictions imposed by the use of the heat and mass transfer analogy, in particular the effect of the trace gas on the mass diffusivity coefficient $D_{AB}$ were assumed to be negligible.

### 2.2.3 FID Calibration

#### 2.2.3.1 Calibration of the Air-Air Mixture

When air is used as coolant, gas of the same composition is present both in the jets and in the mainstream. In this case, the system needs to be calibrated only for two reference concentrations, and the linear response of the FID is used to calculate other concentrations. Sampling of the propane contaminated flow was done through a series of needle probes as described in section 2.2.4. The calibration procedure used is described in the following.

1. The system was first calibrated for "0%" concentration of propane. This was achieved by disconnecting the propane feed from the plenum flow. The default output voltage $E_0$ was recorded for this situation. This value should be the same for all needle probes.

2. The propane feed was connected to the plenum flow which was sampled to determine the highest possible, or "100%", concentration of propane. The needle probes were then individually calibrated for their "100%" reference point and the corresponding output voltage $E^i_{100\%}$ was recorded, where $i = 1$ to 12 represents the number of the needle probes being calibrated.

3. One needle probe was installed inside the plenum and was used to monitor the "100%" reference point in the plenum at the beginning of each sampling sequence. A linear interpolation was used to adjust this reference level for variations within $\pm 2.5\%$ of the

trace gas concentration in the plenum. If reference levels fell outside the $\pm 2.5\%$ limits, the test was aborted. The other 11 needle probes were disconnected from the plenum flow and were exposed to the mainstream at predetermined locations on the leading edge.

For each sampling probe, linear interpolation was used between the two reference calibration points to determine the local concentration at the wall according to Eqn. 2.1:

$$C_w^i = \frac{E^i - E_0}{E_{100\%}^i - E_0} \tag{2.1}$$

Since only the plenum flow was contaminated with the trace gas, $C_2 = 1$ and $C_\infty = 0$ in Eqn. 1.9 so that the film cooling effectiveness was calculated directly from:

$$\eta = C_w \tag{2.2}$$

#### 2.2.3.2 Calibration of the Air-$CO_2$ Mixture

When $CO_2$ is used as coolant, gases of different composition are present in the jets and mainstream flow respectively. Downstream of the injection sites, the $CO_2$ jet flow (which is contaminated with small amounts of propane) is mixed with the mainstream air flow. In this case, a special calibration of the air-$CO_2$ mixture is required and the procedure is described in the following.

1. A separate setup was used for calibration of the air-$CO_2$ mixture. The setup included a metered air feed, a metered $CO_2$ feed connected to an in-line heater, and a propane feed connected to the $CO_2$ feed. The in-line heater was used to maintain the $CO_2$ flow at the same temperature as the air flow. The air and the propane contaminated $CO_2$ were then thoroughly mixed in a specially designed mixing box, and directed through a chamber where a sampling needle probe was installed.

2. With the $CO_2$ and propane flow disconnected, air flowed through the sampling chamber and the default voltage $E_0$ was recorded.

3. With the air flow disconnected, a known amount of $CO_2$ was contaminated with a trace amount of propane and directed through the sampling chamber. The corresponding FID voltage was recorded as $E_{100\%}$. The $CO_2$ contaminated flow was maintained at this rate for the rest of the calibration procedure.

4. With the $CO_2$ contaminated flow fixed at a known rate, the air flow rate was varied in incremental steps and the mixture was directed through the sampling chamber. The corresponding FID output voltage $E$ was then recorded for each known mass fraction of $CO_2$ in the mixture.

The calibration data set was analysed and a fourth order polynomial was fitted through the data points. The above procedure was repeated for different $CO_2$ flow rates and different amounts of propane. The repeatability of the calibration curve was extremely good, with variations less than $\pm 2\%$. This procedure allowed a check to be made on both the linearity of the FID response with the small amounts of propane used, and the independence of the FID response to the amount of $CO_2$ gas present in the plenum. The average calibration curve for the air-$CO_2$ mixture is presented in Fig. 2.6 on a mass fraction basis. This calibration curve was then used in the experiments to calculate the actual $CO_2$ concentration at the wall from the recorded raw FID output voltage $E$. The maximum uncertainty of the calibration curve was estimated at less than $\pm 2\%$.

The calibration of the "0%" and "100%" reference points followed the procedure described in section 2.2.3.1. This time, the plenum flow consisted of $CO_2$ gas contaminated with a trace amount of propane. The exact procedure is described next.

1. With the $CO_2$ feed disconnected, air flowed through the plenum and the reference voltage $E_0$ was recorded. This value should be the same for all needle probes.

2. The air feed was disconnected from the plenum and the propane contaminated $CO_2$ feed was connected instead. The needle probes were fed from this plenum flow exclusively, and were individually calibrated for their "100%" reference point. The corresponding

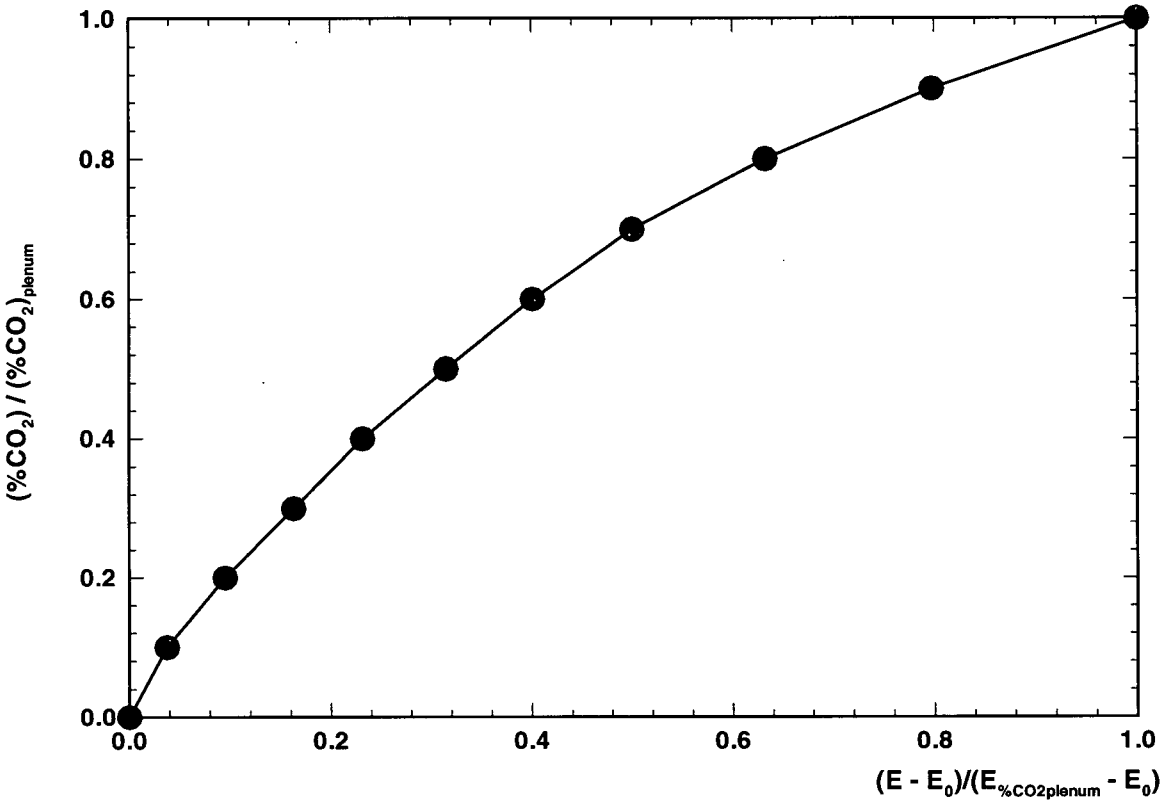


Figure 2.6: Mass fraction calibration for the air-$CO_2$ mixture.

output voltage $E^i_{100\%}$ was recorded, where $i = 1$ to 12 represents the number of the needle probes being calibrated.

3. One needle probe was installed inside the plenum and used to monitor the "100%" reference point in the plenum at the beginning of each sampling sequence. A linear interpolation was used to adjust this reference level for variations within $\pm 2.5\%$ of the trace gas concentration in the plenum. Again, if the reference voltage showed variations larger than $\pm 2.5\%$, the test was terminated. The other 11 needle probes were disconnected from the plenum flow and were exposed to the mainstream at predetermined locations on the leading edge.

Here too, only the plenum flow was contaminated with the trace gas, so that $C_\infty = 0$ and $C_2 = 1$. The film cooling effectiveness was consequently calculated from the raw FID

output voltage $E$ with the use of the air-$CO_2$ mixture calibration curve as:

$$\eta = C_w = g\left(\frac{E^i - E_0}{E^i_{100\%} - E_0}\right) \tag{2.3}$$

where $g$ is the calibration function shown in Fig. 2.6.

### 2.2.4 The Sampling Procedure

Measurements of film cooling effectiveness were made by sampling the mixture of contaminated coolant and mainstream gas very close to the wall and immediately downstream of the injection sites. Sampling was achieved through a series of 11 very fine needle probes with outer diameter of 0.5 mm and spaced $d/2 = 6.35$ mm apart lying directly on the surface of the model, thus covering a spanwise distance of $5d = 63.5$ mm on the leading edge. The sampling probes were mounted on a specially designed rake that kept the probes parallel to the crossflow and at predetermined locations on the leading edge. The rake was attached to a suitable traverse mechanism driven by step motors to allow the accurate positioning of the needle probes on the leading edge. The positioning error of the probes was $\pm 1$ mm. The gas mixture was sampled through these probes and sent through small tubes to a Scanivalve and thence to the flame ionization detector which measured the concentrations with an estimated uncertainty of $\pm 1\%$.

A dedicated PC and software were available for data acquisition from the FID. A computer program controlled the location of the rake, the switching and time delay between sampling probes, and the processing of the amplified FID output voltage. The sampling flow rates were kept constant during the experiment by using a suitable pump and a settling chamber as described in [16]. A time delay of 15 s was used before sampling from each probe to permit the cleaning of the tubes of the residual mixture from a previous sample sequence. A total of 2000 data points sampled at 130 Hz were averaged to calculate $\eta$ at each needle probe location. The estimated film cooling effectiveness uncertainty in [44] accounted for errors in flow rate measurement (less than $\pm 2\%$), flame ionization detector sensitivity (less

than $\pm 1\%$), sampling at 0.25 mm above the wall (less than $\pm 3\%$); for the present measurements, $\eta$ was measured with an uncertainty of less than 2.5% for air injection and less than 3% for $CO_2$ injection.

## 2.3 Experimental Results

For the baseline geometry, measurements of $\eta$ were taken using either air or $CO_2$ as coolant gas. The effect of double row and single row injection was investigated. The mass flow ratios (defined by Eqn. 1.7 on page 13) were adjusted by modifying the mainstream velocity while the jet Reynolds number was kept constant at a value of $Re_2 = U_2 d/\nu_2 = 4200$. In the case of double row injection, five different overall mass flow ratios were used corresponding to $M$ =0.50, 0.64, 0.78, 0.97 and 1.20 respectively. A correlation for the film cooling effectiveness data was determined in this case. In the case of single row injection, the mass flow ratios used varied between approximately $M = 0.21$ and $M = 1.55$. The effect of the jet Reynolds number was investigated for the case of single row injection of air.

For the CA geometry, measurements of $\eta$ were taken for the case of double row injection of air at a constant jet Reynolds number of $Re_2 = 4200$. In all cases, the reported results represent spanwise-averaged values of film cooling effectiveness ($\bar{\eta}$) obtained by integration of local values of $\eta$ over a spanwise distance $S = 4d$.

For the PVC Geometry, measurements of $\eta$ were made for the case of multiple row and single row injection using air as coolant. For the case of multiple row injection, five different mass flow ratios were used corresponding to $M = 0.6$, 0.8, 1.0, 1.2, and 1.4 respectively. For the case of single row injection, measurements of $\eta$ were made at fixed locations immediately downstream of the film cooling holes, and using mass flow ratios ranging from $M = 0.25$ to $M = 1.2$. For all cases, the jet Reynolds number was kept constant at a value of $Re_2 = U_2 d/\nu_2 = 4200$ and different mass flow ratios were achieved by modifying the mainstream velocity.

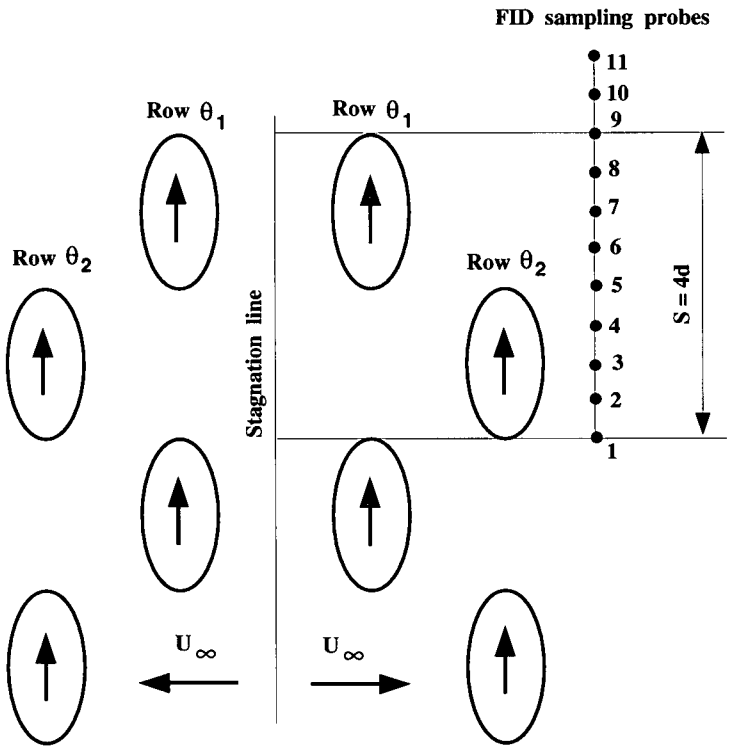


Figure 2.7: Double row injection arrangement.

## 2.3.1 Baseline Geometry

### 2.3.1.1 Double Row Injection

For this case, 2 injection holes were opened in each row while all others were obstructed using a thin tape on the outside of the leading edge. Due to symmetry, measurements were taken only on one side of the leading edge stagnation line, beginning immediately downstream of the second row of cooling holes. Figure 2.7 shows the hole pattern and the fixed spanwise location of the sampling probes. The relative direction of coolant injection is also shown in Fig. 2.7 as well as the direction of the mainstream flow. The streamwise location of the FID sampling probes was automatically adjusted during the experiments by moving the rake with the FID probes in a direction perpendicular to the stagnation line as shown in Fig. 2.7.

This configuration could be considered representative of an infinite row if $\eta$ values are periodic over the pair of two holes downstream of which measurements were taken. This means that $\eta$ values from the sampling probes number 9, 10, and 11 should be the same as $\eta$

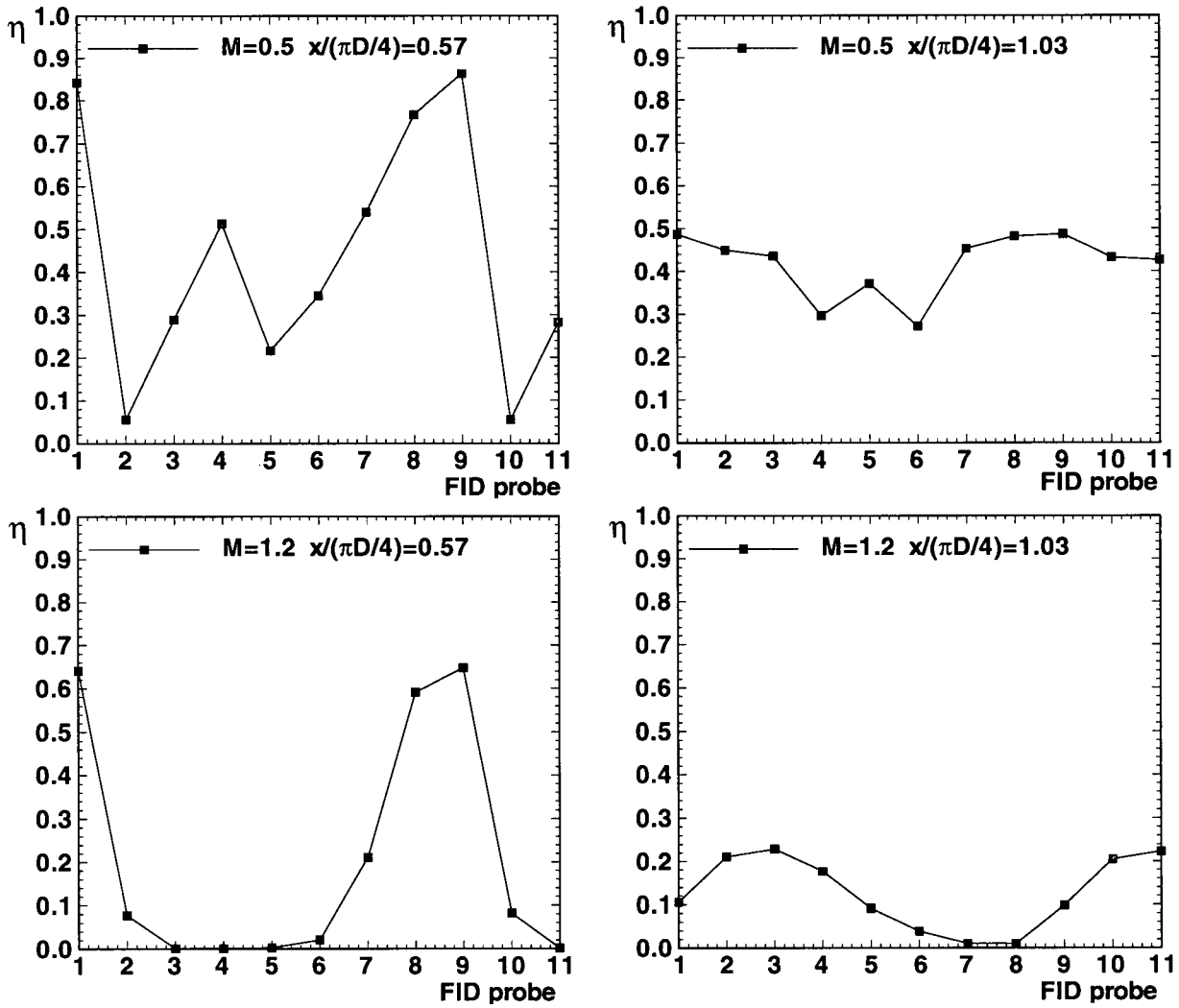


Figure 2.8: Baseline geometry: air, double row injection, periodicity check.

values from the sampling probes number 1, 2, and 3 respectively. This was actually the case during the experiments: Fig. 2.8 presents spanwise distributions of film cooling effectiveness for the lower and higher mass flow ratio used at two streamwise locations placed immediately downstream of the cooling holes and immediately downstream of the cylindrical leading edge on the flat afterbody. Overall, very good periodicity was observed for the streamwise planes passing through at least the sampling probes number 9, 10, and 1 and 2 respectively for all mass flow ratios used in the experiments. Therefore, it was assumed that the arrangement shown in Fig. 2.7 was representative of an infinite row. The values of $\eta$ from probes 1 to 9, between the periodicity planes, were then used to calculate $\bar{\eta}$ according to Eqn. 2.4:

$$\bar{\eta} = \frac{0.5(\eta_1 + \eta_9) + \sum_{i=2}^{i=8} \eta_i}{8} \tag{2.4}$$

A direct comparison of $\bar{\eta}$ for the case of air and $CO_2$ injection is shown in Fig. 2.9. The streamwise position was measured from the stagnation line so that $x/(\pi D/4) = 0$ represents the stagnation line and $x/(\pi D/4) = 1$ represents the end of the semi-cylindrical leading edge and the beginning of the flat afterbody. Streamwise locations $x/(\pi D/4) \leq 1$ are therefore indicative of regions on the round leading edge while streamwise locations $x/(\pi D/4) > 1$ are indicative of regions on the flat afterbody.

The overall mass flow ratio through the cooling holes was calculated based on the total discharge area, the density of the coolant and mainstream gases, and the average coolant velocity for all holes $U_2$. The average coolant velocity for all holes was calculated from the condition that the jet Reynolds number be a constant, and this velocity was used to calculate the jet to mainstream mass flow ratios $M$. For the case of air injection and for all mass flow ratios, $\bar{\eta}$ is highest at the location closest to the injection holes and decreases immediately downstream. For the rest of the circular leading edge region $\bar{\eta}$ is fairly constant. A sudden increase in $\bar{\eta}$ is observed at the measurement location on the afterbody closest to the leading edge for the intermediate mass flow ratios of $M$ =0.64, 0.78, and 0.97. Overall, $\bar{\eta}$ decreases with increasing mass flow ratio being highest at $M = 0.50$ and lowest at $M = 1.20$. On average, a 50% reduction in $\bar{\eta}$ is observed at all streamwise locations when the mass flow

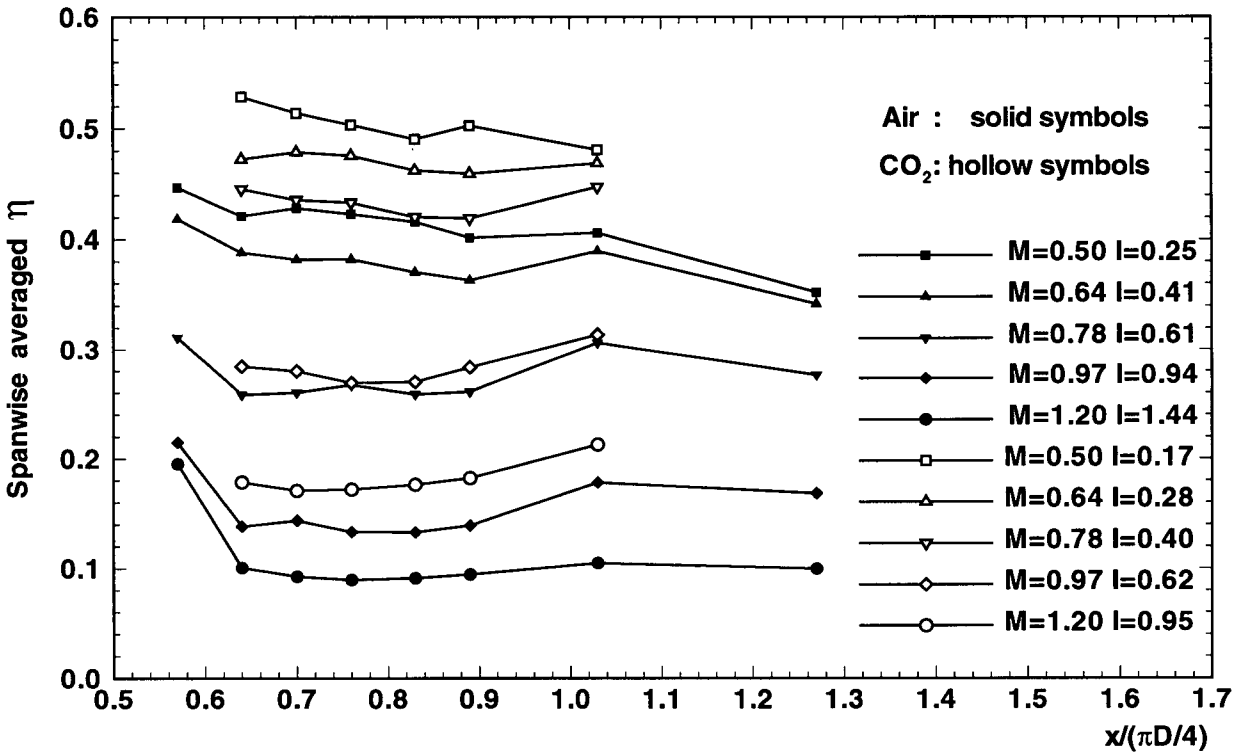


Figure 2.9: Baseline geometry: air and $CO_2$, double row injection.

ratio is increased from $M = 0.78$ to $M = 0.97$.

The injection of $CO_2$ coolant, whose density is about 1.5 times that of air, produced higher values of $\bar{\eta}$ for all mass flow ratios used. The momentum flux ratio $I$ (defined by Eqn. 1.8 on page 13) is the parameter mostly used when comparing $\eta$ values from injection of gases of different densities. Even for the same momentum flux ratios, $\bar{\eta}$ is higher for the case of $CO_2$ injection except for $I = 0.6$ where the results are similar for both air and $CO_2$. This latter situation is shown in detail in Fig. 2.10. It can be seen from this figure that similar $\bar{\eta}$ for air and $CO_2$ cooling were produced by similar area coverage of the cooling jets.

The same trend of decreasing $\bar{\eta}$ with increasing mass flow ratio was observed for injection of $CO_2$ as for injection of air. The highest spanwise-averaged film cooling effectiveness value was around $\bar{\eta} = 0.5$ for the case of $CO_2$ injection at $M = 0.5$.

The fact that higher film cooling effectiveness was achieved at such low mass flow ratio is not necessarily useful in a real gas turbine application. Since all holes at the leading edge are usually fed from a common plenum, the pressure distribution around the leading edge will

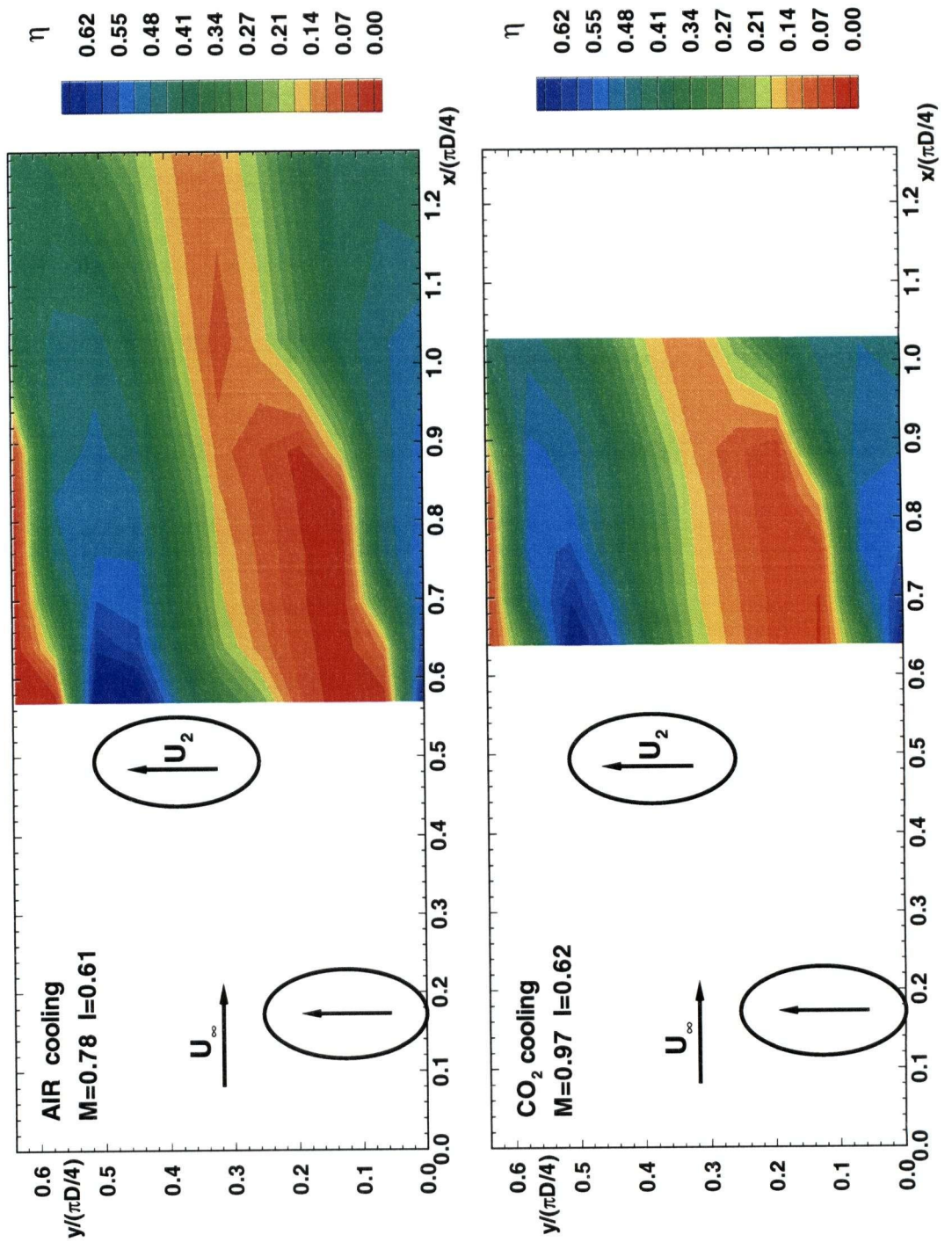


Figure 2.10: Baseline geometry: air and $CO_2$, double row injection, $I = 0.6$.

force the discharge from the holes in row $\theta_1$, closest to the stagnation line, to be less than the discharge from the holes in row $\theta_2$. For the present baseline geometry, complete cutoff of the flow from the holes in row $\theta_1$ occurred at $M = 0.45$ for the case of $CO_2$ injection and at $M = 0.32$ for the case of air injection [44]. For injection at mass flow ratios below these cutoff values, backflow occurs through the row of cooling holes closest to the stagnation line jeopardizing the structural integrity of the blade. A safe backflow margin has to be maintained for all engine operating conditions and this requires the use of higher mass flow ratios.

#### 2.3.1.2 Film Cooling Effectiveness Correlation - Double Row Injection

There are numerous parameters which affect the film cooling performance at the leading edge of turbine blades. For a given leading edge geometry, some of these factors are: position and number of rows of cooling holes, hole spacing in each row, hole spacing in adjacent rows, geometry of the holes, jet to mainstream mass flow/momentum flux ratios, jet to mainstream temperature differences, mainstream turbulence, pressure gradients, relative mainstream to blade angle of attack. Even a brief analysis of the effect of each of these parameters on film cooling effectiveness requires an extensive research program. Design optimization often requires that modifications be made simultaneously to more than one parameter. Consequently, a very large amount of data needs to be analysed at each step in the design and experimentation procedures. In these conditions, the film cooling effectiveness data become useful only if presented in the form of correlations based on the parameters used. These correlations can be more easily implemented in existing design procedures than the raw data, and have the significant advantage that the process can be automated based on continuous feedback. In general, correlations are extensively used in engineering applications and they are even more useful in the complicated conditions found in gas turbines.

For the present study, one of the goals was to develop appropriate correlations for the film cooling effectiveness based on variable coolant density data. The baseline geometry was chosen for investigation. The film cooling effectiveness data for this case was already

presented in Fig. 2.9. For both cases of air and $CO_2$ injection, the spanwise-averaged film cooling effectiveness was fairly constant for most of the leading edge region except for the downstream location closest to the film cooling holes $x/(\pi D/4) = 0.57$. At this location and for the case of air injection, the values of $\bar{\eta}$ are typically higher than farther downstream. For the case of $CO_2$ injection, the same trend was expected immediately downstream of the film cooling holes so that measurements of $\eta$ were only taken at streamwise locations $x/(\pi D/4) \geq 0.64$. In a gas turbine application, the region closest to the film cooling holes benefits from the convection cooling through the cooling holes. Therefore, the focus must be on the leading edge region farther from the cooling holes where lower values of $\eta$ are expected. For the baseline geometry, this region corresponds to streamwise locations $0.64 \leq x/(\pi D/4) \leq 1.0$.

For this region, an area-averaged film cooling effectiveness in spanwise and streamwise directions was introduced to represent the minimum effectiveness that can be expected for the leading edge of the baseline geometry. This parameter is further referred to as $\bar{\bar{\eta}}$ and is defined by Eqn. 2.5:

$$\bar{\bar{\eta}} = \frac{\int_{5d}^{8d} \int_{0}^{4d} \eta dy dx}{4d \times 3d} \tag{2.5}$$

A correlation was developed for $\bar{\bar{\eta}}$ and the results are presented in Fig. 2.11. A third order polynomial fits the data with an error of less than 6.7% for the case of air injection and 7.2% for $CO_2$ injection respectively. The independent variable is represented by a blowing parameter defined by Eqn. 2.6:

$$\xi = \frac{\rho_2 U_2}{\rho_\infty U_\infty} + \left[\frac{\rho_2}{\rho_\infty}\right]^{-\frac{1}{1.41}} - 1 \tag{2.6}$$

where $\xi$ reduces to the mass flow ratio $M$ when $\rho_2 = \rho_\infty$ (air injection into air).

It is understood that the correlation in Fig. 2.11 applies explicitly to the baseline geometry for values of the blowing parameter between $\xi = 0.25$ and $\xi = 1.2$ at constant jet Reynolds number of $Re_2 = 4200$, and for streamwise locations $0.64 \leq x/(\pi D/4) \leq 1.0$. The correlation

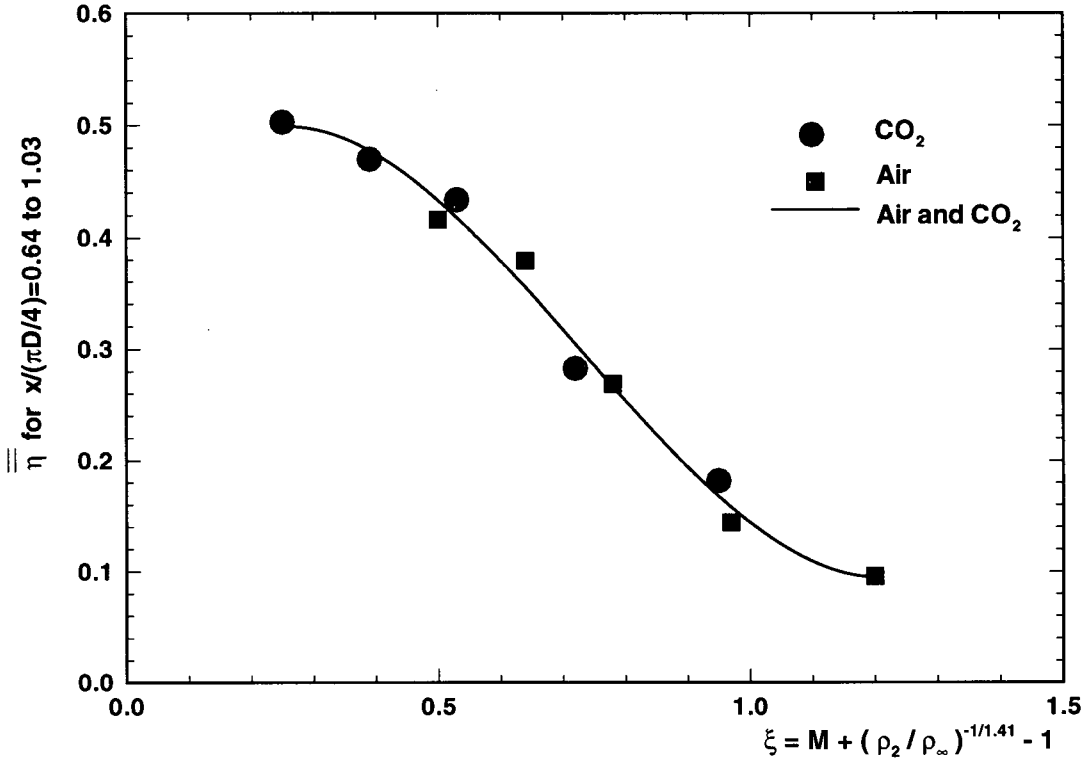


Figure 2.11: Film cooling effectiveness correlation: baseline geometry, double row injection.

in Fig. 2.11 accounts implicitly for the geometrical layout of the baseline geometry with respect to the position of the rows of cooling holes, their relative stagger, and the hole pitch in a row of cooling holes. More experiments are needed using different geometrical layouts to obtain a more complete correlation where the variation of $\bar{\bar{\eta}}$, or possibly the variation of $\bar{\eta}$ itself, is expressed explicitly as a function of the various geometrical parameters involved.

#### 2.3.1.3 Single Row Injection - Constant Jet Reynolds Number

This section presents the results for the case of injection through the holes in either row $\theta_1$ or row $\theta_2$. Perfect symmetry was maintained about the stagnation line; all the holes in row $\theta_2$ were taped and 4 holes were opened in row $\theta_1$ for the case of first row cooling, and *vice versa* all the holes in row $\theta_1$ were taped and 4 holes were opened in row $\theta_2$ for the case of second row cooling. The hole layout used and the fixed spanwise location of the sampling

probes is shown in Fig. 2.12. Only the holes that were opened are shown along with the relative direction of coolant injection and mainstream flow. Again, the rake with the FID sampling probes can only move in a streamwise direction perpendicular to the stagnation line. Two streamwise locations were investigated in each case. The jet Reynolds number was kept constant at a value of $Re_2 = 4200$ and different mass flow ratios were achieved by modifying the mainstream velocity.

In the case of injection through the holes in row $\theta_1$, the effect of the mass flow ratio is illustrated in Fig. 2.13. The values of $\bar{\eta}$ are higher for $CO_2$ injection than for air injection for all mass flow ratios used, and decrease with increasing mass flow ratio. This effect is more pronounced at the location closest to the film cooling holes ($x/(\pi D/4) = 0.32$) where $\bar{\eta}$ decreases more rapidly with increasing mass flow ratio. For all mass flow ratios, $\bar{\eta}$ is higher at the streamwise location closest to the row of cooling holes than at the location farther downstream. Values of $\bar{\eta}$ should have a peak for some value of the mass flow ratio $M > 0$ since $\bar{\eta} = 0$ for $M = 0$. The exact values of the peak $\bar{\eta}$ could not be determined in this case due to limitations of mainstream velocity so that lower mass flow ratios could not be produced.

Figure 2.14 shows the effect of mass flow ratio at two different streamwise locations for the case of injection through the holes in row $\theta_2$. The location $x/(\pi D/4) = 0.64$ was immediately downstream of the cooling holes and the other streamwise location was farther downstream on the flat afterbody. Peak values of $\bar{\eta}$ are evident at both streamwise locations and are similar for both air and $CO_2$. These peak values of $\bar{\eta}$ occur at lower mass flow ratio for air and at higher mass flow ratio for $CO_2$, as expected since the air coolant has a higher injection momentum at the same $M$ than the $CO_2$ coolant. The values of $\bar{\eta}$ are higher at the streamwise location closest to the injection holes than farther downstream for a wide range of $M$ for both air and $CO_2$ cooling, but the differences become smaller with increasing mass flow ratio. For air cooling, the values of $\bar{\eta}$ are eventually the same at the two streamwise locations for $M \geq 1$. The peak values of $\bar{\eta}$ are some 50% higher at the location closest to the cooling holes than at the location on the flat afterbody. Overall, the use of the $CO_2$ coolant

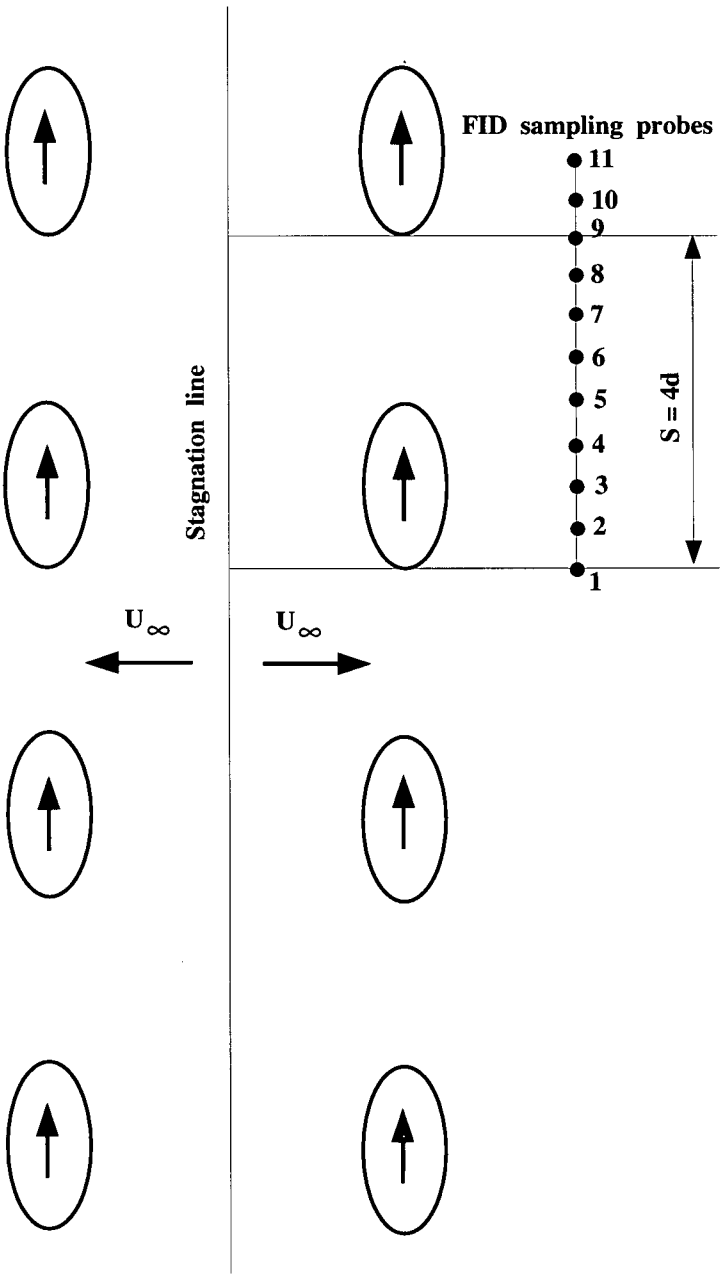


Figure 2.12: Single row injection arrangement.

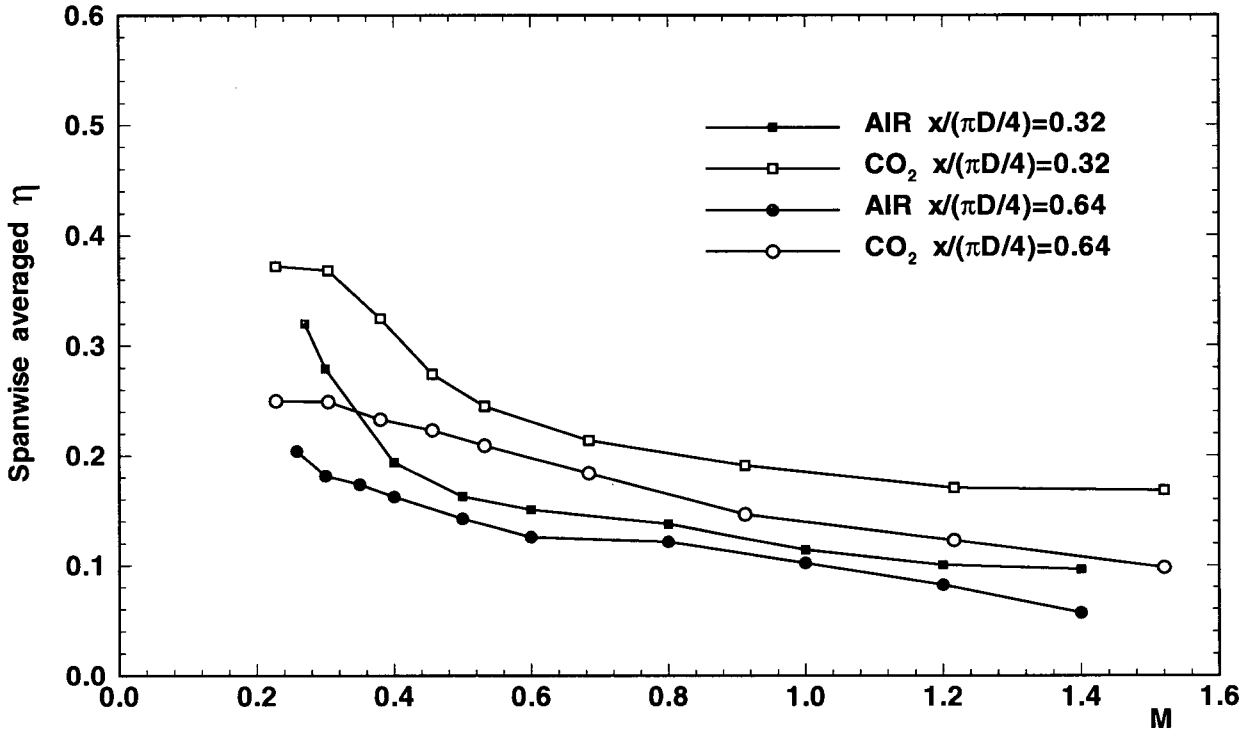


Figure 2.13: Baseline geometry - row $\theta_1$ cooling: effect of mass flow ratio.

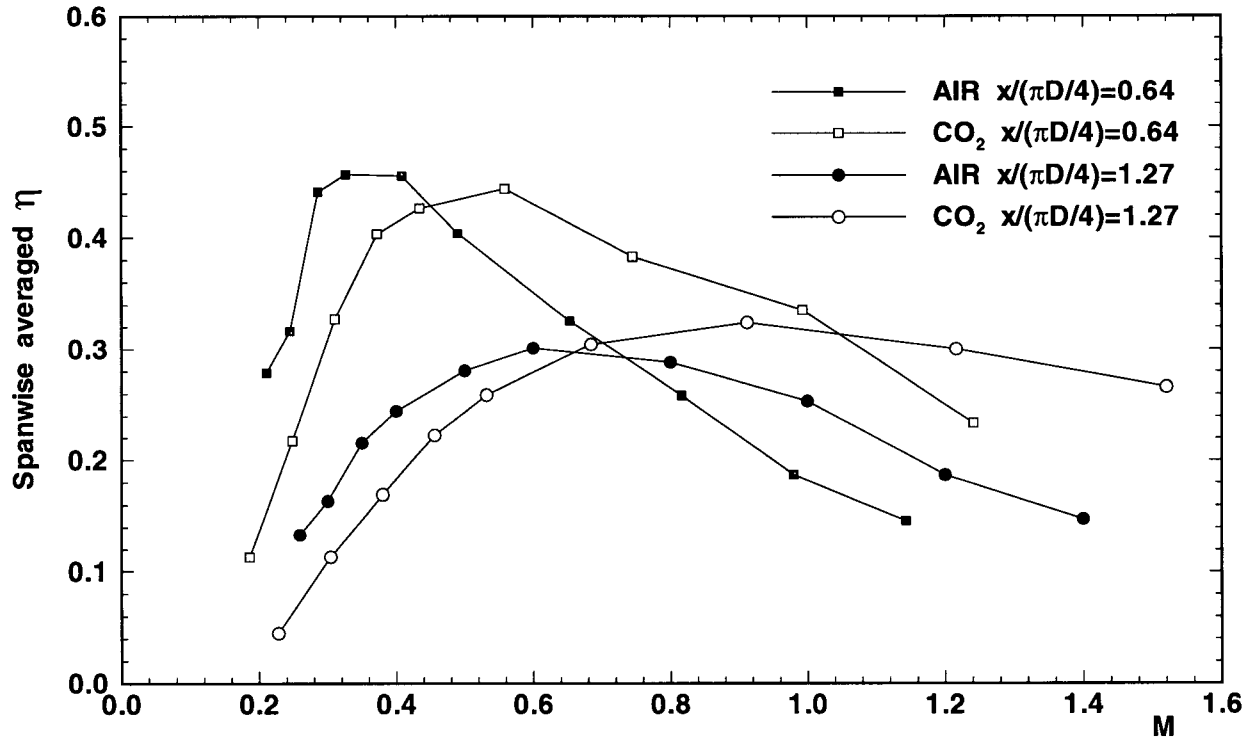


Figure 2.14: Baseline geometry - row $\theta_2$ cooling: effect of mass flow ratio.

is more effective at higher $M$. For mass flow ratios greater than about 0.68, $\bar{\eta}$ is higher for $CO_2$ injection than for air injection at both streamwise locations investigated.

The above analysis, based on the overall mass flow ratio, is consistent with the general approach from published film cooling literature. Nevertheless, since the exact location of the rows of cooling holes on the semi-cylindrical leading edge is known, a local mass flow ratio or momentum flux ratio can be calculated based on the local velocity outside the boundary layer just upstream of the cooling holes. The local velocity approaching the holes at $15^0$ and $44^0$ on the cylindrical surface can be calculated from the pressure coefficient measured at these positions. The usual pressure coefficient is defined by Eqn. 2.7 for this low-speed flow:

$$C_p = \frac{p_\theta - p_\infty}{\frac{1}{2}\rho_\infty U_\infty^2} = 1 - \frac{U_\theta^2}{U_\infty^2} \tag{2.7}$$

where $\theta$ is the angle around the cylinder measured from the stagnation line, $p_\theta$ and $U_\theta$ are the static pressure and the local velocity outside the boundary layer respectively. The pressure coefficient is about $C_p = 0.77$ for the holes at $\theta = 15^0$ and about $C_p = -0.5$ for the holes at $\theta = 44^0$ [20]. The local momentum flux ratio $I_\theta$ can then be determined from the overall mass flow ratio $M$, the pressure coefficient $C_p$, and the coolant to mainstream density ratio $\rho_2/\rho_\infty$ according to Eqn. 2.8:

$$I_\theta = \frac{\rho_2 U_2^2}{\rho_\infty U_\theta^2} = \left[\frac{\rho_2 U_2}{\rho_\infty U_\infty}\right]^2 \frac{U_\infty^2}{U_\theta^2}\frac{\rho_\infty}{\rho_2} = \frac{M^2}{\frac{\rho_2}{\rho_\infty}(1 - C_p)} \tag{2.8}$$

The results from Fig. 2.13 and Fig. 2.14 are replotted in terms of the local momentum flux ratio in Fig. 2.15 and Fig. 2.16 respectively. For the case of injection through the holes at $15^0$, the spanwise-averaged film cooling effectiveness is still higher at the same local momentum flux ratio for $CO_2$ injection than for air injection.

For the case of injection through the holes at $44^0$, $\bar{\eta}$ is the same at lower $I_\theta$ for both air and $CO_2$ injection. The peak values of $\bar{\eta}$ still occur at lower $I_\theta$ for air injection than for $CO_2$ injection, but appear much closer when plotted in terms of local momentum flux ratio than in terms of overall mass flow ratio. Immediately downstream of the cooling holes, the peak

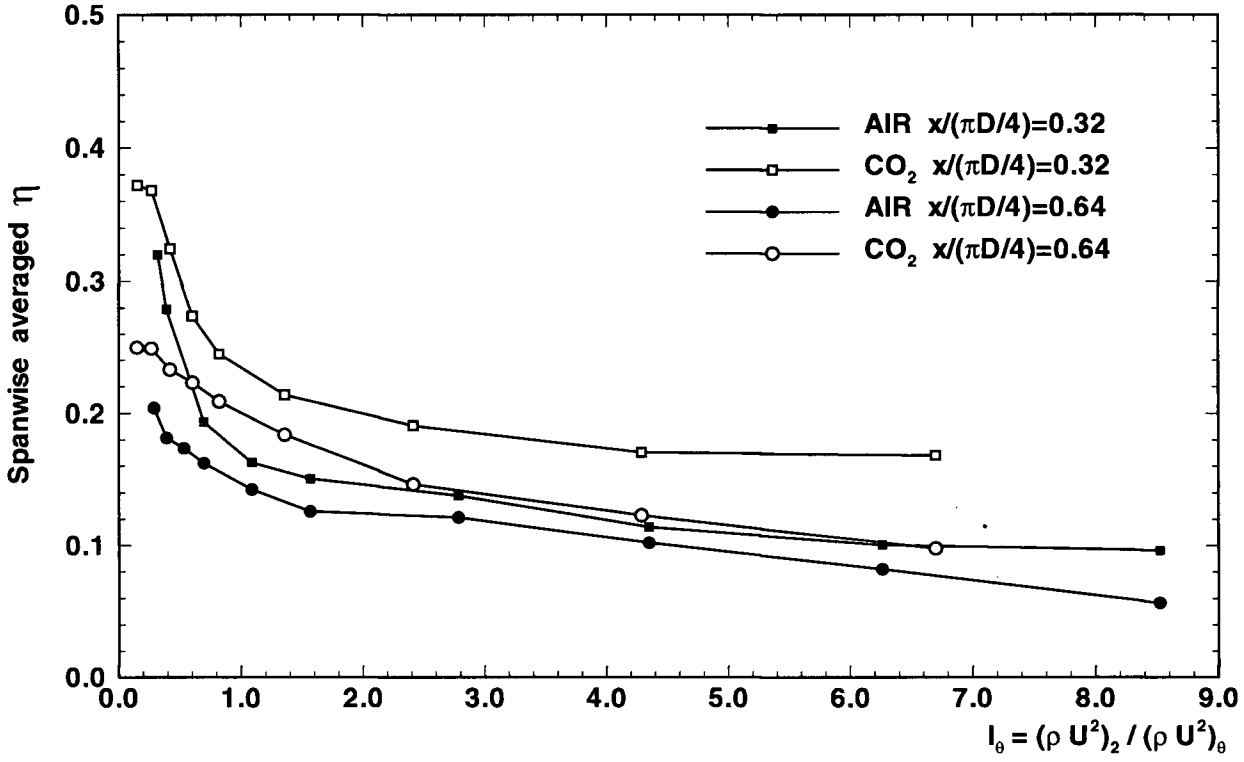


Figure 2.15: Baseline geometry - row $\theta_1$ cooling: effect of local momentum flux ratio.

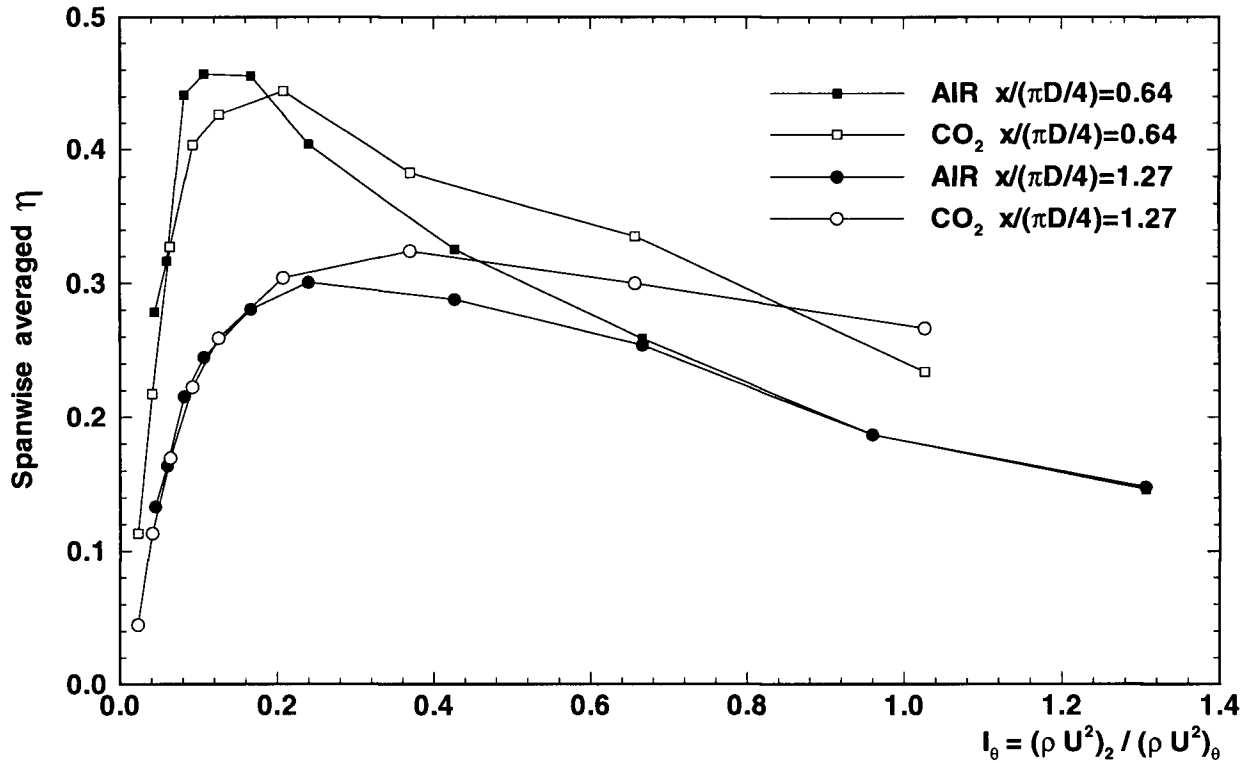


Figure 2.16: Baseline geometry - row $\theta_2$ cooling: effect of local momentum flux ratio.

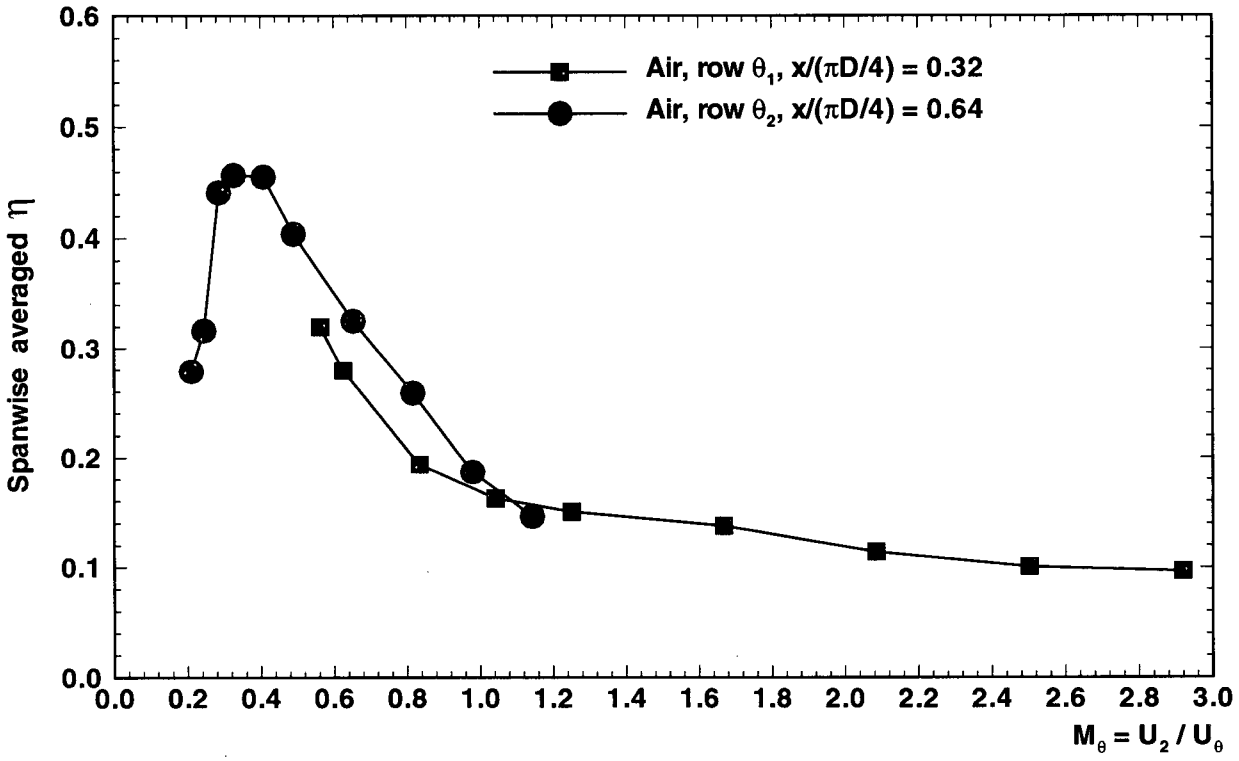


Figure 2.17: Baseline geometry - single row air injection: effect of local mass flow ratio.

$\bar{\eta}$ occurs at about $I_\theta = 0.15$ for air injection and at about $I_\theta = 0.20$ for $CO_2$ injection. For values of local momentum flux ratio greater than about $I_\theta = 0.2$, $CO_2$ injection provides better $\bar{\eta}$ than air injection.

Although the local momentum flux ratio does not completely correlate the spanwise-averaged film cooling effectiveness for the case of single row injection, some trends were better represented in terms of $I_\theta$ than in terms of $M$. It is therefore recommended that this approach be pursued for future analysis of single row injection with variable density coolant.

Immediately downstream of the rows of cooling holes, the spanwise-averaged film cooling effectiveness results are expressed in terms of the local mass flow ratio $M_\theta$ in Fig. 2.17 and Fig. 2.18 for air injection into air and for $CO_2$ injection into air respectively. The local mass flow ratio is defined by Eqn. 2.9 with the use of the pressure coefficient defined by Eqn. 2.8:

$$M_\theta = \frac{\rho_2 U_2}{\rho_\infty U_\theta} = M\frac{U_\infty}{U_\theta} = \frac{M}{\sqrt{1 - C_p}} \tag{2.9}$$

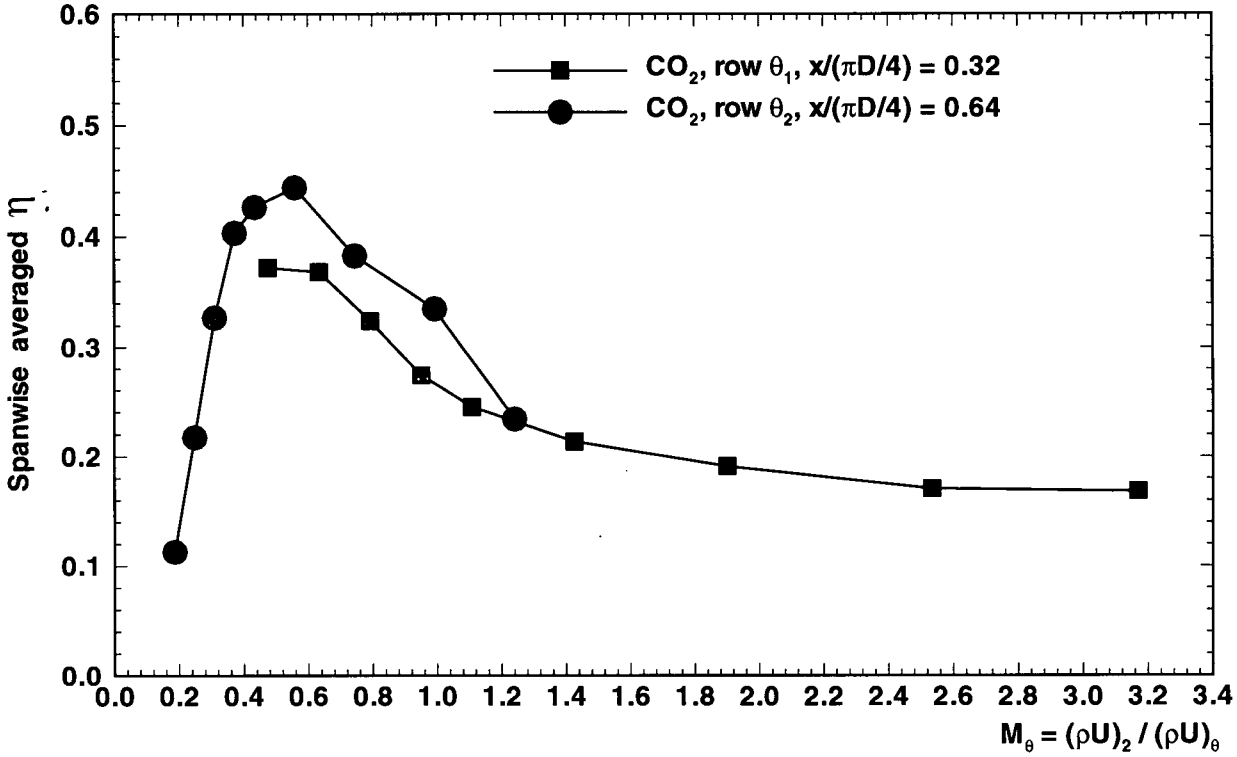


Figure 2.18: Baseline geometry - single row $CO_2$ injection: effect of local mass flow ratio.

For a given geometry, it was expected that local conditions at the point of injection characterise the film cooling effectiveness immediately downstream of the cooling holes, and that the trends be similar regardless of the position of the cooling holes on the cylindrical leading edge surface. The results in Fig. 2.17 and Fig. 2.18 support this assumption and $\bar{\eta}$ values from row $\theta_1$ match reasonably the values from row $\theta_2$ immediately downstream of the cooling holes for the same local mass flow ratios. The differences are probably due to the interaction between the jets and the boundary layer at the location of the cooling holes and immediately downstream. The actual velocity profile at the exit of the cooling holes might also change with row position around the cylindrical leading edge; since the holes are fed from a common plenum, the flow entrance conditions are not the same for holes placed at different angles around the cylindrical surface. This effect is not captured by the local mass flow ratio but some trends can be clearly observed from Fig. 2.17 and Fig. 2.18 respectively; both figures show a peak $\bar{\eta}$ at relatively low $M_\theta$, and the peak $\bar{\eta}$ was the same for both cases of air injection and $CO_2$ injection with a value around $\bar{\eta} = 0.45$. The peak $\bar{\eta}$ occured at

a lower $M_\theta$ in the case of air injection than in the case of $CO_2$ injection. For both cases, a further increase of the local mass flow ratio caused a decrease in $\bar{\eta}$. For higher values of $M_\theta$, the spanwise-averaged film cooling effectiveness was higher for $CO_2$ injection than for air injection.

The analysis based on the local mass flow ratio $M_\theta$ could be used in the future to quantify the effect of single row injection and different hole geometries for a given coolant gas, while the local momentum flux ratio $I_\theta$ is useful, especially for lower values of $I_\theta$, when analysing the effect of variable density coolant for a given hole geometry.

#### 2.3.1.4 Single Row Injection - The Effect of Jet Reynolds Number

The effect of jet Reynolds number on film cooling effectiveness was investigated for the case of single row injection. For each row, measurements of $\eta$ were taken at two streamwise locations downstream of the injection holes using air as coolant. These locations were immediately downstream of the holes in row $\theta_1$ ($x/(\pi D/4) = 0.32$), immediately downstream of the holes in row $\theta_2$ ($x/(\pi D/4) = 0.64$), and on the flat afterbody ($x/(\pi D/4) = 1.27$). For each fixed jet Reynolds number, the mass flow ratio was adjusted by modifying the mainstream velocity.

Figure 2.19 shows spanwise-averaged film cooling effectiveness $\bar{\eta}$ for air injection through the holes in row $\theta_1$ at the streamwise location closest to the holes. There are no significant differences in the values of $\bar{\eta}$ over the range of Reynolds numbers investigated, except at the lowest mass flow ratio of $M = 0.2$. At this low mass flow ratio, $\bar{\eta}$ decreases some 30% with increasing jet Reynolds number from $Re_2 = 846$ to $Re_2 = 2540$. Overall, $\bar{\eta}$ decreases with increasing mass flow ratio and this trend is more pronounced at lower mass flow ratios $M \leq 0.4$. At the location farther downstream, the effect of jet Reynolds number on $\bar{\eta}$ is presented in Figure 2.20. Here too, $\bar{\eta}$ decreases with increasing mass flow ratio for all jet Reynolds numbers but the effect is more pronounced at the lower jet Reynolds numbers used. For the lowest mass flow ratio used $M = 0.2$, $\bar{\eta}$ drops again significantly with increasing jet Reynolds number from $Re_2 = 846$ to $Re_2 = 2540$.

For the case of air injection through the holes in row $\theta_2$, the effect of jet Reynolds number

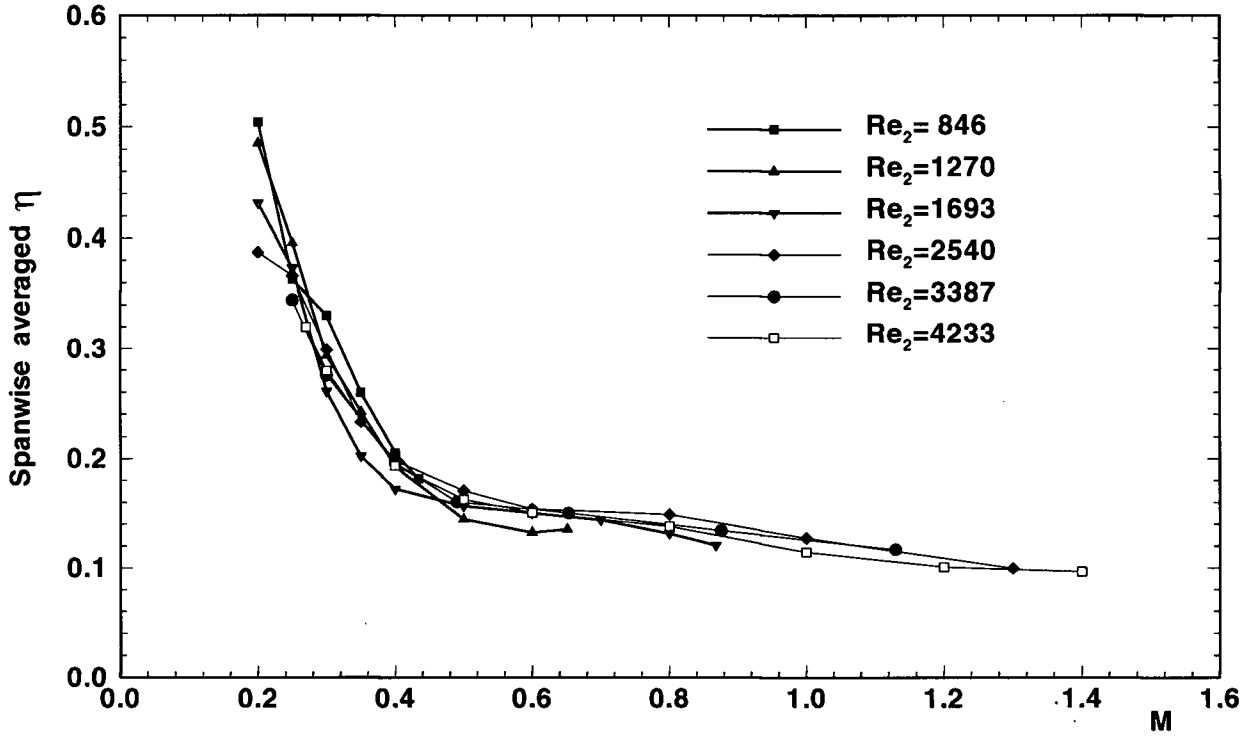


Figure 2.19: Baseline geometry - row $\theta_1$ air cooling: $x/(\pi D/4) = 0.32$.

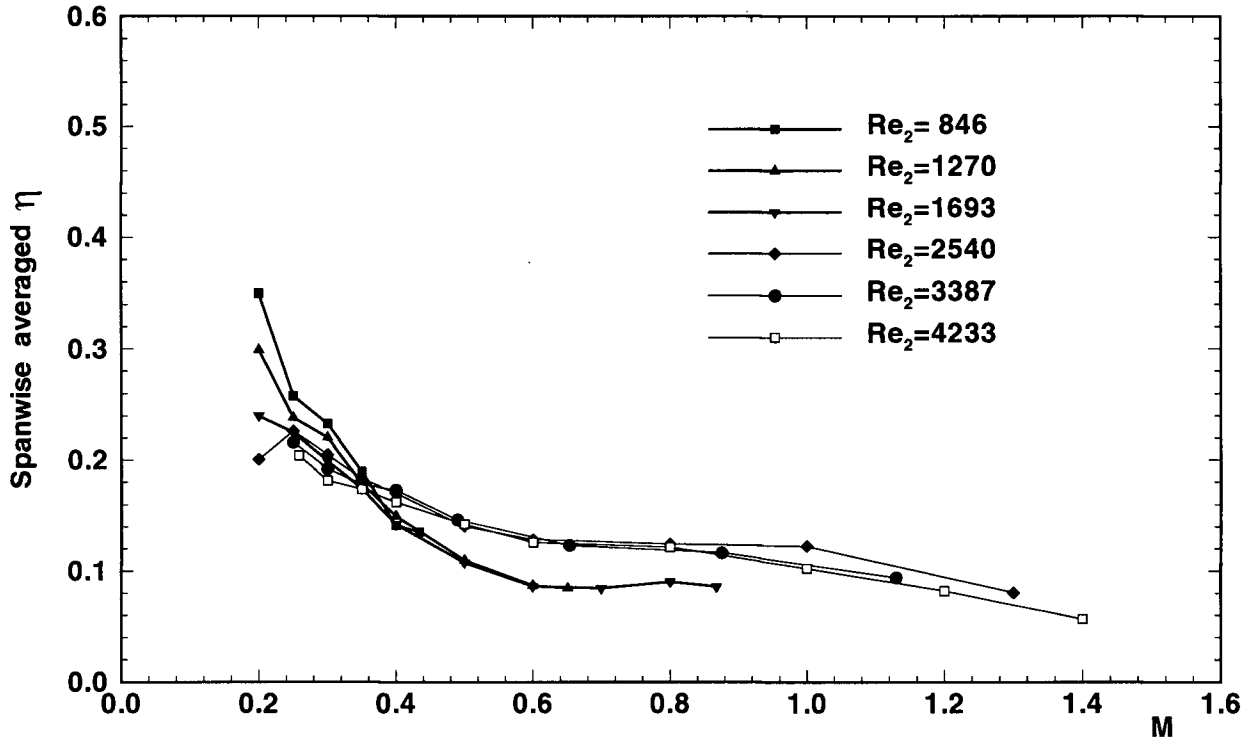


Figure 2.20: Baseline geometry - row $\theta_1$ air cooling: $x/(\pi D/4) = 0.64$.

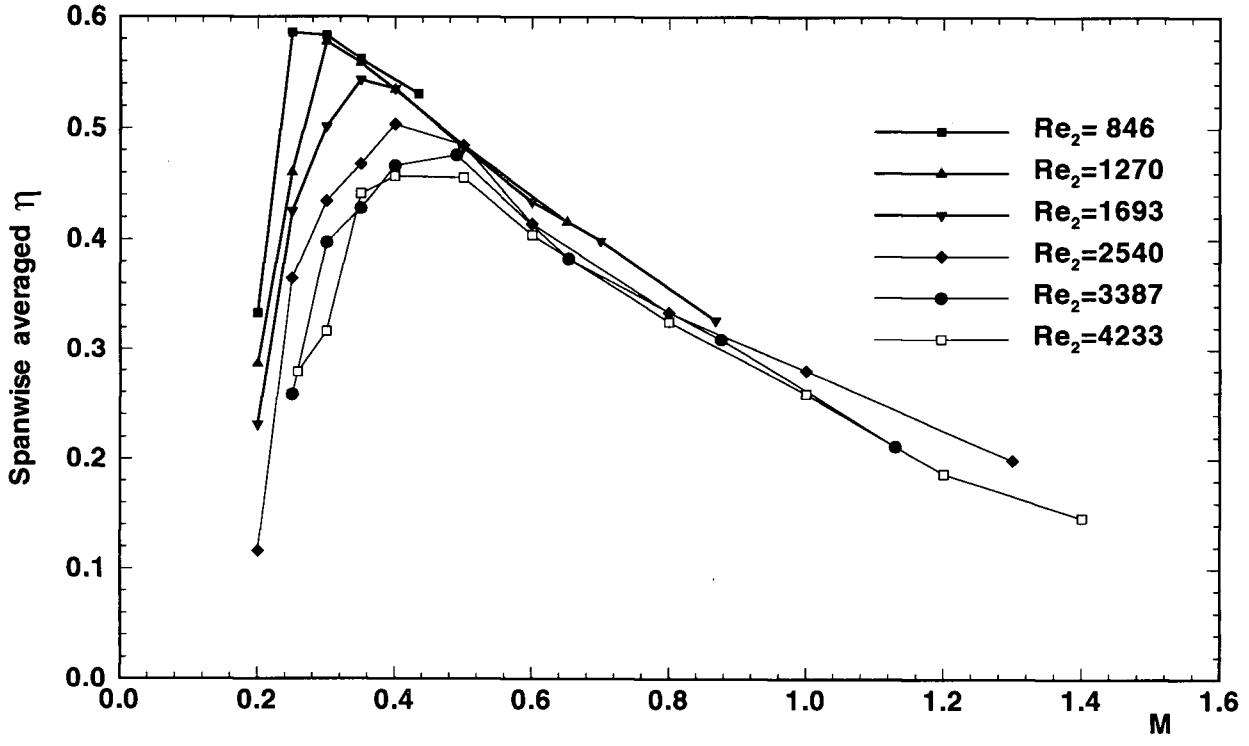


Figure 2.21: Baseline geometry - row $\theta_2$ air cooling: $x/(\pi D/4) = 0.64$.

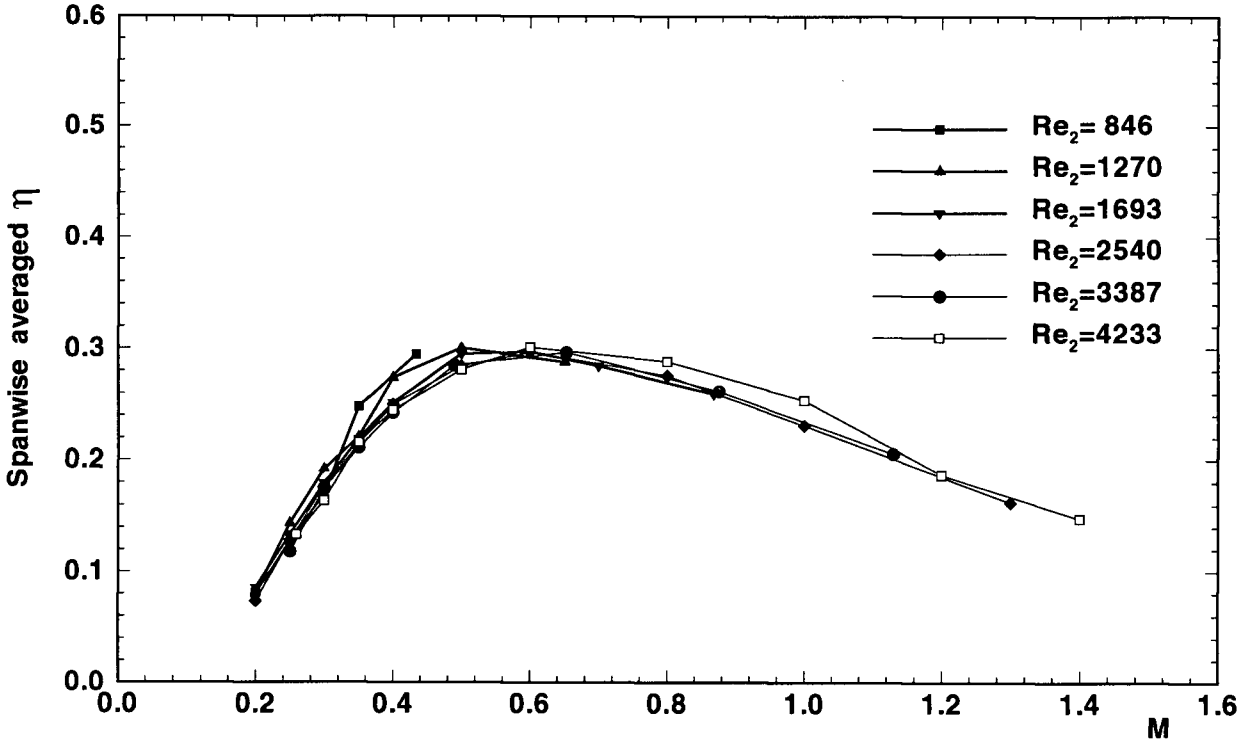


Figure 2.22: Baseline geometry - row $\theta_2$ air cooling: $x/(\pi D/4) = 1.27$.

is presented in Fig. 2.21 and Fig. 2.22 for streamwise locations immediately downstream of the cooling holes and farther downstream on the flat afterbody respectively. The jet Reynolds number clearly affects the peak $\bar{\eta}$ at the streamwise location closest to the cooling holes. The peak $\bar{\eta}$ occurs at lower mass flow ratio for lower $Re_2$ and at higher mass flow ratio for higher $Re_2$, as expected. The values of $\bar{\eta}$ are also some 26% higher at the lower jet Reynolds number of $Re_2 = 846$ than at the higher jet Reynolds number of $Re_2 = 4233$. For mass flow ratios higher than about $M = 0.5$, the values of $\bar{\eta}$ are basically independent of the jet Reynolds number and $\bar{\eta}$ decreases with increasing mass flow ratio. At the location on the flat afterbody, $\bar{\eta}$ is clearly independent of the jet Reynolds numbers used and $\bar{\eta}$ has a peak at about $M = 0.6$.

### 2.3.2 CA Geometry

Figure 2.23 shows the comparison of spanwise-averaged film cooling effectiveness for the case of multiple row air injection for the baseline and CA geometries. The same procedure and setup described in section 2.3.1.1 were used to obtain film cooling effectiveness at a constant jet Reynolds number $Re_2 = 4200$ for the CA geometry.

The compound angle of the cooling holes provides significantly higher $\bar{\eta}$ for the CA geometry than for the baseline geometry for all mass flow ratios investigated. The effect is most beneficial especially for regions closer to the cooling holes. For the CA geometry, a peak in $\bar{\eta}$ occurs at the streamwise location $x/(\pi D/4) = 0.64$. The spanwise-averaged film cooling effectiveness decreases at locations farther from the cooling holes, and it decreases more rapidly for the lower mass flow ratios than for the higher mass flow ratios. The differences in $\bar{\eta}$ for the two geometries become less significant at locations on the flat afterbody. The highest values of $\bar{\eta}$ occur at the lowest mass flow ratios investigated $M = 0.64$ for the CA geometry and $M = 0.50$ for the baseline geometry respectively.

More significant was the improvement in $\bar{\eta}$ for the CA geometry at mass flow ratios farther from the cutoff values of row $\theta_1$ of cooling holes. For example, $\bar{\eta}$ is on average some 90% higher for the CA geometry than for the baseline geometry at the intermediate mass flow

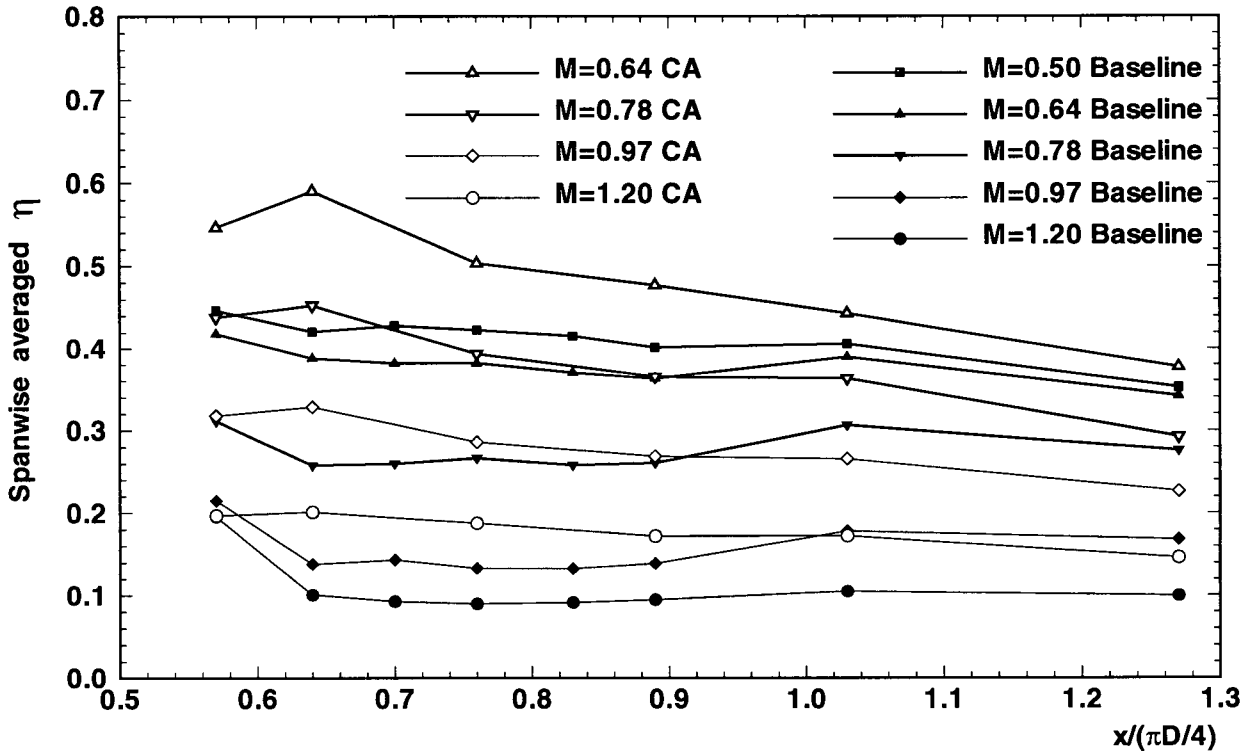


Figure 2.23: Spanwise averaged $\eta$ for baseline and CA geometries.

ratio $M = 0.97$. This trend is maintained even at the highest mass flow ratio investigated of $M = 1.2$ where $\bar{\eta}$ is on average some 70% higher for the CA geometry than for the baseline geometry.

Figure 2.24 shows the effect of geometry more simply in terms of the area-averaged film cooling effectiveness $\bar{\bar{\eta}}$ for the streamwise region between $x/(\pi D/4) = 0.64$ and $x/(\pi D/4) = 1.03$, and for a spanwise region $S = 4d$ downstream of the cooling holes. For the CA geometry, the analysis based on $\bar{\bar{\eta}}$ is not very accurate since the spanwise-averaged film cooling effectiveness clearly decreases with increasing streamwise distance from $x/(\pi D/4) = 0.64$ to $x/(\pi D/4) = 1.03$ for all mass flow ratios investigated. Nevertheless, the use of $\bar{\bar{\eta}}$ provides a simple and clear qualitative indication of the overall improved film cooling performance of the CA geometry which is attributed to the compound angle $\psi = 33^0$ of the cooling holes. This angle represents the only geometrical parameter that was different for the CA geometry than for the baseline geometry where $\psi = 0^0$.

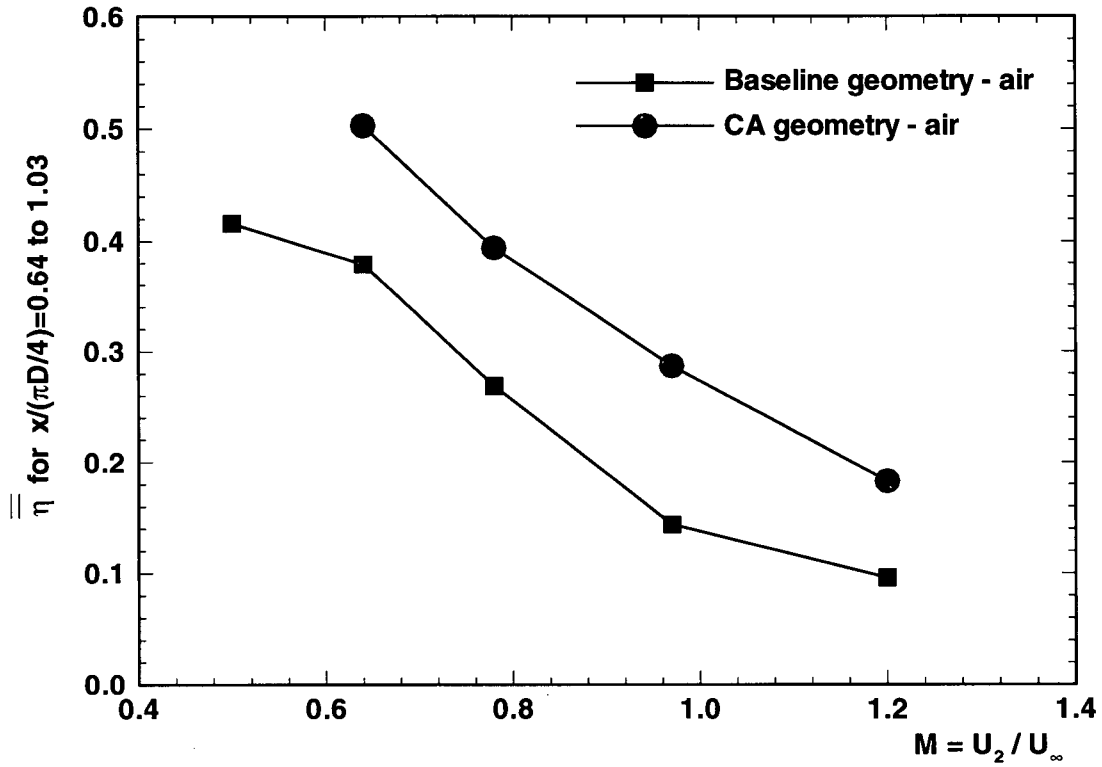


Figure 2.24: Comparison of baseline and CA geometries: $\bar{\eta}$, double row air injection.

### 2.3.3 PVC Geometry

#### 2.3.3.1 Double Row Injection

Figure 2.25 shows the layout used and the spanwise location of the FID sampling probes. For this case, 5 injection holes were opened in each row. The sampling probes covered a fixed spanwise region of $S = 7.5d$ and were only allowed to move in a streamwise direction, that is, perpendicular to the geometrical leading edge, along the lines shown in Fig. 2.25. This arrangement was chosen to be representative of an infinite row. The streamwise location of the sampling probes was automatically adjusted using the same hardware and software described in section 2.2.4. The total streamwise region covered by the sampling probes was from $x/(\pi D/4) = 0.46$ to $x/(\pi D/4) = 1.23$. The values of $\eta$ from all probes were used to calculate the spanwise-averaged film cooling effectiveness $\bar{\eta}$. The measurements were

taken on one side of the geometrical leading edge beginning with a location immediately downstream of row $\theta_2$ of cooling holes.

Figure 2.26 shows a comparison of the spanwise-averaged film cooling effectiveness for the PVC and baseline geometries for mass flow ratios $M \geq 0.6$. For the PVC geometry, the highest $\bar{\eta}$ was achieved at the lower mass flow ratio $M = 0.6$ for the streamwise region immediately downstream of the cooling holes, and at $M = 0.8$ for streamwise regions farther away from the cooling holes. Overall, there are little differences in the values of $\bar{\eta}$ for the lower mass flow ratios used, $M = 0.6$ and $M = 0.8$. At higher mass flow ratios, $\bar{\eta}$ decreased with increasing mass flow ratio; the same trend of decreasing $\bar{\eta}$ with increasing mass flow ratio was observed previously for both baseline and CA geometries.

At the lower mass flow ratio $M = 0.64$, the baseline geometry provides only slightly higher $\bar{\eta}$ than the PVC geometry at $M = 0.6$. For higher mass flow ratios, the PVC geometry provides significantly higher $\bar{\eta}$ than the baseline geometry. For the mass flow ratio $M = 1.0$, $\bar{\eta}$ for the PVC geometry is on average almost twice the $\bar{\eta}$ values for the baseline geometry. This situation is shown in more detail in Fig. 2.28. Even at $M = 1.4$, the values of $\bar{\eta}$ farther away from the cooling holes are higher for the PVC geometry than for the baseline geometry at $M = 1.2$. Also, for the PVC geometry, the values of $\bar{\eta}$ for mass flow ratios of $M = 1.0$, 1.2 and 1.4 show little variation with the streamwise coordinate for locations on the cylindrical region of the leading edge.

A comparison of $\bar{\eta}$ for the PVC and CA geometries is presented in Fig. 2.27. At the lower mass flow ratio $M = 0.64$, the CA geometry provides higher $\bar{\eta}$ than the PVC geometry at $M = 0.6$ and $M = 0.8$. At $M = 0.8$, $\bar{\eta}$ is slightly higher for the CA geometry than for the PVC geometry. For all other higher mass flow ratios investigated, the PVC geometry provides higher $\bar{\eta}$ than the CA geometry and the differences are more significant at locations farther away from the cooling holes.

The area-averaged film cooling effectiveness can be used to summarize qualitatively the relative performance of the baseline, CA, and PVC geometries. Figure 2.29 shows the variation of $\bar{\bar{\eta}}$ calculated for a streamwise region from $x/(\pi D/4) = 0.64$ to $x/(\pi D/4) = 1.03$

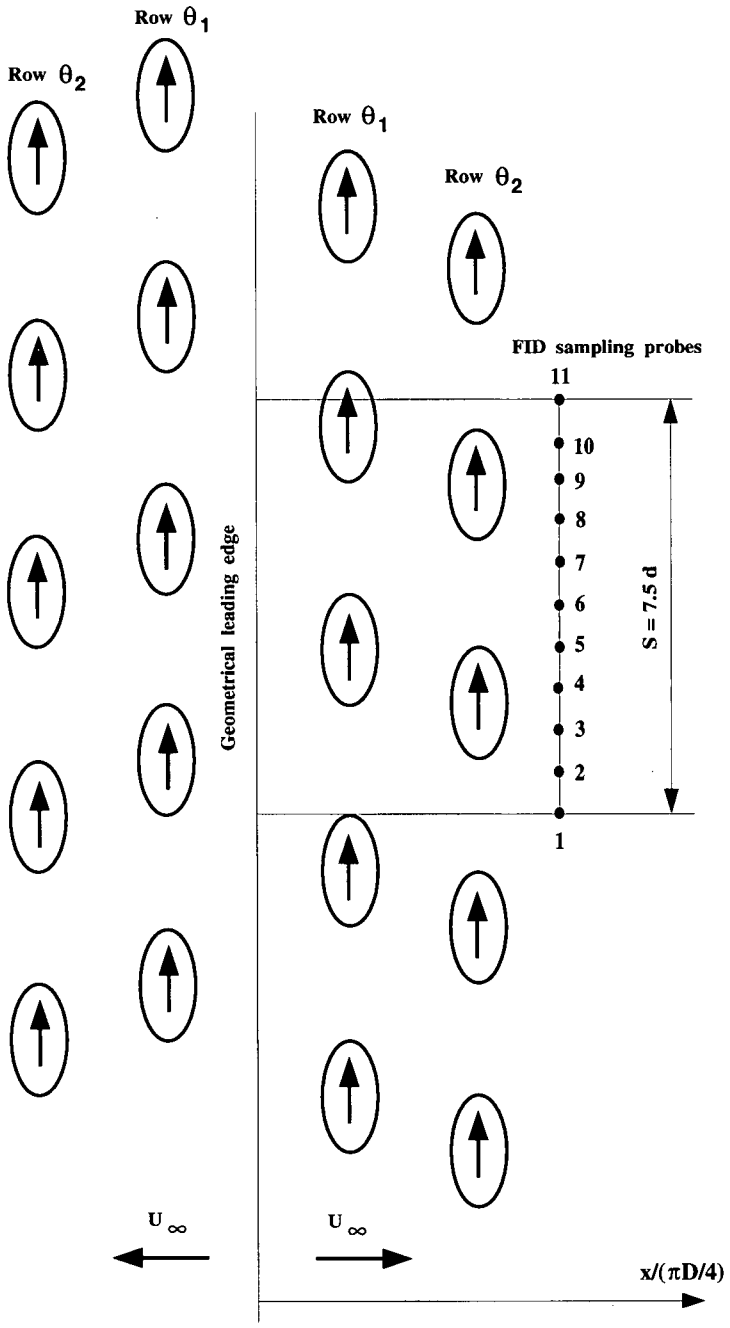


Figure 2.25: Injection arrangement for the PVC geometry.

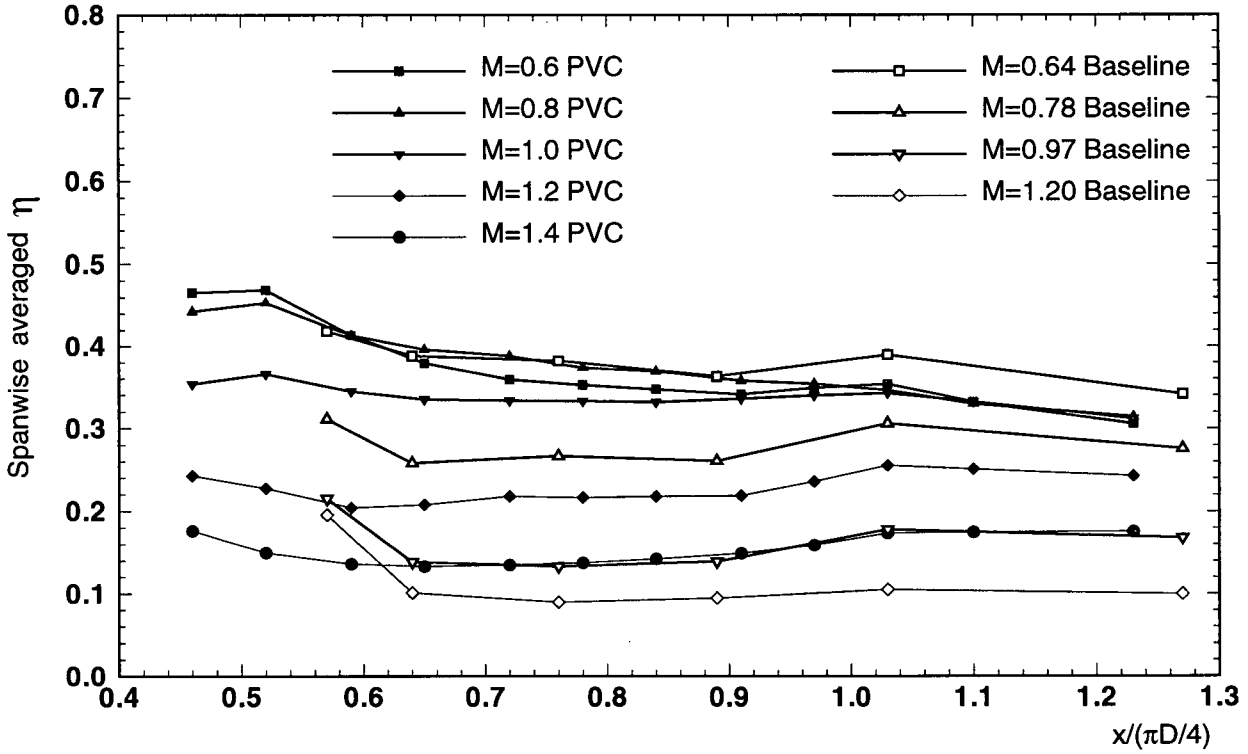


Figure 2.26: Comparison of PVC and Baseline geometries: air, double row injection.

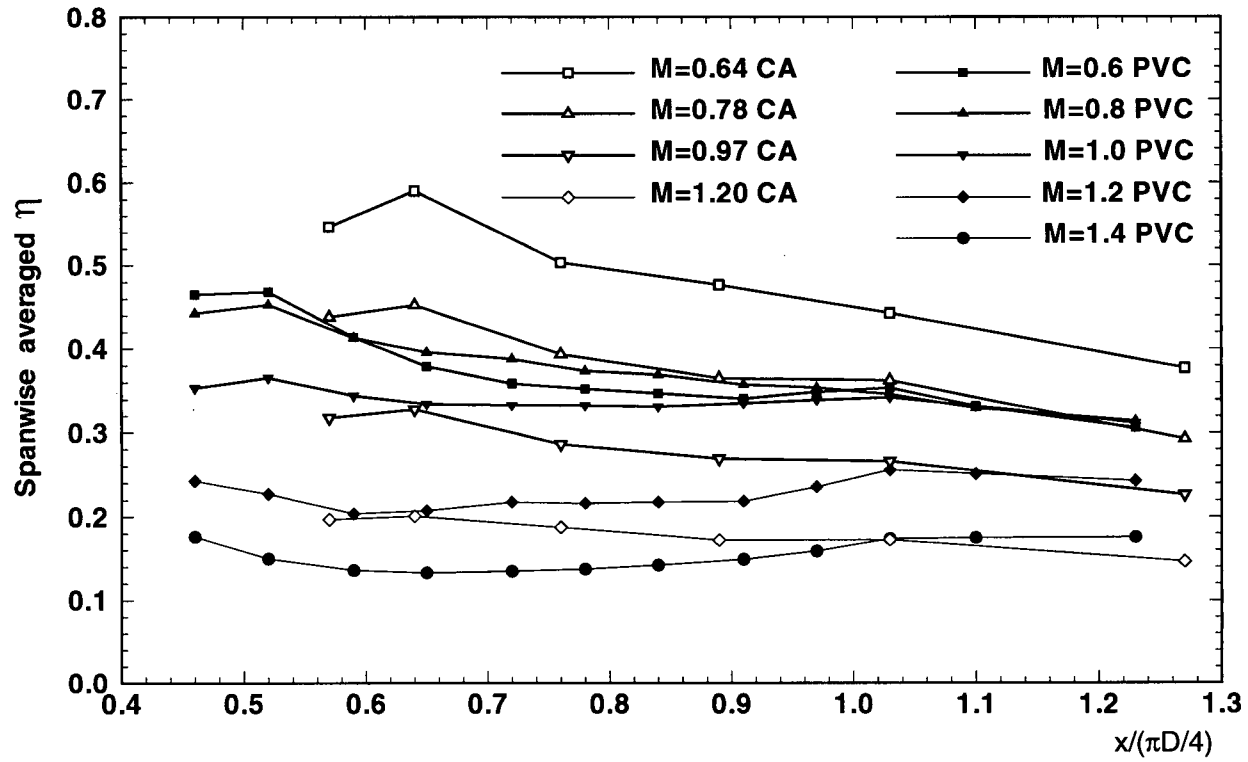


Figure 2.27: Comparison of PVC and CA geometries: air, double row injection.

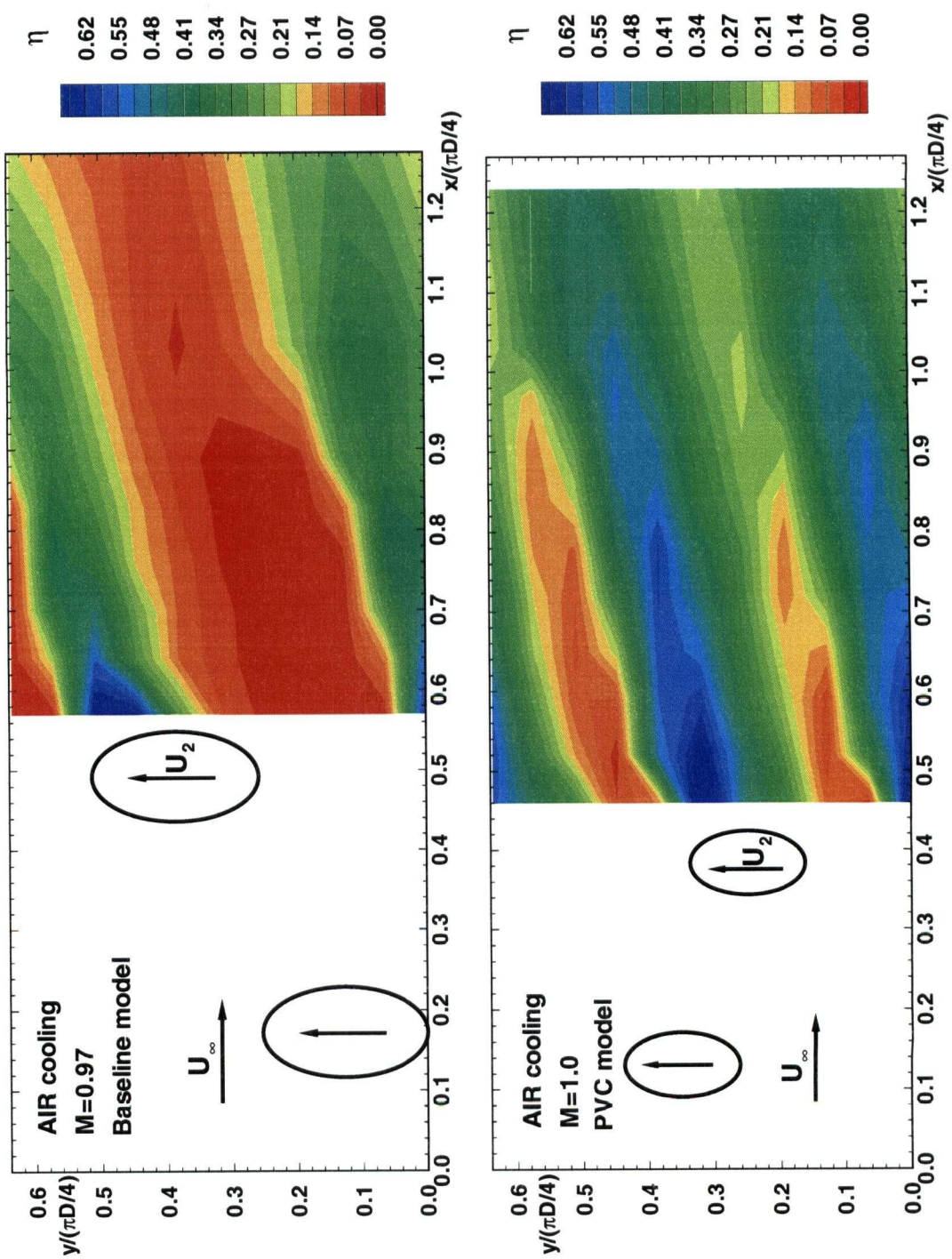


Figure 2.28: PVC and Baseline geometries: air, double row cooling at $M = 1.0$.

against the mass flow ratio for the case of double row air injection for the three geometries investigated.

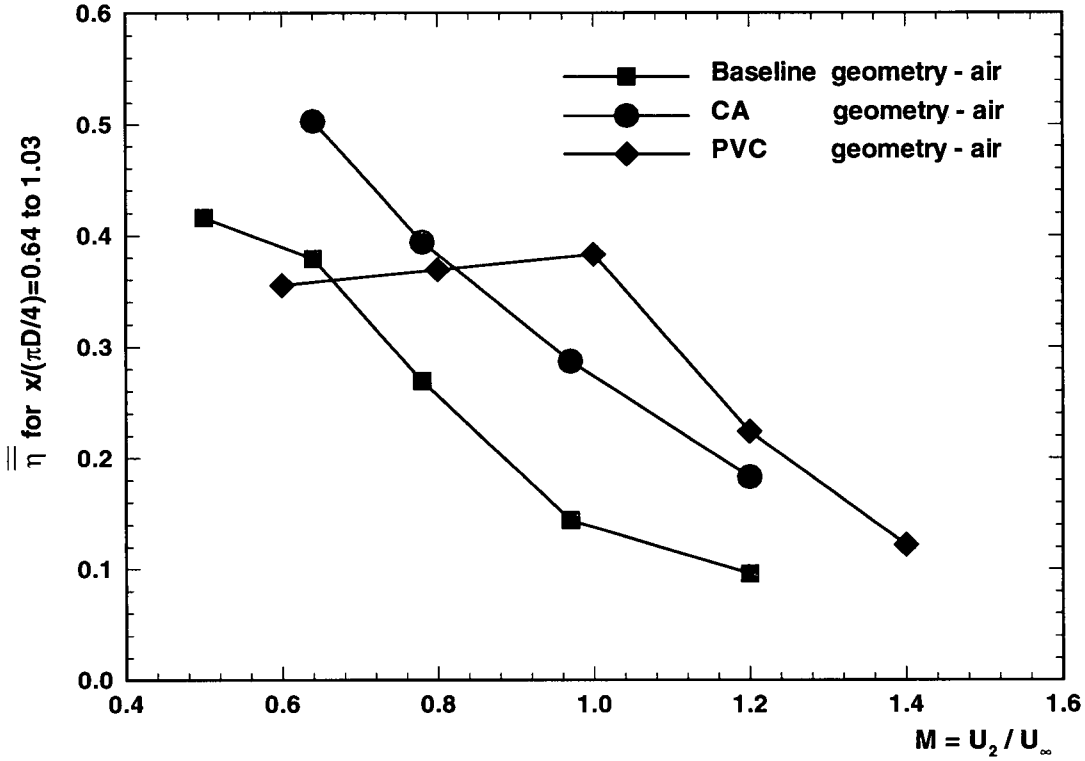


Figure 2.29: PVC, Baseline, and CA geometries - $\bar{\bar{\eta}}$: air, double row cooling.

The comparison of $\bar{\eta}$ presented in Fig. 2.26 and Fig. 2.27 and the comparison of $\bar{\bar{\eta}}$ presented in Fig. 2.29 clearly show the improved film cooling performance of the PVC geometry at higher mass flow ratios. This allows the cooling system to operate with good efficiency while providing the necessary backflow margin at different engine operating conditions. This was actually the main objective of the design of the PVC geometry. This also proves that a design procedure must include the effect of different geometrical parameters such as row location, hole geometry and position in a row of cooling holes, and relative stagger of the row of cooling holes.

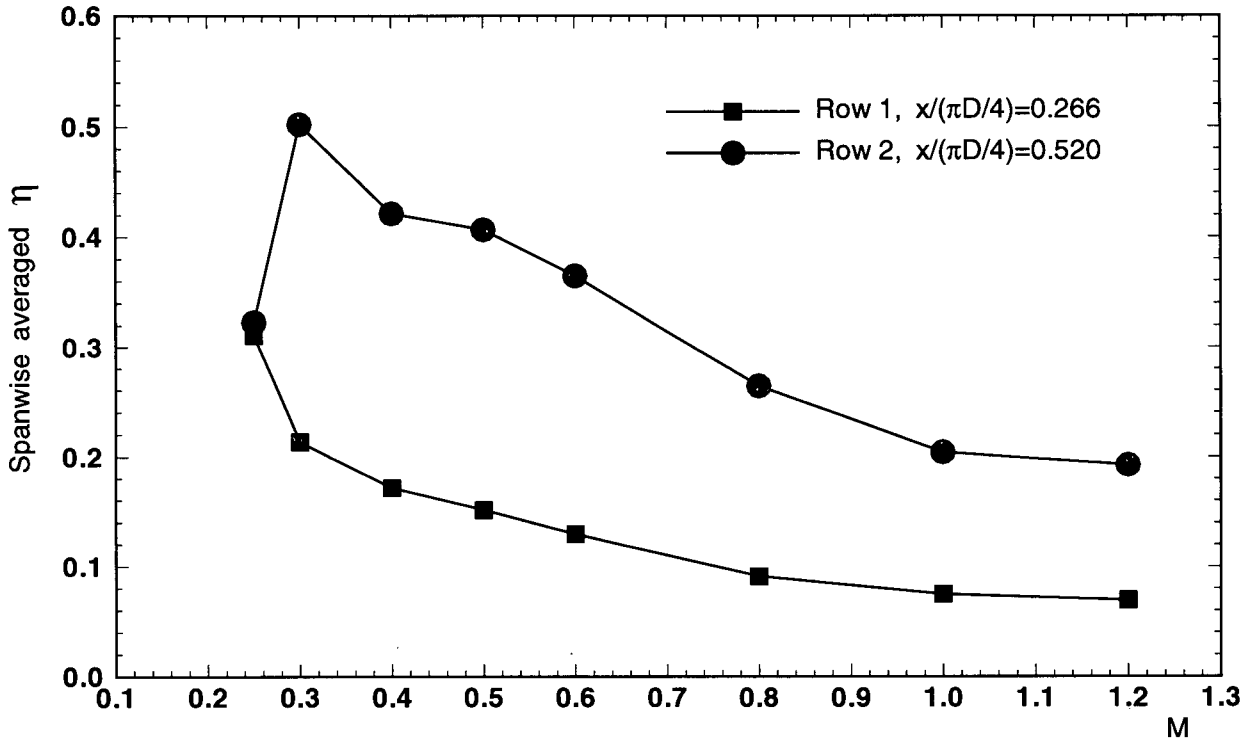


Figure 2.30: PVC geometry: single row cooling, effect of $M$.

#### 2.3.3.2 Single Row Injection

Figure 2.30 presents the effect of the overall mass flow ratio for the case of injection through the holes in row $\theta_1$ and row $\theta_2$ respectively. Five holes were opened in either row $\theta_1$ or row $\theta_2$ and the corresponding layout of the cooling holes and the spanwise position of the sampling probes were the same as described in Fig. 2.25. The streamwise location $x/(\pi D/4) = 0.266$ was immediately downstream of row $\theta_1$ of cooling holes and the streamwise location $x/(\pi D/4) = 0.52$ was immediately downstream of row $\theta_2$ of cooling holes.

For the entire range of mass flow ratios investigated, the spanwise-averaged film cooling effectiveness was higher for the case of injection through the holes in row $\theta_2$ than for injection through the holes in row $\theta_1$. This behaviour was actually expected since the actual mainstream velocity approaching the holes in row $\theta_1$ is less than that approaching the holes in row $\theta_2$ just outside of the boundary layer. Therefore, for the same mass flow ratio $M$, the local mass flow ratio $M_\theta$ is higher for the holes in row $\theta_1$ than for the holes in row $\theta_2$. When

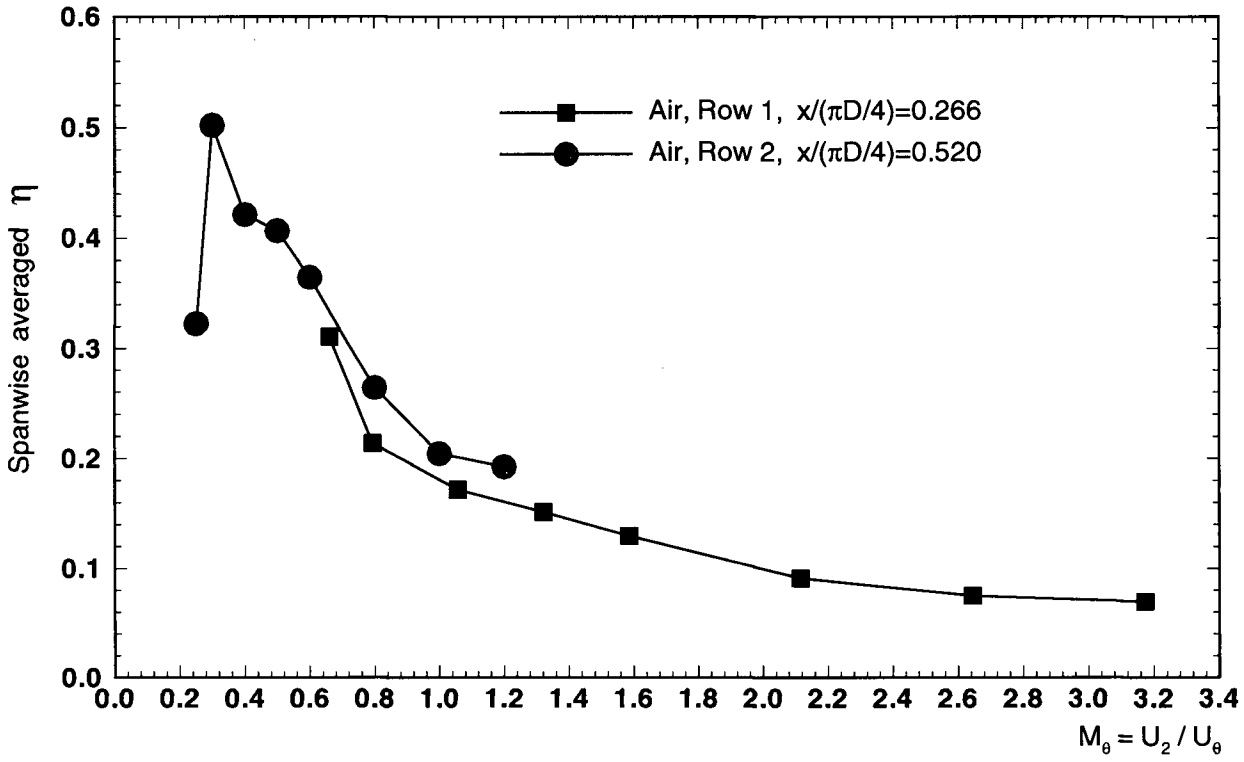


Figure 2.31: PVC geometry: single row cooling, effect of $M_\theta$.

the local mass flow ratio $M_\theta$ is considered, the variation of $\bar{\eta}$ is as shown in Fig. 2.31. The local velocity approaching the holes just outside the boundary layer was found from experimental pressure coefficient data [20] by the method described in section 2.3.1.3. Figure 2.31 shows clearly that the local conditions at the jet exit are more important than the relative position of the rows of cooling holes. For a given hole geometry, the same $\bar{\eta}$ can be expected just downstream of the cooling holes for the same local coolant discharge regardless of the streamwise position of the cooling holes. The fact that the values of $\bar{\eta}$ do not completely overlap at the same $M_\theta$ is probably mostly due to the slight differences in the hole geometry which is a feature of the PVC geometry, and to the differences in the boundary layers approaching the two rows of holes.

For this case of single row air injection, $\bar{\eta}$ values from Fig. 2.31 can be compared with $\bar{\eta}$ values for the baseline geometry from Fig. 2.17 on page 51. The peak $\bar{\eta}$ occurs at approximately the same local mass flow ratio $M_\theta = 0.3$ for both geometries, and the peak value is only slightly higher for the PVC geometry than for the baseline geometry. The trends are

clearly preserved in both cases and variations are probably due to the difference in the exit hole geometry. For many purposes, a single plot of $\bar{\eta}$ versus $M_\theta$ could be used for all hole locations and for these two hole geometries. The effects of hole geometry in this plot are not very significant.

## 2.4 Summary

For the case of multiple row injection using the baseline and CA geometries, the use of the higher density $CO_2$ coolant provided higher film cooling effectiveness for all mass flow ratios investigated.

Higher values of $\bar{\eta}$ always occurred at lower mass flow ratios, and film cooling effectiveness decreased with increasing mass flow ratio for both baseline and CA geometries used.

Significant improvement of the blade leading edge film cooling effectiveness was achieved for the CA geometry with the use of compound angle holes. This proves the importance of geometrical parameters in the design of film cooling systems.

For a specified leading edge region of the baseline geometry, the area-averaged film cooling effectiveness data were correlated based on a newly defined blowing parameter.

For the case of single row injection using the baseline geometry, higher values of $\bar{\eta}$ were achieved from injection through the holes at $\pm 44^0$ than through the holes at $\pm 15^0$. The use of the $CO_2$ coolant provided higher film cooling effectiveness than the air coolant particularly at higher local momentum flux ratios.

For the baseline geometry, the effect of jet Reynolds number on the spanwise-averaged film cooling effectiveness in not significant in the case of air injection from row $\theta_1$ except at the lowest mass flow ratio investigated of $M = 0.2$. At this mass flow ratio, $\bar{\eta}$ decreases significantly with increasing $Re_2$. For the case of air injection from row $\theta_2$, higher peak values of $\bar{\eta}$ were obtained at the lowest jet Reynolds number used of $Re_2 = 846$, and the peak $\bar{\eta}$ decreases with increasing jet Reynolds number and also occurs at higher mass flow ratio. Overall, the jet Reynolds number has no significant effect on $\bar{\eta}$ at higher mass flow

ratio.

For the case of double row injection using the PVC geometry, the spanwise-averaged film cooling effectiveness was significantly higher than $\bar{\eta}$ values for the previously tested baseline and CA geometries for mass flow ratios $M > 0.64$ and $M > 0.8$ respectively.

For the case of single row injection using the PVC geometry, the $\bar{\eta}$ results immediately downstream of the injection holes were consistent with the values from the baseline geometry when the local mass flow ratio was used as the scaling parameter. The spanwise-averaged film cooling effectiveness has a peak at a relatively low local mass flow ratio and $\bar{\eta}$ further decreases with increasing local mass flow ratio.

For a given hole geometry, the $\bar{\eta}$ values from injection through holes at arbitrary locations around the cylindrical leading edge can be predicted with reasonable accuracy when local mass flow ratios are considered.

# Chapter 3

# Liquid Crystal Thermography

This section describes the measurement of wall temperature distributions based on the colour change of a thermochromic liquid crystal. Various colour imaging systems are analysed and the development of a high performance imaging system is presented. The concepts developed here have application in convective heat transfer studies where a temperature difference exists between an arbitrary surface and the surrounding incompressible flow. The developed concepts relate also to more general applications where non-intrusive thermal mapping of an arbitrary surface is needed.

## 3.1 Thermochromic Liquid Crystals

Detailed distributions of the external heat transfer coefficient together with the film cooling effectiveness parameter are necessary in the design of film cooled turbine vanes and blades. The film cooling layer has to protect the airfoil for some region downstream of the injection sites, and thus high resolution mapping of relatively large regions is required. Some of the techniques most widely used for measuring surface heat transfer in the past, as reviewed in [36], are not flexible enough for investigating many different geometries with minimum instrumentation costs. Quite often, significant modifications have to be made in order to accomodate a new geometry, and serious complications arise when more complicated and

irregular surfaces need to be investigated. For example, heat flux gages together with surface thermocouples have been successfully used in the past for convective heat transfer studies, and are still used in situations where the geometry is fixed and only the flow conditions and the temperature fields are changing. They provide good local representation of the heat transfer process, but detailed mapping would necessitate multiple probes with accompanying high instrumentation costs.

The turbine cooling designer on the other hand, requires not only the investigation of a fixed geometry under various flow and temperature field conditions, but also the comparison of many different complicated geometries for identical surrounding conditions. One of the goals of this study is to develop a technically sound and economically viable experimental program to meet the designer's need for flexibility, close to real-time output of the results, and sufficient accuracy to allow sensible integration of the preliminary external heat transfer performance with the assumed available aerodynamics and heat transfer numerical routines. A detailed temperature distribution on the surface of interest would prove sufficient when the analysis follows the principles discussed in section 4.1 of this study. The focus has to be then on choosing a method that will grant high resolution thermal mapping over a large region of interest of possible irregular shape.

Two such methods have been identified from the literature as suitable candidates, one is based on infrared thermography and the other is based on liquid crystal thermography. Both techniques are non-intrusive. The surface of interest is coated with high emissivity paints and thermochromic liquid crystals respectively, and the probing device (an infrared camera and a video camera respectively) is placed at some distance from the surface, thus causing no disturbance to the generated flowfield.

Infrared thermography is based on capturing the radiation from a surface onto a thermal detector in the probing device scanning the surface, and digitizing the generated signal to store the emitted intensity values in a computer data acquisition system. Ultimately, a calibration procedure relates the scanned intensity values with the respective local surface temperatures. With proper calibration to accont for the multiple sources of uncertainty (like op-

tical aberrations, radiation contributions from neighbouring elements, hysteresis associated with the camera scan-frequency, etc.), and with appropriate image reconstruction techniques, temperature measurements with accuracies as good as $0.3 - 0.4^0C$ can be achieved [34]. Although attractive, the high costs of the infrared probe makes the technique prohibitively expensive for lower budget research facilities. The alternate liquid crystal thermographic technique is clearly much more feasible from an economic point of view, and also has the technical potential of producing accurate results as suggested by studies in the past. The concepts and principles associated with this technique will be further documented and developed in this study.

Thermochromic liquid crystals change colour when subjected to various temperatures. The colour change is reversible and this makes them suitable for repeated use. Liquid crystals are in fact organic molecules which exhibit the flow properties of a liquid and some of the optical properties of a crystalline solid. The discovery of the liquid crystalline state lies with the research performed separately in the late nineteenth century by an Austrian botanist, Freidrich Reinitzer, and a German physicist, Otto Lehmann [60], [9]. It was not until 1970s that the general public was exposed to this technology through an application related to the display industry. Ever since, liquid crystal technology has found numerous applications in many industrial and research fields such as medical thermography, non-destructive testing, heat transfer and flow visualisation, battery testing, scientific instrumentation, and of course, various liquid-crystal-based electro-optic display applications, to name only a few. An increasing amount of dedicated literature in now available for both the novice and the specialist. A thorough introductory description of the liquid crystals was found in [9].

A thermochromic liquid crystal is optically active above a certain temperature called the melting point, and below a temperature called the clearing point. The melting point temperature for a particular liquid crystal compound represents the temperature at which the crystalline solid will begin to melt, and the clearing point represents the temperature above which the liquid crystal behaves entirely as a liquid losing the optical properties associated

with the crystalline solid phase. Liquid crystals are more similar to liquids than they are to solids, having only a small amount of additional order. A typical liquid crystal molecule would be elongated in shape, with some rigidity in the central region and with the ends somewhat flexible. The molecules orient themselves along a certain direction in space called director, and this is intrinsic to their anisotropy.

The most common classification of the liquid crystal phases identifies them as smectic (the most solid-like phase), nematic (the degree of molecular order is smaller than in smectics), and chiral nematic (Greek words for the exhibited twisted structure of this phase). In a multi-layered chiral nematic liquid crystal the molecular director rotates about an axis in a helical fashion, the molecules in each layer being on average oriented along the director. A pitch length can be thus defined as the distance in the layers of molecules for a $360^0$ rotation of the director. When white light is incident on a chiral nematic liquid crystal, most of it will be transmitted with some optical activity through the liquid crystal compound, and only the wavelength equal to the pitch will be reflected parallel to the direction perpendicular to the liquid crystal. At any other viewing angle the wavelength reflected is less, with the wavelength decreasing as the viewing angle (defined with respect to the direction perpendicular to the liquid crystal) increases, as shown in Fig. 3.1.

With chiral nematic liquid crystal, the longest wavelength for a specific temperature will be therefore observed on directions perpendicular to the liquid crystal, and for any departure from this direction shorter wavelengths (towards blue hues) will be observed. This is an important aspect that experimentalists using these materials have to compensate for through proper spatial calibrations. A compound that will exhibit minimal colour change with the viewing angle is desirable since it could be used on round surfaces without the need for more complicated spatial calibrations.

For maximum visualisation of the reflected colours, the thermochromic liquid crystal colour change is always viewed against a black absorbing background. The intensity of the produced colours is directly dependent on the available light. Since the pitch in the liquid crystal is a function of the temperature of the compound, TLC's can be manufactured to

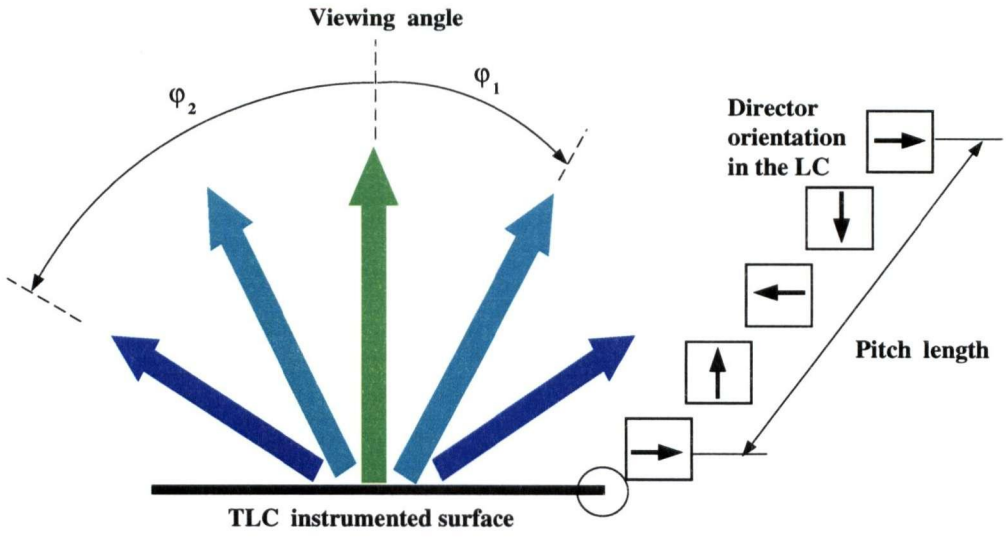


Figure 3.1: Effect of the viewing angle on the observed colour of a chiral nematic liquid crystal.

exhibit the entire colour spectrum. Red appears first immediately after the melting point followed by yellow, green, cyan, blue and purple hues as the temperature increases. After the clearing point, the compound becomes clear again and the black colour of the background is observed. A schematic of the temperature-colour relationship is depicted in Fig. 3.2.

The displayed colours of the liquid crystal appear in reverse order when cooling the compound, with violet appearing first immediately below the clearing point, red immediately above the melting point, and back to clear below the melting point. The temperature range between the melting and clearing points is also known as the thermochromic liquid crystal band. A band as narrow as $1^0C$ is possible and the liquid crystal will selectively reflect all the colours in the visible spectrum over such a temperature range. Wide-band liquid crystals can also be custom manufactured by combining different narrower band liquid crystals and exhibit the same colour change over a wider temperature range. The viewed colours would change more slowly over this wider temperature range. Various thermochromic liquid crystal manufacturers can presently produce mixtures in any temperature between $-30^0C$ and $150^0C$. Mixtures less susceptible to contamination can be presently produced between $-30^0C$ and about $90^0C$ [60].

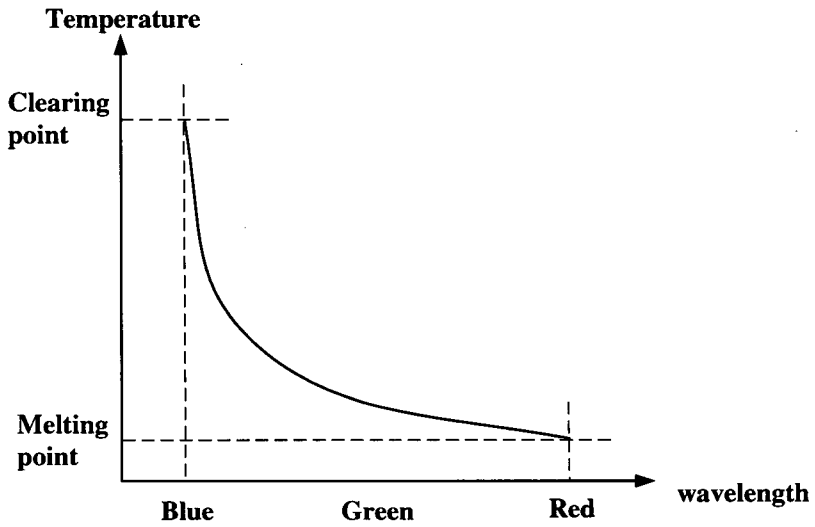


Figure 3.2: Colour/temperature response of a thermochromic liquid crystal.

While the melting point, or the clearing point, and the temperature band will define the optically active range of the thermochromic liquid crystal, the exact colour/temperature relationship, shown in Fig. 3.2 for an arbitrary liquid crystal under specified lighting conditions, has to be carefully determined by suitable calibration. This is a mandatory procedure when the thermochromic liquid crystal is used for quantitative mapping of various thermal regions.

Thermochromic liquid crystals have already demonstrated their unique characteristics in heat transfer research as accurate temperature measuring devices. There are numerous qualities that make these liquid crystals a very attractive alternative to more conventional temperature indicators. Their time response to minute changes in temperature is almost instantaneous due to their small mass, and precise mass production is achieved by formulating the liquid crystals in large batches to ensure variations of less than $\pm 0.1^0 C$ within the batch. Microencapsulation and chemical coating are two methods used to protect the liquid crystals against contamination and make them extremely durable and easy to handle. Thermochromic liquid crystal inks are mainly used in gaseous media while microencapsulated slurries can be used for flow studies in water. The main advantage of using thermochromic liquid crystals is the capability of mapping out large thermal regions with high resolution,

a task otherwise difficult to achieve without expensive more conventional thermographic instrumentation.

The following procedure describes the general use of thermochromic liquid crystals to obtain the temperature distribution on a arbitrary surface of interest:

1. The region of interest on the surface is chemically degreased to obtain a solvent free area;

2. A thin layer of specially formulated black paint is then applied onto the cleaned surface to act as a base and absorbing background, and is allowed to dry;

3. The specified liquid crystal is then applied in a thin layer on top of the dried black paint by one of the many available methods including screen printing, painting, spraying, and is allowed to dry;

4. If the liquid crystal instrumented surface is to be used over long periods of time and possibly exposed to various contaminating agents, further protection of the liquid crystal can be achieved by chemically coating the region of interest with a specially formulated varnish;

5. Appropriate illumination has to be arranged, and the viewing angle of the instrumented surface set;

6. The liquid crystal colour response with temperature has to be accurately determined through proper calibration under the given lighting conditions and viewing angle;

7. Once the calibration function is known, the temperature at any point on the instrumented surface is given by the viewed colour at that point.

This procedure can be used in a transient heat transfer experiment to monitor the surface temperature variation with time. Once the time history of the surface temperature is known, the method described in the previous section of this study can produce the desired detailed distribution of the surface film heat transfer coefficient $h_f$ and the film cooling effectiveness

$\eta$. The next logical step in the development of the method is to identify appropriate means of recording and storing the colour change of the liquid crystal instrumented surface, and to find a suitable colour-temperature conversion for the particular thermochromic liquid crystal used.

## 3.2 Imaging System

The use of thermochromic liquid crystals as temperature measuring devices depends on their capability to reflect different colours at different temperatures under certain lighting conditions. An accurate temperature measurement can only be achieved if the colour change of the liquid crystal is properly recorded, stored and further analysed. This requires the implementation of a colour imaging system to be used in conjunction with the aerodynamic arrangements and heat transfer hardware specific to film cooling research.

The imaging system requirements would then be high resolution colour capturing at rates sufficiently high for the transients used in the heat transfer experiment, transmission and recording of the colour signal with minimum distortion and in a form suitable for further computer processing, image display, enhancement and analysis capabilities. An automated image acquisition - data processing system has to use appropriate computing power and a dedicated computer is a fundamental part of such a system.

### 3.2.1 Illumination Sources

It is important to recognize that the thermochromic liquid crystal only produces colour by selectively reflecting the incident available light. The amount and quality of the ambient light will therefore dictate the quality and intensity of the colours produced.

Visible light is a form of radiant energy that propagates, by some theories, in the form of electromagnetic waves which cover a small region of the electromagnetic spectrum, having wavelengths $\lambda$ between approximately 380 nm to 780 nm. Figure 3.3 shows in more detail the spectrum of electromagnetic radiation.

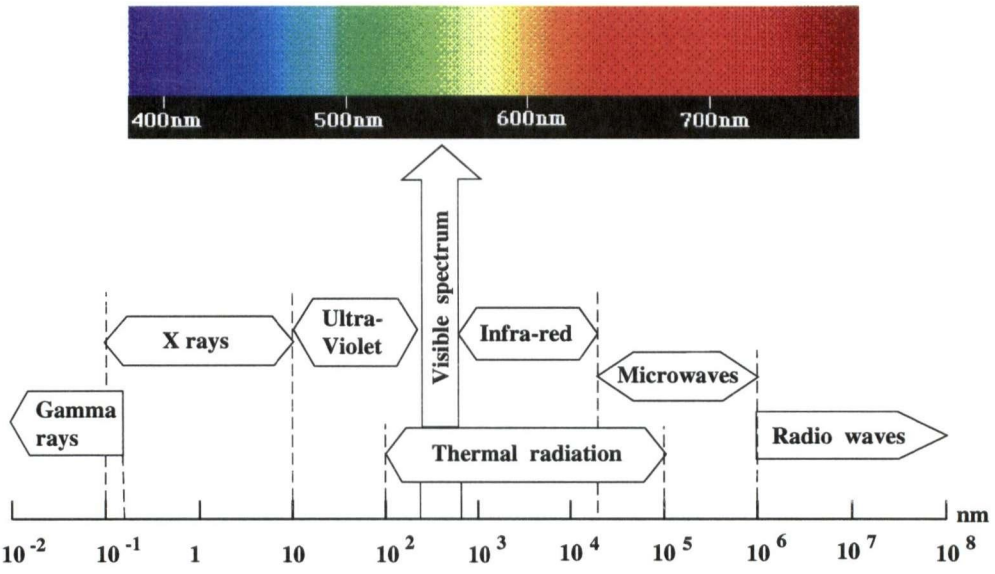


Figure 3.3: Spectrum of electromagnetic radiation.

In this context, colour represents the perceptual result of light on a human receiver, and the various devices of viewing colour are patterned on human vision. Since human vision is a very complex process involving physical, physiological and neurological aspects, colour perception is relative and thus basic tools are required for interpreting and quantifying the phenomenon. The science of colorimetry is concerned with the nature of human vision and provides a basis for specifying colour. Also, the Commission Internationale de L'Éclairage (CIE) [57] is the governing body that sets standards for all the aspects of colour. Only those elements important for this work will be exposed here.

Different objects appear to be of certain colour by selective reflection and absorption of the incident light. The light could have a natural source, the sun, or could come from an artificial source. An object would appear green if it absorbs the incident light at higher (red respectively) and shorter (blue respectively) wavelengths and reflects predominantly the light at wavelengths corresponding to green. Similarly, an object appears black if it absorbs most of the incident visible radiation and white if it reflects this radiation.

When characterising different artificial light sources, comparison with a standard white

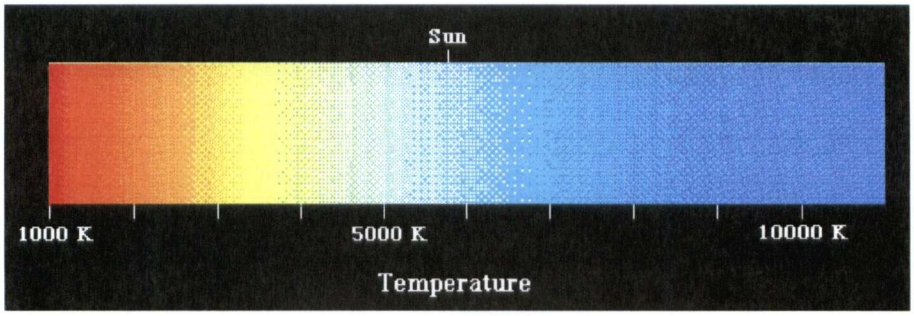


Figure 3.4: Blackbody radiation.

light is often used. The energy of the standard white light is well balanced across the visible spectrum. The spectral distribution of the white light is set by standard. Here, spectral distribution refers to wavelength dependent variations. A parameter called *Colour Rendering Index* (CRI) describes the ability of a given illuminant to render the colour appearance of an object in comparison with the colour of the same object when illuminated by standard natural light. A CRI of 100 was assigned for natural daylight. The *correlated colour temperature* (in units of degrees Kelvin) is another parameter widely used to describe a certain illuminant, and is associated with the blackbody concept used in radiation analysis. A blackbody is an ideal surface that absorbs all incident radiation (more generally from the thermal region of the radiant energy spectrum which includes the visible spectrum), and will emit radiant energy that is function of wavelength when heated. Many sources of illumination have at their core a heated object, and this is the reason why a light source is also characterised by the temperature (in degrees Kelvin) of a blackbody that provides the closest visual color match to the particular light source.

The colour temperature concept is better visualised in Fig. 3.4. The sun can be viewed as a blackbody radiator at temperatures between 5000 K to 7500 K. A low correlated colour temperature is correspondingly assigned for illuminants with most of the visible spectrum at comparatively longer wavelengths (towards red hues), and the colour temperature increases as more radiation appears at shorter wavelengths. For example, a correlated colour temperature of 3200 K is used for precalibration of consumer type video cameras as well as broadcast type cameras. Higher performance and higher cost video cameras would compen-

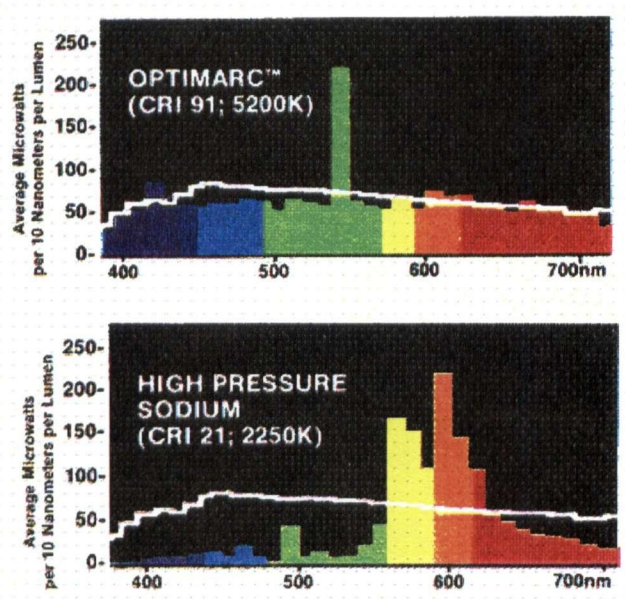


Figure 3.5: Optimarc lamp technical specifications.

sate for changing illumination conditions when shooting outdoors or indoors.

In this study, a white light system is used for best visualisation of thermochromic liquid crystal instrumented surfaces. The white light system consists of two 400 W Duro-Test Optimarc high-intensity discharge lamps with each lamp powered through a dedicated enclosed ballast unit. The technical specifications for the Optimarc lamp are a CRI of 91 and a lumen-per-watt efficiency of 28,000 lumens at 400 watts.

The Optimarc lamp was chosen due to its high colour rendering performance. With a correlated colour temperature of 5200 K and a spectral distribution matching closely the standard white light it proved to be the best choice for the application. Figure 3.5 (taken from Duro-Test Optimarc technical specifications [58]) illustrates the light spectral distribution of the Optimarc lamp as compared to the light spectral distribution of a fluorescent type lamp (high pressure sodium). Natural daylight spectral distribution is also shown with a white line in both graphs. The Optimarc lamp is clearly superior to the high pressure sodium lamp especially at shorter wavelengths, and this will benefit the colour rendering in the blue region

which corresponds with higher temperatures on a liquid crystal instrumented surface. This will allow for the use of a wide temperature-band liquid crystal, a rather novel approach in liquid crystal thermography.

### 3.2.2 Image Acquisition

Colour images can be viewed using many types of light sensing devices. The most suitable device has to be easily integrated into the imaging system while providing high resolution colour rendition. Various sensing devices have been tested and will be briefly described along with their possible use as primary sources in the present imaging system.

#### 3.2.2.1 Colour Photography

The first technique investigated was colour photography with images captured on 35 mm film. A Contax camera was fitted with appropriate lenses and used to photograph the colour change of a specially designed liquid crystal instrumented calibration surface. A reference coloured strip was always placed in the field of view. This allowed for the use of a common colour datum among the captured frames. The temperature of the calibration surface was monitored with two type K thermocouples. No colour correction was made during developing of the films.

The colour photographs were then digitized using a Hewlett Packard ScanJet IIC scanner and the generated 24-bit TARGA format graphics files were stored in an IBM compatible PC. A region of interest of 60x40 pixel between the two thermocouples was consistently sampled from every file and statistically investigated to determine the colour component means and standard deviations. The intensity for each of the colour components can take $256 = 2^8$ integer values between 0 (corresponding to black, all channels) and 255, typical of 8-bit/component digitization. The colour at each pixel location is completely specified by its red, green and blue intensity values. The scatter around the corresponding mean values is represented by the calculated standard deviations. The standard deviation is used as a measure of accuracy of the recorded colour information. The smaller the standard deviations

are, the higher the accuracy of the colour measurement is.

It was found that the uncertainty in colour measurement varies with temperature. For later comparison with other image acquisition techniques though, only the best statistics resulted from the investigated colour photographs are reported in Fig. 3.6. The same analysis can be done for any other colour representation, as discussed in following sections of this study (hue is defined in section 3.3 and Appendix A). For future reference, the mean hue values and standard deviations are also reported in Fig. 3.6.

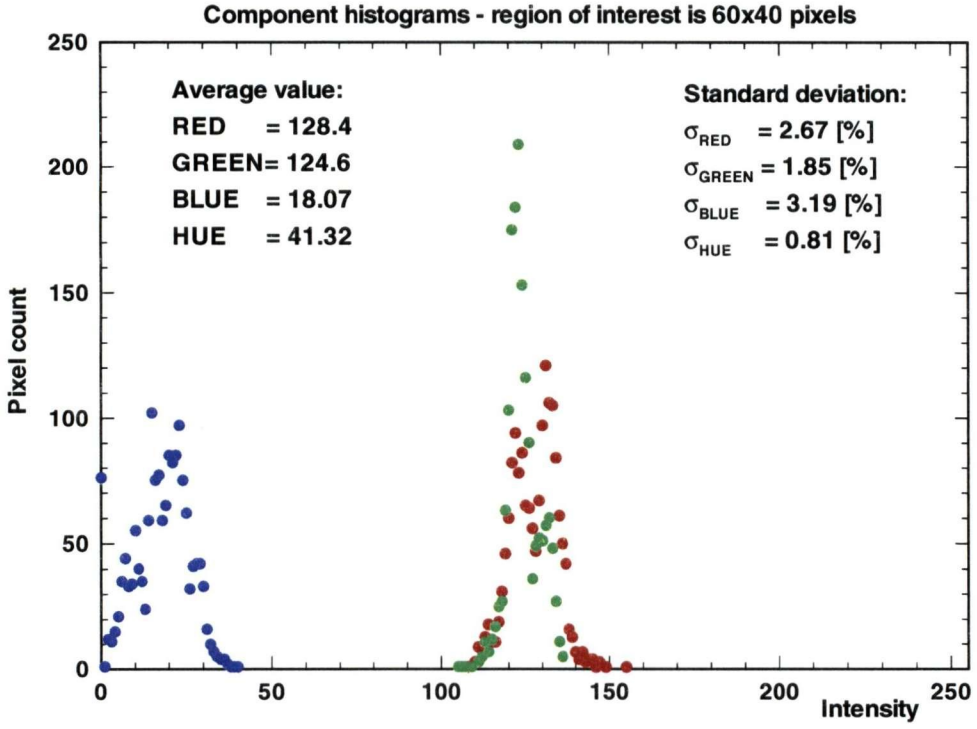


Figure 3.6: Typical histograms and statistics for colour photography.

Colour photography was found to produce good resolution images in the carefully monitored environment. The main drawback of the techniques lies with its output format, the colour photographs, that are not in a form directly suitable for mass storage into a personal computer. The colour photographs have to be individually digitized and this can be a prohibitively time consuming process when a large amount of data needs to be analysed. Implementation of this technique in the imaging system would not allow for the required

flexibility and fast output of the processed results. Other methods needed to be investigated and their performance assessed.

#### 3.2.2.2 Video Capturing

As an alternative to colour photography, video capturing offers the benefits of increased frame rate and more versatility on the video output format. High resolution and high image quality are also possible with the appropriate choice of the video camera. Real-time video digitization can also be done through dedicated electronics so that information can be quickly stored into a host PC for further processing and manipulation.

The main video signal standards in use are NTSC (National Television Standards Committee, used in North America, Japan, Korea, some Latin American countries), PAL (Phase Alternation by Line, used in most of the Western European countries, Australia, China, Africa), and SECAM (Sequentiel Couleur Avec Mémoire, used in France and some other French speaking countries and in most countries from the former communist block). Although NTSC has a reputation for poor colour accuracy, this is only true for broadcast television. As a video format, the NTSC format achieves better signal to noise performance than either PAL or SECAM formats. This further justifies the use of a video camera working in NTSC video format.

Either an analog or a digital video camera could be used in the imaging system. The choice was made considering the colour image quality and the associated costs. At the time this work was conducted, a lower performance digital video camera was almost as expensive as a high performance analog video camera. It was then decided to further investigate the use of analog video cameras to capture the colour change of a liquid crystal instrumented surface.

Previous research using thermochromic liquid crystals relied almost exclusively on CCD video cameras for colour capturing, due to their compactness and ease of use. Some fundametal aspects of the way these cameras create colour have to be understood so that their performance in the overall imaging system can be properly evaluated. CCD stands for

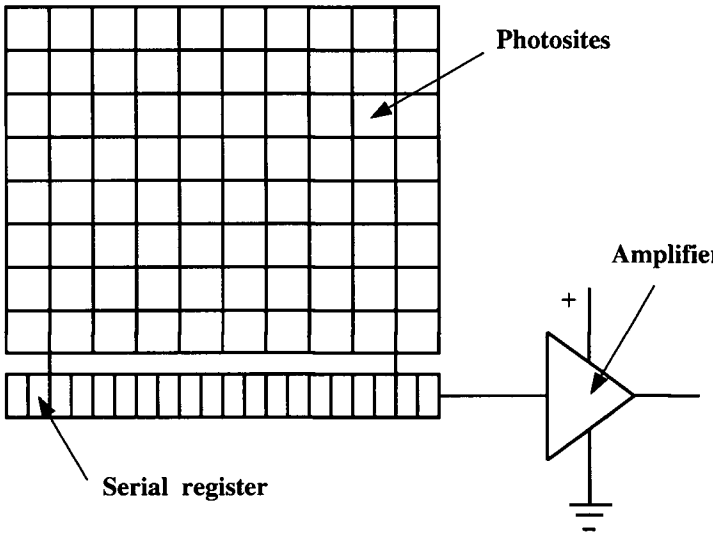


Figure 3.7: Charge-coupled device - CCD.

charge-coupled device and is actually an array of hundreds of thousands of light-sensitive photosites (or pixels) formed on a silicon chip. When light reflected from an object in the field of view falls on the CCD, the various photosites will be charged differently according to the amount of light they see. Charge-coupling (cycling the applied voltage) is the technique used to transfer the freed electrons from the various photosites line by line into a serial register, and off to an amplifier at the end of the serial register. A schematic of a CCD is shown in Fig. 3.7.

The number of pixels, or light-sensing elements, from a CCD should not be confused with the number of pixels, or the resolution, of the output image. There is no direct relationship between the number of pixels on a CCD and the number of pixels in the viewed image, typically there are significantly more pixels on the CCD than in the final image. The quality and uniformity of the CCD array of pixels , together with the accompanying electronics would make the difference between the consumer type and the professional type of video cameras.

The most important technical specifications that directly affect the image quality from a video camera are the S/N ratio (Signal-to-Noise ratio) and the horizontal resolution. The S/N ratio expresses the amount of useful video information as compared to the amount

of noise within a certain video image. The term noise normally characterises the random variation in a measured or observed quantity. The higher the S/N ratio is, the better the image quality is. A S/N ratio of at least 42 db to 45 db is generally required for a consumer type video camera.

The vertical resolution in a video image is basically set by the NTSC format at 525 horizontal lines. A measure of the actual resolution in an image is then expressed by the lines of horizontal resolution, which represent the vertical lines per picture height one would count across a horizontal line on a video image. This is the appropriate way of representing the resolution of the luminance component, while the colour resolution is always less due to the nature of the human eye response (more sensitive to the black/white signal than to the colour signal in an image). For example, the VHS (Video Home System) videotape format is characterised by approximately 240 lines of horizontal resolution, and the S-VHS (Super-Video Home System) format can achieve around 400 lines of horizontal resolution, both referring to the luminance (black/white) component.

Colour is reproduced in a video camera through an additive process by mixing three primary colours namely red, green and blue. Processing the individual colour channel output is done by matrix circuits to yield three types of signals, a luminance signal and two chrominance signals. The luminance signal, often referred to as the Y channel, is skimmed from all three colour channels, and contains a black and white representation of the viewed object. The two chrominance channels (or C for chrominance, or chroma) contain all the colour information. Furthermore, the luminance (Y) and chroma (C) channels could be encoded together in what is referred to as a composite video signal, or could travel on separate wires thus producing what is referred to as the Y/C video signal, characterised by higher quality video. The latter method is at the heart of the S-VHS format, providing increased resolution and less inherent noise. Individual red, green and blue components can also be used in what is referred to as a component (or RGB) video signal. This produces the best quality of the colour images since no encoding/decoding circuitry is needed.

Extensive tests were conducted using a single chip Panasonic PV-S770-K OmniMovie S-VHS camcorder. Single CCD cameras produce colour with the aid of a filter system placed in front of the CCD and the signal is electronically separated into the three primaries red, green and blue. When the S-VHS format is employed, single chip colour cameras can produce good quality images at a relatively low cost, and this was the motivation for testing such a camera. The technical specifications of this camera indicate a S/N ratio of 44 db, luminance resolution of 400 lines and colour resolution of 80 lines. The output video signal was recorded on tape using a S-VHS video cassette recorder (VCR), and also directly into a PC through a time base corrector/digitizer board. More will be said about time base correctors (TBC) and digitizers in the following sections of this study. It was found from these tests that the colour rendition of the video camera/storing device chain was not yet satisfactory for quantitative interpretation of the thermochromic liquid crystal response with temperature. Figure 3.9 on page 88 shows the best statistics of a region 60x40 pixels out off a test video sequence captured with the S-VHS camera and recorded by a S-VHS VCR on S-VHS tape. Figure 3.10 on page 90 shows the best statistics of a region 60x40 pixels out off the video frames captured with the S-VHS colour camera and stored directly into the computer. These sample statistics will be used later for comparison of all image acquisition techniques investigated in this study.

The final image source device selected for the application was a 3-CCD JVC KY-F55B colour video camera that provides a S/N ratio of 60 db, with a luminance resolution of 750 lines and colour resolution of 580 lines for the output RGB video signal. The superior performance of this camera is mainly due to the three chip concept, high performance 380,000 pixel CCDs, and improved circuitry and optics. The incoming light received by the video camera lens is split by a colour separation optical prism system into the primary red, green and blue colour components that are individually focused on a corresponding CCD. Such an arrangement is illustrated in Fig. 3.8.

The advantage of having three dedicated CCDs, one for each of the colour primaries, is

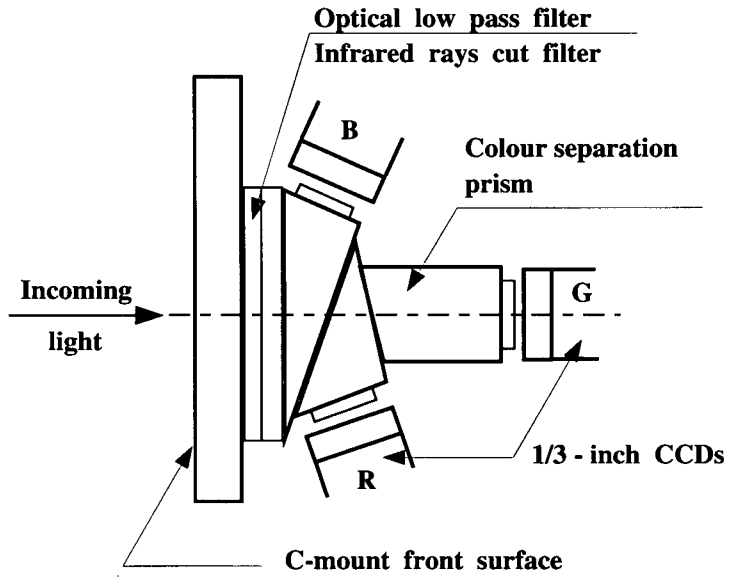


Figure 3.8: Colour separation optical system.

fully appreciated when using the red, green, and blue generated signals which have not gone through a matrix stage. Maximum resolution and image quality can only be achieved if the output RGB video signal is recorded in the same format, and its characteristics preserved. Using a high performance 3xCCD camera and then recording the signal onto a consumer type VCR, incapable of accurate storage and reproduction, would defeat the purpose of generating a high quality signal at the source-end of the imaging system chain. The method used to record the colour video signal deserves further attention, and it represents the second component of the integrated imaging system.

### 3.2.3 Recording and Storage Devices

Video capturing with CCD camcorders (consumer type video cameras) and recording onto a video tape using consumer type VCRs, was the method almost exclusively used in previous studies involving liquid crystal thermography. The motivation for using such a system lies with the relatively low cost of the equipment, wide availability, ease of use, and simple integration. Since the data has to be finally processed with the use of a PC, storing the images directly into the PC memory or hard disk is also a very attractive option. These

possibilities were investigated during the development and integration of the imaging system finally used in this study.

#### 3.2.3.1 Video Tape Recorders - Video Tapes

Video tapes and video tape recorders (VTR) represent the foundation of both professional and commercial video industry. VTR is the more general designation for any type of reel-to-reel recorder and includes the popular video cassette recorder or VCR. A generous amount of literature is dedicated to this topic and a good description of various components was found in [49].

Component VTRs record all three colour signals red, green and blue as generated by the video camera thus providing the best quality among the various video tape formats. This is also typically done in digital format, so that the original video information is much more durable in time and multiple copies can be produced with no loss of quality. The main drawback of using such machines is their high cost and limited availability.

If the component VTRs represent the higher quality of the video tape formats, the popular VHS format is at the opposite lower end of the available formats. The low cost and the direct availability of consumer VCRs using this format made them the immediate choice of most researchers involved in the past in liquid crystal thermography. Their main disadvantage is low signal quality and more specifically limited colour signal recording and reproduction capabilities. These machines were simply not designed for accurate colour reproduction as needed in typical thermochromic liquid crystal visualisation or other colour measurement applications. The images reproduced by a good quality VHS machine have to be only as good as a standard human observer would critically tolerate. The high frequency input colour information is down-converted by a factor between 5 and 6 before being recorded on tape, and is up-converted by the same factor when the tape is played back. The information that is lost during the down-conversion process cannot be recovered, and this is one of the reasons why the colour resolution is much less than the luminance resolution for this video tape format. Other image quality limitations are directly related to the composite video signal

(luminance and chroma channels matrixed together) used as input to the VHS recorder. Separating the chroma information from the luminance information before recording on tape, and recombining the chroma and luminance signals at play back is another source of image degradation associated with the VHS format.

The S-VHS format is able to achieve higher luminance resolution by keeping the chroma signal separated from the luminance signal (Y/C signal). The colour signal though goes through the same down-conversion and up-conversion procedures on recording and play back respectively. Although the images look much sharper in S-VHS format, the colour information in not much better than in the VHS format. Initial tests were conducted with the S-VHS Panasonic video camera, and a Panasonic AG-1970 ProLine S-VHS VCR was used to record the colour change of a instrumented liquid crystal surface on S-VHS tape. The recorded images were then played back on the S-VHS VCR and transferred to the dedicated PC through a Digital Processing Systems PAR-TBC IV digitizer. For comparison with other investigated image acquisition techniques, the best statistics of the colour investigation on a region 60x40 pixels are reproduced in Fig. 3.9 .

The uncertainty in colour measurement using S-VHS video tape recording is comparable with that using colour photography, as expressed by the standard deviation values in Fig. 3.9 and Fig. 3.6 on page 80 respectively. Higher accuracy is possible and this will be addressed further in this study.

Storing the colour change history on video tapes was the method most widely used in liquid crystal thermography in the past. The advantages are low cost, good frame rate, ease of use and direct hardware availability. The main drawbacks are associated with the colour resolution itself, too low for quantitative colour analysis purposes, and the unstable VCR output signal. The latter is due to the mechanical complexity of VCRs that makes them unable to play back a tape at exactly the same speed the tape was recorded. This is referred to as the time base error, measured in video lines, and is a known problem in video production since VCRs cannot be integrated with other stable sources through a switcher. Time base correction is needed to obtain a stable video signal and this is done with a *time*

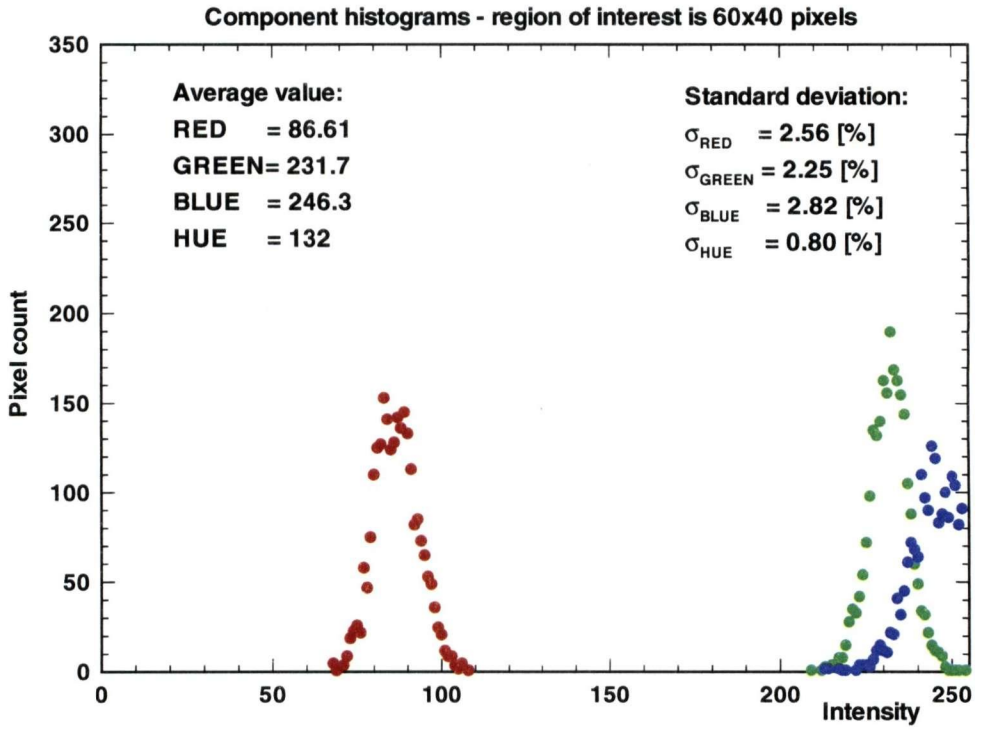


Figure 3.9: Typical histograms and statistics for S-VHS tape recorded images.

*base corrector* (TBC). The unstable VCR output video signal is fed into the TBC, and the stable video signal coming out of the TBC can now be used for integration with other devices. This comes with a high cost since a high performance TBC is an expensive piece of equipment.

Since it appeared that at least a S-VHS machine, good editing and time base correction capabilities are needed for preliminary liquid crystal thermographic tests, other options were investigated within the same budget range. A more direct way of transfering the colour information into the computer while achieving good colour resolution would provide a more efficient imaging system, absolute requirement for colour measurement applications.

#### 3.2.3.2 Digitizers - Hard Drives

With the increased performance of today's computer bus system and peripherals, bringing live video into the PC environment at affordable costs is only a matter of time. The main

problem the manufacturers have to overcome is the bandwidth, or the amount of information that can be transferred per unit of time as required by video applications. As already pointed out, the best colour resolution is achieved when providing three separate channels for additive primaries red, green and blue. Colour systems that provide 8-bit digitization for each of the three components are referred to as *true colour* systems or 24-bit systems. A typical NTSC frame would require for true colour reproduction 900 KB (Kilo Bytes, 640x480x24=7,372,800 bits), and real-time video at 30 fps (frames per second) would consequently require approximately 26 MB (Mega Bytes) to be transferred in one second. For comparison, the amount of data generated by digital audio in the very popular CD format is about 150 times smaller (approximately 185 KB per second).

Numerous compression methods (or *codecs* for compression/decompression algorithms) have been developed and research continues into video image compression, a method widely used to incorporate video in PC environment. Physiological limitations of the human eye prove handy and are fully exploited in designing new algorithms of data compression. Basically, all audiovisual compression methods need to be patterned on human perception, thus removing the less relevant information to such an extent that the quality loss is not noticeable to a human observer. The compression methods can be generally split into two major types, lossless and lossy compression, whether information is lost or not. In lossless compression, as the name suggests, only the redundant information is combined and condensed and no loss of quality occurs. The compression factors that can be achieved this way are relatively modest and lie between 1.5:1 to 3:1. In lossy compression, information that is considered not important for visual perception is actually removed from the video signal, and much higher compression factors can be achieved.

Analog video information cannot be stored as such into a digital computer. The analog signal has to be digitized first, which means that its shape is discretely sampled and consequently processed as numbers by the computer. The piece of hardware that represents the link between the analog signal and the digital computer is referred to as the digitizer, or frame grabber, or capture board. Digitizers can perform much more complicated functions

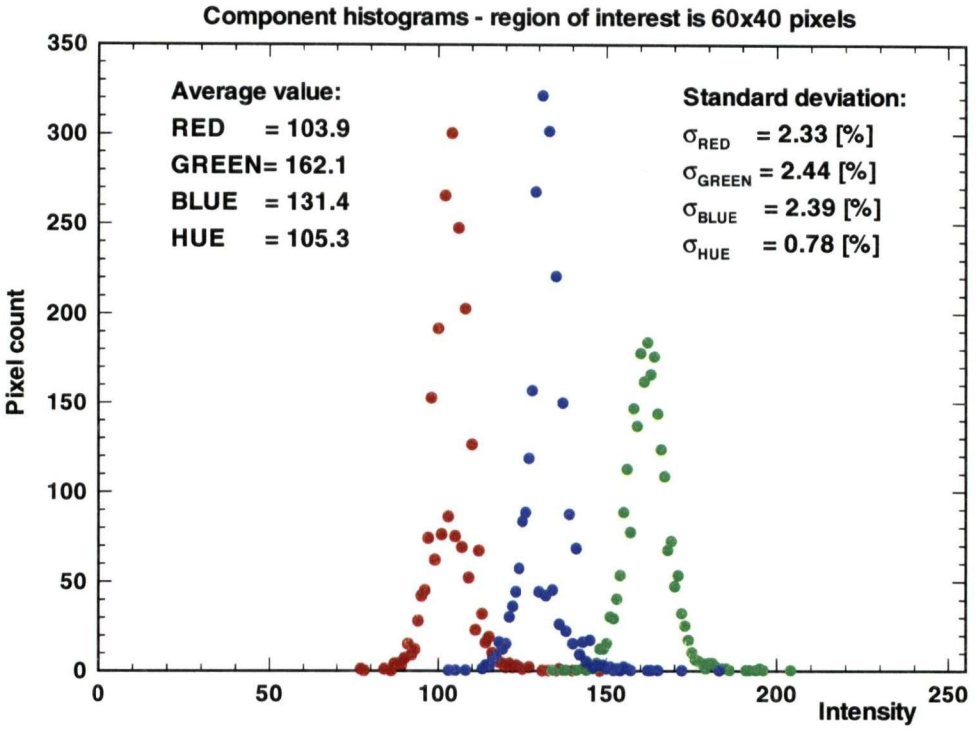


Figure 3.10: Typical histograms and statistics for S-VHS PAR-disk recorded images.

and can be specifically programmable as well.

Tests were conducted with a real-time video capture deck with image storage directly in the PC on dedicated disk drives. The system used was the Personal Animation Recorder (PAR) and the time base corrector TBC IV, both from Digital Processing Systems Inc. The Y/C video signal from the Panasonic S-VHS camera was fed directly into the PAR-TBC IV system which allows for real-time digitization and storage of the video sequence as animation files. Individual video frames were recovered as 24-bit TARGA files, and the same colour investigation process was conducted on a region 60x40 pixels located between two type K thermocouples on the liquid crystal instrumented surface. For comparison with the other image acquisition techniques investigated in this study, the best statistics from all recorded test sequences are shown in Fig. 3.10.

It can be seen that the scatter around the mean component values, represented by the corresponding standard deviations, is not much different from the best results obtained with

colour photography or S-VHS video tape recording shown in Fig. 3.6 on page 80 and Fig. 3.9 on page 88 respectively. This can be explained by investigating the PAR-TBC IV system performance on real-time video data transfer. In order to manage the large amount of information, the system uses a lossy compression algorithm. In the best case, a compression factor of at least 5:1 is achieved at the expense of high-frequency colour information. This is of course, not much better than the colour down-conversion process used in video tape recording. The reconstructed images look acceptable when viewed by the human eye, but the lost information can be quantified in the colour measurement process.

A system able to transfer in real-time all the required uncompressed RGB video data would represent an improvement of the status quo as far as colour measurement based liquid crystal thermography is concerned. This can be done with digitizers taking full advantage of improved sustained PCI bus transfer rates. PCI stands for Peripheral Component Interconnect and represents the shared line of communication between the host CPU, memory, display boards, frame grabbers, and other peripherals, the heart of traditional PC architecture. A 32-bit wide PCI bus running at 33 MHz can theoretically transfer up to 132 MB/s.

The frame grabber finally chosen for the application is a Matrox Meteor/RGB colour digitizer with transfer rate capabilities of up to 35 MB/s in NTSC format. This means that a 32-bit colour input data in the form RGBx (x represents an extra channel) at a resolution of 640x480 pixel and a frame rate of 30 fps can be transferred in real-time to either the host computer memory or display. The display is achieved real-time using a Matrox Millenium MGA display board with 4 MB on-board memory. The host PC is carefully specified to perform the sustained PCI transfer rates to system memory. After the video sequence is transferred and stored into the host RAM it can be then saved on a hard disk at slower transfer speeds. Direct transfer and storage onto fast dedicated hard drives would have been possible at higher cost.

### 3.2.4 Imaging System Specifications

A new imaging system was developed and implemented for use in liquid crystal based thermographic applications. The imaging system is based on real-time true colour video capturing and recording on computer RAM with sequential storage onto a hard drive. The system is characterised by excellent colour rendering, high colour resolution, high quality colour signal, minimum required hardware, and direct data availability in digital format for processing and measurement.

The lighting is produced by a white light system for best colour rendering, the colour capturing is done by a 3xCCD RGB video camera, the RGB video signal is transferred uncompressed in real-time into the host PC RAM through a 32-bit colour frame grabber, visualisation is done real-time on computer monitor through a dedicated 4 MB WRAM display board. The host PC is an Intel Pentium 200 MHz processor based Windows NT machine with 256 MB of RAM. A schematic of the imaging system is shown in Fig. 3.11.

The imaging software used to control the video sequence capturing, file conversion, image processing and analysis is Matrox Inspector-32 version 2.1. Scripting is probably the most important feature of the Inspector. Scripting allows the developer to customize a particular application by writing specific programs to automate complicated repetitive tasks. The programming language used within the Inspector has close similarities with the more popular C language. Inspector also supports multiple file formats including TARGA, TIFF, JPEG and more. An additional software package, Matrox Intellicam, can be used as an interactive utility for interfacing various types of cameras. A specific digitizer configuration format (DCF) file is required for each attached video source.

A memory buffer has to be allocated for real-time data transfer upon installation of the imaging software, and can be further modified by calls to the Meteor driver. This procedure proved unreliable and conflicted with the good operation of the overall system. This again shows the importance, sensitivity and complex interaction of every piece of hardware involved. Perfect integration among the various devices is required to achieve the desired performance of the imaging system. The memory buffer allocation allows for capturing of

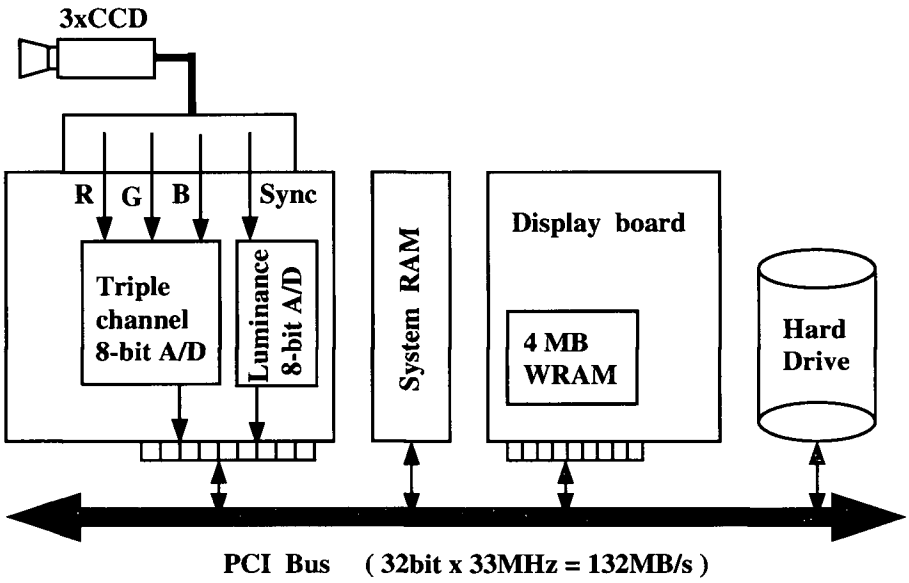


Figure 3.11: Block diagram of the imaging system.

a maximum 92 frames real-time. Direct transfer to a dedicated partition on the host hard drive can be done at 3 fps only but for a longer period of time. Creating a memory partition to act as a RAM disk is another option and transfers of up to 10 fps can be achieved in this way.

This newly developed imaging system can be used to accurately analyse the colour change history of a liquid crystal instrumented surface. The colour information is only useful in a three-temperature experiment if converted into temperature information. The exact relationship between the observed colour and the temperature of the surface must be identified.

## 3.3 Tristimulus Colour Space

There are three types of light receptors in the human eye responsible for daylight vision, the cone cells, while a fourth type of receptor, the rod cells, plays a more important role only at very low light levels, or night vision. The three colour cone receptor cells each have a different spectral response to the incident radiation that peak in the red, green, and blue regions of the visible spectrum respectively. Since there are three types of colour photoreceptor cells,

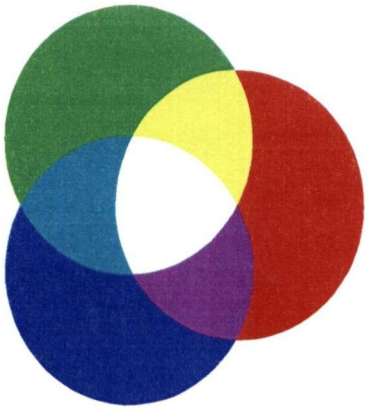

Figure 3.12: Additive system with Red, Green, and Blue primaries.

three numerical components are necessary and sufficient to specify any colour, and this is the basis of the trichromatic theory of colour vision. The three components are referred to as primaries, or colour stimuli, and represent the coordinates of a tristimulus colour space. The requirement for the primaries is that no single one of them can be produced by a combination of the other two.

In a tristimulus colour space, any colour can be produced by an additive mixture of accordingly weighted primaries. Several colour coordinate systems have been standardised by CIE to accomodate the needs for colour specification of different practical applications. Colour space conversions are merely linear transformations and are directly available in CIE specifications. The implementation of such linear transformations are also beneficial from a computational point of view, being fast to compute.

The largest colour range (gamut) is obtained in additive reproduction using red, green, and blue as primaries. This is at the basis of the CIE's colour matching tests that produced the RGB colour space corresponding to monochromatic primaries red (with $\lambda = 700$ nm), green (with $\lambda = 546.1$ nm), and blue (with $\lambda = 435.8$ nm). Equal amounts of red, green, and blue produce white (all colours) at a specified luminance level as shown in Fig. 3.12.

A combination of red and green produces yellow, green plus blue produces cyan, and blue plus red produces magenta. Yellow, cyan, and magenta represent complementary colours to blue, red, and green respectively. Black would represent the lack of any colour. A direct

application of the RGB colour space is used in television for colour display on cathod ray tube (CRT) monitors. The NTSC's RGB colour space is obtained through a linear transformation from the CIE's RGB colour space. A system that uses cyan, magenta, and yellow (CMY) as primaries is also widely used in colour printing.

Other colour spaces have been produced to better match the human visual perception of colour. There are three common attributes that describe the human response to light known as hue, saturation and brightness. The hue of the light is the attribute that distinguishes the colour itself, for example red, yellow or blue. When the light source is monochromatic (as the CIE's RGB primaries) the hue is an indication of the wavelength of the light. The saturation is a measure of the purity of a colour, or a measure of the amount of white light added to a pure colour. Pure colours are also referred to as spectral colours for which the corresponding spectral power distribution is concentrated at one wavelength. Brightness is a more subjective and complex attribute according to which an area appears to emit more or less light. For measurement purposes, the CIE defined another quantity for brightness called luminance and denoted Y. The magnitude of luminance is now proportional to physical power and its spectral composition is related to the luminous efficiency of a standard human observer. Yet another quantity is defined by CIE to account for the nonlinear human perceptual response to luminance, called lightness. Lightness can be referred to as the relative brightness since an area would appear to emit more or less light in proportion to a similarly illuminated area perceived as white. A fundamental reference for all aspects of colour was found in [55]. In common language brightness, luminance, intensity, and lightness all refer to a black and white version of the image, while hue and saturation contain the chrominance information of the image.

Several colour models have been developed to accomodate the visual perception of hue, saturation, and brightness. One such system is the HSL colour space, standing for hue, saturation, and lightness as shown in Fig. 3.13. Lightness is a term normally used in discussing light reflection and it is used somewhat loosely here.

In the double hexcone arrangement, the lightness is represented on the vertical axis

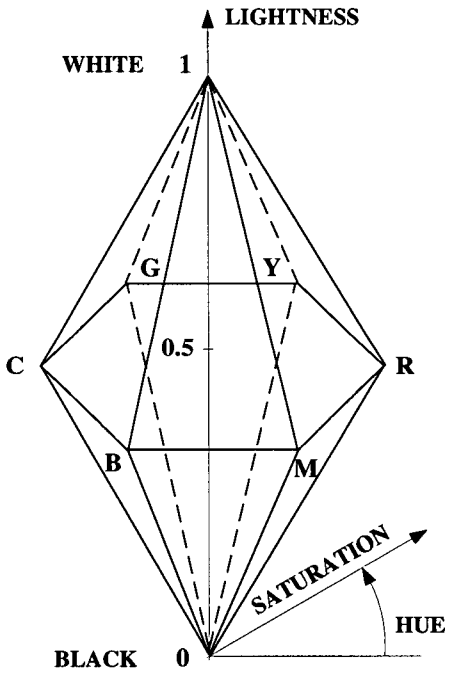


Figure 3.13: The double hexcone HSL colour space.

ranging from 0 for black, at the lower tip, to 1 for white at the upper tip of the double hexcone. Hue is represented by the angle around the vertical axis with red at $0^0$ and the other colours in the spectrum appear when the double hexcone is traversed counterclockwise. The saturation is simply measured radially from the vertical axis with 0 on the axis and 1 on the surface corresponding to fully saturated colours. For 8-bit digitization the corresponding range will be from 0 to 255 for each colour coordinate. The RGB to HSL colour space conversion algorithm is described in Appendix A. Both RGB to HSL and HSL to RGB colour space conversions are available with the Matrox Inspector-32 imaging software. More conversion algorithms can be found in [41].

For the present application, an appropriate relationship must be found between the temperature of a liquid crystal instrumented surface and either the RGB or HSL colour spaces. This function must be easy to compute and must minimize the error in temperature over the entire liquid crystal useful colour response. Only when the exact form of this relationship is known, for a given liquid crystal setup under known lighting conditions, can the thermochromic liquid crystal become a powerful tool for thermal mapping.

## 3.4 Calibration of the Liquid Crystal

This section presents the calibration of the thermochromic liquid crystal and video camera system used in the wind tunnel experiments described in section 4 of this study. The wide-band liquid crystal used in this study was custom manufactured by Thermax-Thermographic Measurements Inc. [60].

The same lighting conditions and video camera setup must be used for both calibration of the TLC and actual experiments. The incident light on the TLC instrumented surface must be uniform and such that the surface would appear without gloss. A pair of white light lamps was placed symmetrically above the liquid crystal instrumented surface as shown in Appendix B, and their relative position and distance to the surface was adjusted until the above conditions were satisfied. No measurements were taken until the lamps reached their normal operating temperature.

Light uniformity was checked by shooting a white piece of paper placed on the surface of interest within the field of view. The position of the lamps was adjusted until a uniform colour signal in the R, G, and B components was achieved across the white subject. The white balance of the video camera was adjusted for the actual lighting conditions, and the white paint data was stored in the video camera's memory. A master white still image was then captured and stored on the hard drive. This procedure ensured that the settings used for TLC calibration were restored for all runs based on that calibration.

Possible electromagnetic interference on the video signal from the noisy wind tunnel environment (wind tunnel motor, in-line heater, heater coil, and lamp ballast units as described in section 4.3), as well as possible induced CCD thermal noise, were quantified by shooting a sequence of dark images with the lens covered. After digitization, noisy pixels would apper to have R, G, B values different than 0, on a 0 to 255 range. The averaged results showed that on the R channel 99.994% of the pixels were clean, on the G channel 99.971% of the pixels were clean, and on the B channel 98.547% of the pixels were clean. The noisiest pixels had a value of 2, on a 0 to 255 range. The results were considered satisfactory and no further noise correction was made on any of the recorded images.

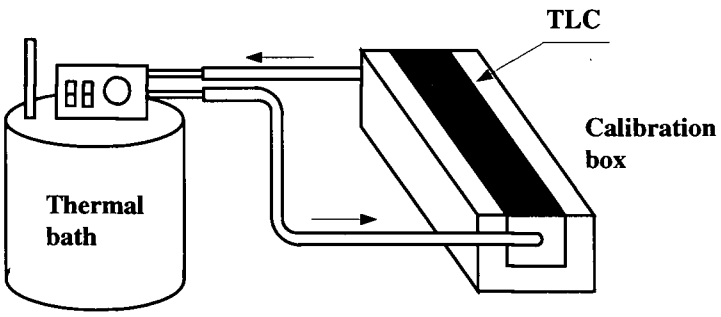


Figure 3.14: TLC calibration setup.

A geometrical calibration was also made by measuring the TLC instrumented patch in physical units. The resultant resolution was 3.23 pixel for each millimetre unit length.

The calibration of the Thermax wide-band TLC [60] was done in the same wind tunnel, and under the same lighting and viewing angle conditions as the actual experiments described in section 4 of this study. A specially designed hollow rectangular calibration box was used for this purpose. The rectangular box was made of aluminum and was insulated in a 2 inch thick layer of Styrofoam on all but one of its sides. The exposed side was machine polished and treated by the method described in section 3.1. A type K thermocouple connected to an OMEGA OMNI-CAL unit was mounted on the surface before the black paint and the TLC were sprayed using an air brush. To achieve the same TLC layer thickness on the calibration box and on the flat plate test surfaces, the two were simultaneously treated and sprayed.

The hollow calibration box was connected in a closed loop to a LAUDA-BRINKMAN K-4R refrigerated circulator using distilled water as the circulator agent, as shown in Fig. 3.14. The temperature of the bath can be set with a thermoregulator and the bath heat input rates can also be adjusted by a wattage proportioning electronic relay. A slow temperature increase of the circulator agent was achieved in this way, allowing for a uniform temperature on the TLC instrumented calibration surface. The temperature of the surface was known at all times, being digitally displayed by the OMNI-CAL unit. Still images were recorded directly on the dedicated imaging system PC's hard drive for each $0.2^0C$ temperature increase from $18^0C$ to $41^0C$. A region 60x40 pixels around the thermocouple leads was then sampled from each image and analysed. The wide-band TLC's colour response with temperature is

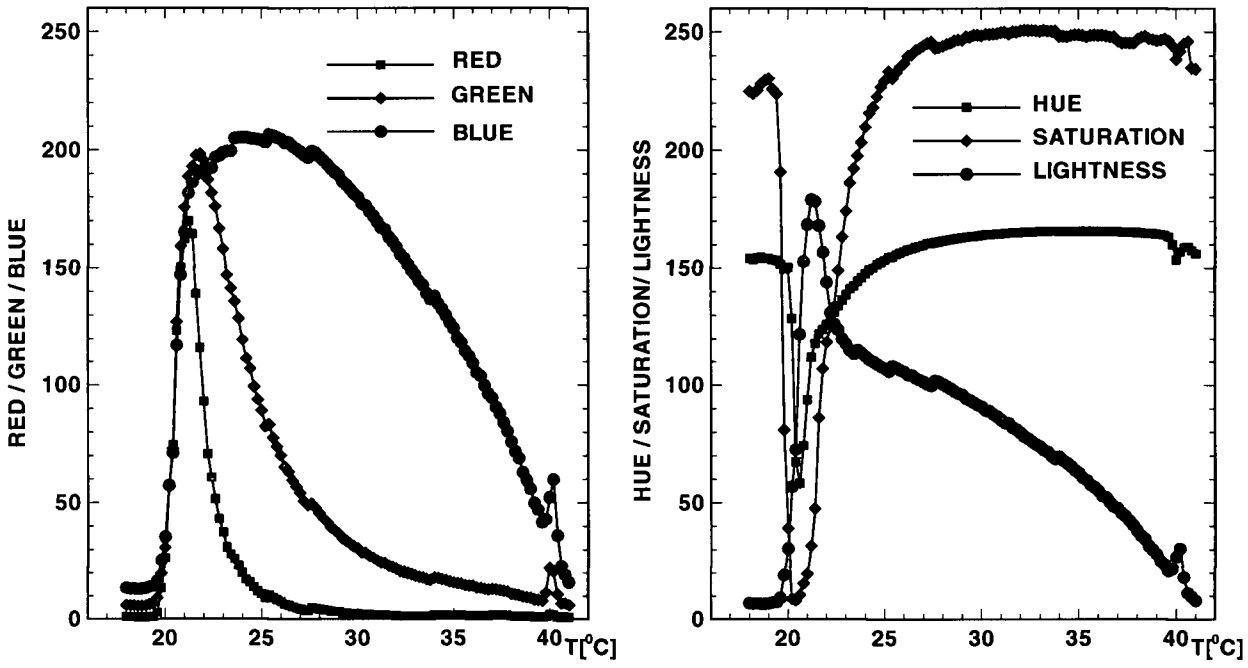


Figure 3.15: TLC colour response with temperature.

shown in Fig. 3.15, in both RGB and HSL colour spaces.

The melting point of the TLC was between $19^0C$ and $20^0C$, and the clearing point was around $41^0C$. No clear relationship between the colour displayed by the TLC and the corresponding temperature was identified using the RGB colour space. In the derived HSL colour space, more clear dependencies can be identified between the colour components and temperature. The lightness (L) component shows the same type of dependency with temperature as the R, G, and B signals. The lightness signal peaks at around $21^0C$ and has a monotonic behaviour below and above this temperature. A possible lightness versus temperature relationship is thus identified for the temperature range $T > 21^0C$. Both the hue (H) and the saturation (S) components have a minimum at around $20.6^0C$, and are monotonic with temperature above this value. Both H and S components appear to flatten out at temperature values around $30^0C$. A possible hue, or saturation, versus temperature relationship was therefore identified for the temperature range between $20.6^0C$ and $30^0C$.

The final choice for the use of hue or saturation was made after investigation of the absolute error in H, S, L, as a function of temperature, resulting from multiple calibration

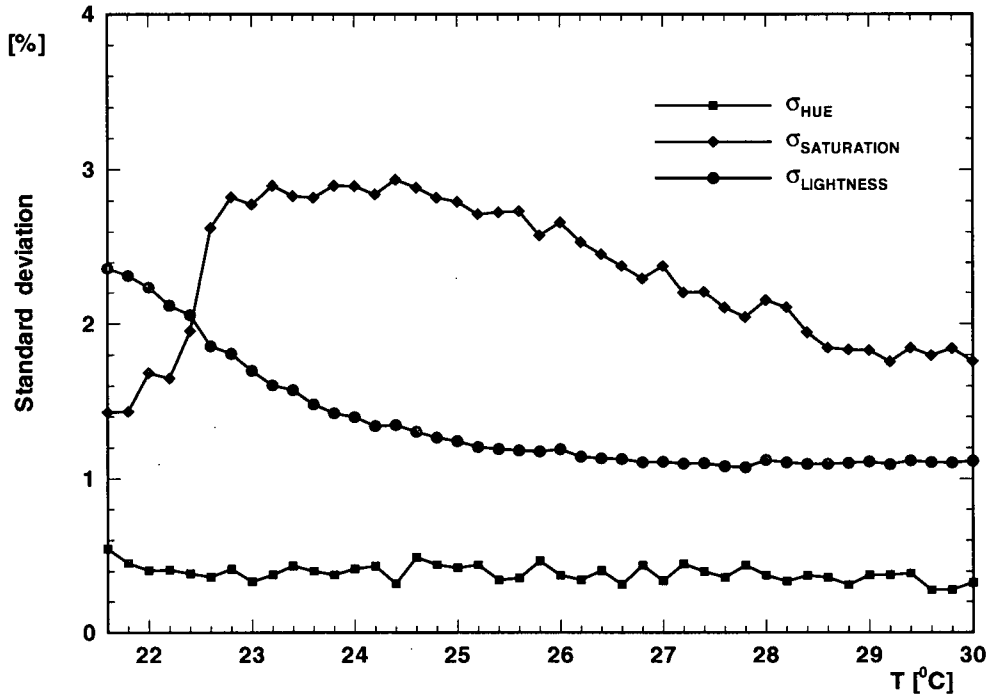


Figure 3.16: Statistics for real-time true colour recording.

data sets. The TLC calibration was repeated seven times, under the same lighting conditions, for a temperature range between $20^0C$ and $30^0C$ with a temperature increment of $0.2^0C$. Standard deviation values computed from the calibration data set for a region of 60x40 pixels are presented in Fig. 3.16. The uncertainty values corresponding to the hue component are about 50% less than those from colour photography, SVHS tape recording, and SVHS disk recording shown in Fig. 3.6 on page 80, Fig. 3.9 on page 88, and Fig. 3.10 on page 90 respectively.

The absolute error in any of the H, S, or L components was calculated, for any temperature, as the maximum variation about the mean value, according to Eqn. 3.1:

$$\epsilon_H = \frac{max[H(T)] - min[H(T)]}{mean[H(T)]} \times 100\% \tag{3.1}$$

The error values from multiple calibrations are plotted against temperature in Fig. 3.17. The minimum error was found to correspond to the H component, and a useful temperature

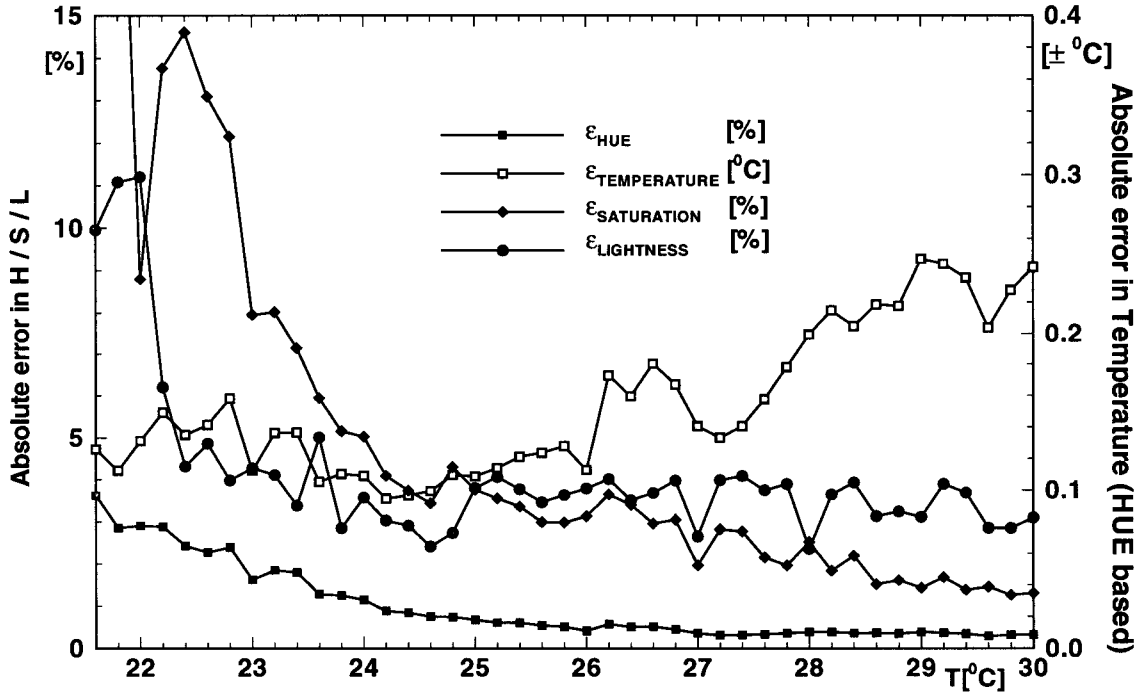


Figure 3.17: TLC calibration accuracy.

range was indentified between $21.6^0C$ and $30^0C$. The error in the H component was between 3.6% and 1% for temperatures between $21.6^0C$ and $24.1^0C$, dropped between 1% and 0.5% for temperatures between $24.1^0C$ and $26.6^0C$, and was below 0.5% for temperatures between $26.6^0C$ and $30^0C$. The hue component was consequently used to obtain the desired colour - temperature relationship.

An eighth order polynomial was used to compute the temperature of the TLC instrumented surface based on the calculated hue colour component. An absolute error in temperature could be then calculated based on the calculated absolute error in hue from multiple calibrations, and the result is also shown in Fig. 3.17 for the temperature range between $21.6^0C$ and $30^0C$. For this temperature interval, the error in temperature is as low as $\pm 0.1^0C$ and as high as $\pm 0.25^0C$.

The use of multiple calibration data sets produced the needed relationship between the colour displayed by the wide-band TLC instrumented surface and the corresponding surface temperature. The hue colour component was used as the independent variable in an eighth order polynomial calibration function, with temperature as the dependent variable. The

associated error in temperature is on average $\pm 0.155^0C$, or $\pm 0.6\%$, for the range between $21.6^0C$ to $30^0C$. This compares well with the results from [53] where a temperature error less than $0.3^0C$ was reported for a $15^0C$ band liquid crystal used in a two-temperature situation, and using a different hue, saturation, intensity (HSI) colour space transformation.

Script programs were developed within the Inspector-32 environment to automate all the above procedures. Finally, the calibration function was incorporated in a software routine and used to map out thermal regions of interest based on resolved pixel hue input data.

## 3.5 Summary

The colour change properties of a wide-band thermochromic liquid crystal were used to determine the temperature of a TLC instrumented surface.

A high performance imaging system which includes a white light system, a component colour video camera, a 32-bit colour frame grabber, and a host computer was developed and implemented. This imaging system provides higher accuracy of the colour representation than colour photography, S-VHS (Super-Video Home System) tape recording, and S-VHS disk recording.

The hue component from the RGB to HSL colour space transformation was used in the colour calibration of the wide-band thermochromic liquid crystal. The uncertainty values of the hue component, which are based on calculated standard deviation for a region of 60x40 pixels, are about 50% less for the new imaging system than for the other imaging systems investigated.

Based on the calibrated hue/temperature relationship, the temperature history of the TLC instrumented surface can be determined from the recorded colour change of the liquid crystal.

# Chapter 4

# Compound Angle Jets in Crossflow

This section describes the validation of the newly developed imaging system in a three-temperature application. Integration and development of appropriate software was required to compute the parameters of interest, the film cooling effectiveness ($\eta$) and the film heat transfer coefficient ($h_f$). The geometry is such that the transient heat conduction through the wall material can be assumed one-dimensional. The surface temperature history will then suffice to determine the heat transfer characteristics in a suitable form. Comparison of film cooling effectiveness data obtained by liquid crystal thermography with data obtained by a flame ionization detector technique by Findlay [17] is used to validate the method.

## 4.1 Transient Heat Transfer

The calculation of the heat transfer coefficient directly from Eqn. 1.3 on page 10 requires the measurement of the heat flux $q_w$, temperature of the surface $T_w$, and temperature of the adiabatic wall $T_{ad}$. This is impossible to achieve in a single experiment since measurements on an adiabatic surface ($T_w = T_{ad}$) would provide no information on the heat transfer coefficient. The flow field in an arbitrary three-temperature situation is three-dimensional, and the resulting adiabatic wall temperature distribution varies significantly on the surface of interest. In the past, the effort was often focused on determination of the adiabatic wall temperature in

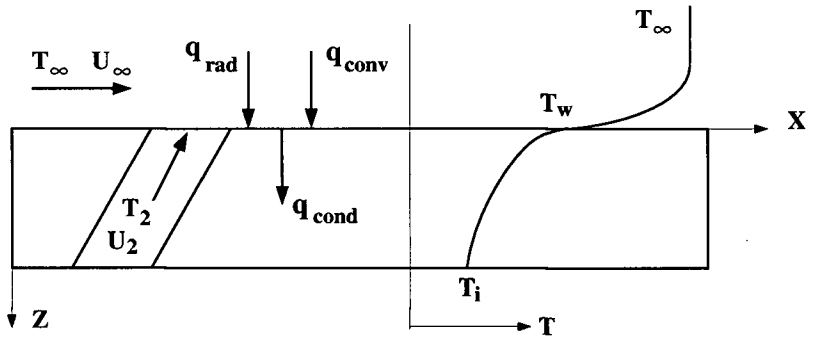


Figure 4.1: General three-temperature arrangement - nomenclature.

the form of film cooling effectiveness, and this is especially true if the heat transfer coefficient $h_f$ was considered to be close to the value without injection $h_0'$. The comprehensive study by Goldstein [19] addresses this topic with emphasis on two-dimensional film cooling situations. To avoid the complications induced by imposing adiabatic wall conditions, a different method initially proposed by Metzger *et al.* [35] uses heat transfer data under different isothermal wall conditions to specify the film cooling performance. The two methods are based on the linearity of the energy equation in temperature for constant property flows, and thus allow for the result to be obtained by superposition of other solutions. These methods were compared and analysed in a study by Eckert [11].

Most of the previous work was carried out in low speed wind tunnels with properly scaled models to keep at least the Reynolds number within the range used in gas turbine applications. The solution to the heat transfer problem is much simplified on larger wind tunnel models if two- or three-dimensional effects are not significant. A one-dimensional formulation would clearly prove advantageous from a computational point of view.

A typical three-temperature situation is summarized in Fig. 4.1 showing a transient temperature profile into a slab.

The temperature of the jet flow ($T_2$) is taken to be different from the temperature of the mainstream flow ($T_\infty$). For a given geometry and generated flow field, the surface temperature downstream of the injection sites becomes a function of the location on the surface and time $T_w(x, y, t)$. The conservation of energy requirements at the interface between

the surface and the fluid can be written for both steady-state and transient conditions in the form:

$$q_{cond} = q_{conv} + q_{rad} \tag{4.1}$$

where the analysis is on a unit area basis [W/m$^2$] with no heat generation and with $q_{cond}$ being the heat flux by conduction from the control surface to the wall medium, $q_{conv}$ the heat flux by convection from the fluid to the control surface, and $q_{rad}$ the radiation exchange from the surroundings to the surface.

Steady-state conditions would require that all parameters be independent of time. This condition is difficult to realize in a heat transfer experiment with a strong three-dimensional flow field and with a large scale model. Steady-state heat transfer experiments are usually associated with uniform boundary conditions in the form of either uniform wall heat flux or uniform wall temperature. As research in the past has shown [28], [24], departure from uniform conditions is accounted for through heat losses and are always somehow hard to quantify. Reaching steady-state conditions is also a time-consuming procedure, and could prove quite expensive when large wind tunnels are used.

A transient heat transfer technique on the other hand, would allow for the time dependence of the temperature field, and the actual experiments could be completed in very short periods of time. To obtain useful correlations of the desired parameters many runs are needed, and so the transient techniques have become increasingly popular among experimentalists. Such an approach is therefore investigated further in this study.

In a first approximation it is considered that heat losses through radiation in Eqn. 4.1 are small, so that the radiation term can be neglected ($q_{rad} = 0$). This is a reasonable assumption since the temperature difference between the surface and the surroundings is small, potentially less than $20^0C$. The energy balance at a particular location on the surface requires then that the heat flux by convection be equal to the heat flux by conduction through the wall. There is now coupling between the external heat transfer and the conduction within the solid wall. The physical properties of the solid wall must then be part of the

solution. With the system initially in thermal equilibrium at temperature $T = T_i$, transient conduction occurs within the solid when a sudden change in temperature is imposed at the wall. Another simplification is found to be useful here, and the assumption is that there is heat transfer in the solid wall only in the positive z-direction shown in Fig. 4.1, and that the wall is semi-infinite in that direction. This idealization is actually very useful in many practical applications where the temperatures within the wall, far from the surface, are not immediately influenced by the change in the surface conditions. The semi-infinite solid formulation is then a convenient approach to the transient heat conduction if the thermally affected region is less than the wall thickness. This situation can always be controlled by limiting the duration of the experiment.

The transient one-dimensional heat conduction in the assumed semi-infinite solid wall is governed by the equation:

$$k\frac{\partial^2 T}{\partial z^2} = \rho c\frac{\partial T}{\partial t} \tag{4.2}$$

where $k$ is the thermal conductivity [W/(mK)] assumed constant in the wall, $\rho$ is the wall density [Kg/m$^3$], $c$ is the specific heat [J/(KgK)] assumed to be a constant for the wall material, and $T$ is the temperature distribution that is function of location and time $T = T(z,t)$. The transport and thermodynamic properties of the solid wall are often linked in one important parameter, the thermal diffusivity $\alpha$ with units of [m$^2$/s]. The thermal diffusivity is the ratio of the thermal conductivity $k$ to the product $\rho c$, the volumetric heat capacity of the wall. For transient heat conduction experiments, materials with low thermal diffusivity are useful since they take longer time to reach a new equilibrium condition.

Before attempting to solve Eqn. 4.2, initial and boundary conditions have to be specified. The initial condition is:

$$T(z, t = 0) = T_i \tag{4.3}$$

and for the boundary conditions instantaneously applied at $t = 0$ there are two equations to

describe the interior boundary and the surface convection at any time $t > 0$. The interior boundary condition is expressed in the form:

$$T(z = \infty, t) = T_i \tag{4.4}$$

and the surface convection condition is expressed by the energy balance requirement:

$$-k \frac{\partial T}{\partial z}\bigg|_{z=0} = h_f (T_{ref} - T_w(t)) \tag{4.5}$$

where $h_f$ and $T_{ref}$ are constants depending only on the flow field and are independent of the transient temperature of the wall. A closed form solution exists for Eqn. 4.2 subject to the boundary conditions (4.3), (4.4), and (4.5) in the form:

$$\frac{T(z,t) - T_i}{T_{ref} - T_i} = \text{erfc}\left(\frac{z}{2\sqrt{\alpha t}}\right) - \exp\left(\frac{z h_f}{k} + \frac{h_f^2 \alpha t}{k^2}\right) \text{erfc}\left(\frac{z}{2\sqrt{\alpha t}} + \frac{h_f \sqrt{\alpha t}}{k}\right) \tag{4.6}$$

Equation 4.6 was adapted from [6], [25]. The solution contains the Gaussian complementary error function defined as:

$$\text{erfc}(u) = 1 - \text{erf}(u) = 1 - \frac{2}{\sqrt{\pi}} \int_0^u \exp(-w^2)\, dw \tag{4.7}$$

with values between unity and zero, for values of $u$ between zero and infinity respectively.

The surface temperature distribution $T = T_w(t)$ can be simply determined from Eqn. 4.6 making the appropriate substitution for the spatial coordinate, $z = 0$. At any time during the transient and at any particular location on the surface of interest, the following expression relates the film heat transfer coefficient $h_f$ and the reference temperature $T_{ref} = T_{ad}$ with the initial equilibrium temperature condition $T_i$, temperature of the surface $T_w$, and physical properties of the wall material $\alpha$:

$$\frac{T_w(t) - T_i}{T_{ad} - T_i} = 1 - \exp\left(\frac{h_f^2 \alpha t}{k^2}\right) \text{erfc}\left(\frac{h_f \sqrt{\alpha t}}{k}\right) \tag{4.8}$$

The form of Eqn. 4.8, which describes a three-temperature situation, is very similar to the solution to the more common two-temperature situation [6], [25], where $T_{ad} = T_\infty$ and the heat transfer coefficient is $h_0'$ as defined by Eqn. 1.4 on page 10. The major difficulty in a film cooling application lies in the fact that the reference, or adiabatic wall, temperature is unknown and is function of the location on the surface, mainstream and jet flow temperatures, and the degree of mixing between them. For each known location on the surface, Eqn. 4.8 has therefore two unknowns, the film heat transfer coefficient and the adiabatic wall temperature. The latter can be reduced by the use of Eqn. 1.6 on page 12 so that the denominator in the left hand side of Eqn. 4.8 now reads:

$$T_{ad} - T_i = \eta(T_2 - T_\infty) + (T_\infty - T_i) \tag{4.9}$$

and the unknowns conveniently become the film heat transfer coefficient $h_f$ and the film cooling effectiveness $\eta$. The experiment has to produce only the value of the surface temperature during the transient $T_w(t)$ at all desired locations on the surface of interest. Two equations in the form of Eqn. 4.8 can be written for each point on the surface and at different times during the transient $t = t_a$ and $t = t_b$, to provide the two needed relationships for the simultaneous calculation of $h_f$ and $\eta$ at that location.

Theoretically, any two time events can be chosen from the transient history during one test, or two separate tests can be conducted with the same flow field but different flow temperatures to calculate a time independent heat transfer coefficient and film cooling effectiveness. The latter technique has been used in the past [51], [12], [13] in three-temperature situations, and can be categorized as double sampling or double event procedure. It is noted at this point that a double event procedure provides the minimum required information for calculating $h_f$ and $\eta$ in a three-temperature situation, while a single event procedure could provide all the necessary information for calculation of the heat transfer coefficient (Eqn. 1.4 on page 10) in a two-temperature situation.

In typical jets in crossflow applications, unsteady vortex structures were often observed downstream of the injection sites [2], [21]. In such situations, the double sampling tech-

niques, as used in the past, cannot lead to an accurate representation of the heat transfer characteristics. Multiple sampling has to be considered in these cases, and the full time history of the surface temperature has to be available for data reduction. Locally time averaged $h_f$ and $\eta$ could then provide higher accuracy in the representation of the heat transfer process on the surface of interest. Even in a perfectly steady flow field, the multiple sampling technique can improve the accuracy by noise minimization through the time averaging process. The term noise is used here to describe random errors in temperature measurement.

This study will further focus on a multiple sampling technique related to the transient heat conduction process with convective boundary conditions in a film cooling, three-temperature situation. This new technique has also the advantage that $\eta$ and $h_f$ can be calculated simultaneously during a single test, while two separate tests were needed in the past [51], [12], [13]. The goal is to develop a low cost, efficient method for calculation of the film heat transfer coefficient $h_f$ and the film cooling effectiveness $\eta$ in arbitrary film cooling arrangements.

The underlying assumptions include: small temperature differences and constant property flows; small radiation and buoyancy effects; transient one-dimensional heat conduction response within the solid wall for points close to the surface, and a sudden change in surface conditions. These assumptions will be addressed in subsequent sections of this study.

## 4.2 Jet Temperature Data Acquisition

The solution to the transient impulsive one-dimensional heat conduction problem with convective boundary conditions is described by Eqn. 4.8 on page 107 for the three-temperature situation. The impulsive condition on temperature is required in either the mainstream or the jet flow. The temperature history of the surface of interest ($T_w$) is given by the colour change of the applied liquid crystal, while the temperature of the mainstream ($T_\infty$) and the temperature of the jet flow ($T_2$) are monitored by thermocouples. In this study, the initial

condition ($T_i$) corresponds to all temperatures being equal, $T_\infty = T_2 = T_i$, and the impulsive temperature change is imposed on the jet flow. If a step change in $T_2$ is not possible, the whole jet temperature history is needed and has to be recorded during the transient.

A temperature data acquisition system was implemented consisting of two type K thermocouples connected to a specially designed amplifier/cold junction compensator printed circuit board. The circuit was built around two Analog Devices AD595 [56] monolithic thermocouple amplifiers with cold junction compensation working in dual supply operation. The AD595 output voltage is linear with temperature in the range of interest from $T = 10^0C$ to $T = 40^0C$ at 10 mV/$^0$C. The thermocouple circuit output voltage was differentially applied at the input of a National Instruments Lab-PC+ data acquisition board installed in an IBM compatible 386 PC, to minimize the common-mode noise voltage. The voltage carrying wires were also shielded and then grounded to the PC casing. Excellent noise rejection was achieved with this setup. Data acquisition was controlled through specialized Labtech Notebook version 8.1 software. Temperatures were sampled at 200 Hz to allow for further noise cancellation by appropriate averaging, and were recorded directly onto the PC hard drive for the entire duration of the transient experiment.

## 4.3 Wind Tunnel Setup

The experiments were performed in the Aerodynamics Laboratory at the University of British Columbia. The wind tunnel used was referred to as the Blue wind tunnel and is an open-circuit forced-draft tunnel. The crossflow was driven by a fan coupled to a 3.8 KW D.C. motor. The maximum tunnel air speed was 12 m/s and was measured by Pitot tube. The test section was 1020 mm x 405 mm x 270 mm and was located downstream of a 4:1 area contraction section. The wind tunnel side walls were made of clear plexiglass for observation purposes. A boundary layer trip wire was fixed onto the tunnel floor just upstream of the test section to ensure a boundary layer whose thickness was constant across the span of the tunnel and was also steady with a fixed transition point.

The test section was modified to include a specially designed removable tunnel floor, and a removable non-glare glass tunnel ceiling. The removable floor is basically a flat plate made of $\frac{1}{2}$ inch thick Plastic G sheet with low thermal conductivity properties. The physical properties of interest of the Plastic G are density $\rho = 1187.6$ Kg/m$^3$, thermal conductivity $k = 0.1872$ W/(mK), and specific heat $c = 1464$ J/(KgK).

The removable plate contained a row of 7 square jets of size (the symbol $d$ - diameter is used for size, from analogy with a round jet) $d = \frac{1}{2}$ inch angled at $30^0$ with the tunnel floor and at $45^0$ with the crossflow. Only the middle 5 jets were used in the experiments, and the marginal 2 jets were taped over. The row of jets was located 406 mm from the test section entrance. The length of the jet duct was 4 times its diameter, so $L/d = 4$. The jets were spaced 3 jet diameters apart in the spanwise direction so that $S_r = 3d$. A rectangular patch of dimensions around 6dx10d was instrumented with a wide-band liquid crystal, by the method described in section 3.1 of this study, and covered the region downstream of the middle jet. The Thermax wide-band thermochromic liquid crystal [60] was sprayed onto the surface using an air brush. The instrumented liquid crystal surface was illuminated with the white light system described in section 3.2.1. Two Optimarc lamps were symmetrically placed above the tunnel ceiling, and the incident light onto the instrumented liquid crystal surface came uniformly through the tunnel non-glare glass ceiling. The colour video camera was placed outside the tunnel, perpendicular to the centre point of the liquid crystal instrumented patch, such that the camera lens was perfectly alligned with the tunnel ceiling and shot through an opening in the non-glare glass ceiling. Details of this arrangement are shown in Fig. 4.2.

The removable flat plate fitted tight on top of a metal cylindrical-plenum rectangular collar, and the clearance became hermetically sealed when the plate was screwed down onto the collar. Thermal insulation was attached on the plenum side of the removable plate to avoid heating of the plate by the plenum flow. A stove heater coil was placed inside the plenum on top of a metal radial diffuser plate, the electrical wires being fed through a small sealed hole in the bottom plate of the plenum. A honeycomb was also inserted in the plenum to prevent a swirling flow pattern inside the plenum. The metal plenum was further wrapped

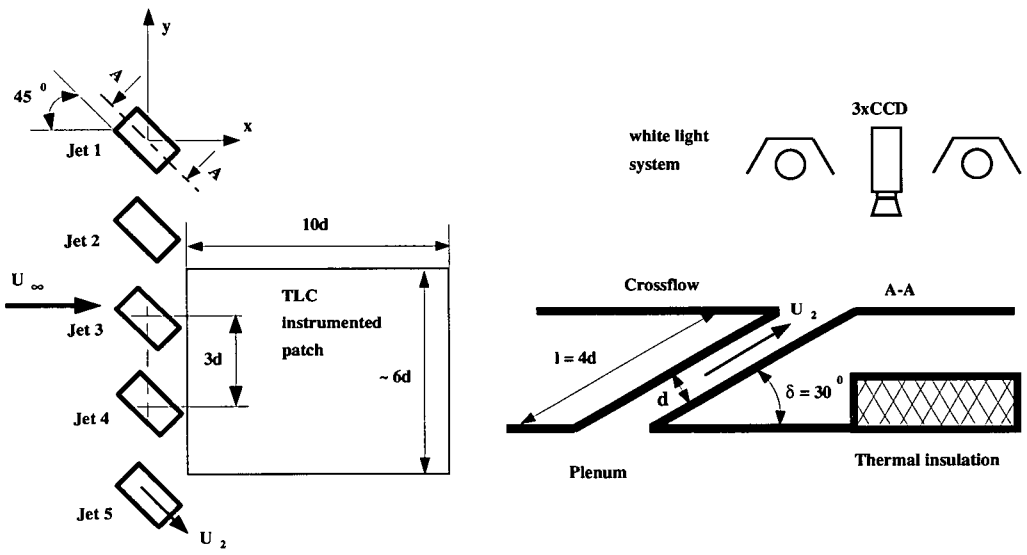


Figure 4.2: Wind tunnel arrangement.

in thermal insulation along its entire length to minimize the thermal radiation losses from the heated plenum to the surroundings.

The jet flow was supplied by a rotary screw Quincy compressor, filtered through multiple oil traps, metered with the aid of a rotameter such that the jet Reynolds number was kept constant at a value of $Re_2 = 5000$. The jet air was heated in an in-house designed and built in-line heat exchanger, diverted by a system of two-way direct-lift solenoid valves so that it flowed through the plenum, and finally discharged into the mainstream boundary layer through the row of compound angle ducts. The temperature of the jets was recorded at a sample rate of 200 Hz by two type K thermocouples with the setup described in section 4.2. The two thermocouples were placed just inside of the two marginal square ducts out of the five square ducts used, so that the flow through the middle jets (used for thermal mapping of the region downstream) was not disturbed. The final jet temperature was found by averaging the data recorded from the two thermocouples. A block diagram of the entire setup is shown in Appendix B.

With all the hardware and software in place, the experiments proceed in the following sequence:

1. The white light system is turned on. The air line is opened and the flow rate is set with the use of the installed pressure regulators. The wind tunnel motor is turned on and some arbitrary air speed is set for ventilation of the test section area.

2. The removable flat plate is unscrewed from the plenum collar and lifted in the middle of the wind tunnel test section, alligned with the mainstream flow. The plenum discharge is partially obstructed by a removable piece of Plastic G sheet, to avoid the flow of the colder mainstream into the plenum.

3. The power to the in-line heater is turned on, as well as the power to the inside plenum heater coil. A variac is used to adjust the heater power.

4. The hot air flow is routed through the metal plenum until a relatively uniform temperature of the plenum metal skin is reached, and the plenum discharge air temperature is around $40^0C$. The discharge temperature is measured by another type K thermocouple connected to an OMEGA OMNI-CAL calibration unit. The jet air flow rate is checked and eventually corrected. The tunnel air speed is set according to the desired mass flow ratio $M = (\rho U)_2/(\rho U)_\infty$. The time required to achieve these conditions is anywhere from 60 to 90 minutes.

5. The imaging system and the temperature data aquisition system are now initialized. The transient is set for 30 seconds, with colour image capture at 5 fps. A total of 150 frames are captured during each transient. The jet flow is switched by two solenoid valves and routed to the surroundings.

6. The duct exits are covered during this period to avoid entrainment of the plenum air by the mainstream. The plenum discharge obstruction plate is removed and the liquid crystal instrumented flat plate is lowered and screwed onto the plenum collar. The duct exits are now uncovered and the tunnel lateral window is sealed.

7. The image sequence capture and temperature data acquisition software are started simultaneously with the jet flow being switched and routed through the plenum.

8. At the end of the run the data are stored onto hard drives for further processing. The heater power is turned off and jet air is directed through the system until it has cooled. A new run follows the same procedure and can be repeated after a couple of hours when the instrumented flat plate temperature has cooled to the mainstream temperature.

Values of film cooling effectiveness $\eta$ are available from the flame ionization detector technique study by Findlay [17], using the same jet geometry and the same wind tunnel at the University of British Columbia. For direct comparison of $\eta$, the flow conditions and the mass flow rates used in this validation study match closely the conditions in [17]. Three mass flow ratios were used M=0.5, 1.0, and 1.5.

In summary, a wind tunnel setup is described for the investigation of three-temperature situations by a transient heat conduction technique. The slab temperature was equal to the temperature of the mainstream at the beginning of the transient, and the required boundary condition of sudden temperature change was provided by heating the jet flow. The jet Reynolds number was kept constant at a value of $Re_2 = 5000$ in all experiments, while mass flow ratio adjustments were made by modifying the wind tunnel air speed. During the 30 second transients the images were captured at 5 fps and the jet temperature was recorded by two thermocouples at a sampling rate of 200 Hz.

## 4.4 Solution Algorithms

Each experimental run generated a sequence of 150 frames contained in an Audio Video Interleave (AVI) file. Each frame consisted of 32-bit RGBx data for 640x480 pixels. The total amount of RAM required to store each sequence file amounts to 640x480x4x150=184,320,000 byte=174 MB.

The same region of interest (ROI) was selected from each frame and covered a streamwise distance of approximately 10 jet diameters and a spanwise distance of 3 jet diameters, or 416x124 pixels. The RGB to HSL colour space transformation was applied on the selected ROI and the resolved hue values were stored in a newly created Truevision TARGA

(TGA) [59] binary file. A script program was written to automate this procedure and store the sequence of 150 TGA files on the hard drive.

A C routine containing the calibration function was implemented to reduce the computational domain using a 4x4 pixel grid, and to record the temperature at each cell based on the averaged hue value over the 16 pixel cell. Each cell covered a physical area on the surface of around 1.5 mm$^2$. A new file containing 104x31=3224 temperature data points was stored on the hard drive for each of the 150 TGA files. The temperature history of the TLC instrumented surface ($T_w(t)$) was then known.

Using the approach described in section 4.1, the film cooling effectiveness $\eta$ and the heat transfer coefficient $h_f$ can be simultaneously obtained from the solution of a system of two non-linear equations in the form of Eqn. 4.8 on page 107. With the setup used in this study, the mainstream temperature is equal to the initial temperature, so that $T_i = T_\infty$ in both Eqn. 4.8 and Eqn. 4.9. For an arbitrary time event pair, $t = t_a$ and $t = t_b$, $\eta$ and $h_f$ can be found from the solution of the following system of equations:

$$\frac{T_w(t_a) - T_\infty}{\eta(T_2 - T_\infty)} = 1 - \exp\left(\frac{h_f^2 \alpha t_a}{k^2}\right) \mathrm{erfc}\left(\frac{h_f\sqrt{\alpha t_a}}{k}\right) \tag{4.10}$$

$$\frac{T_w(t_b) - T_\infty}{\eta(T_2 - T_\infty)} = 1 - \exp\left(\frac{h_f^2 \alpha t_b}{k^2}\right) \mathrm{erfc}\left(\frac{h_f\sqrt{\alpha t_b}}{k}\right) \tag{4.11}$$

If a step change in the temperature of the jet flow ($T_2$) is achieved, Eqn. 4.10 and Eqn. 4.11 combine to give one equation with one unknown, the heat transfer coefficient:

$$\frac{T_w(t_a) - T_\infty}{T_w(t_b) - T_\infty} = \frac{1 - \exp\left(\frac{h_f^2 \alpha t_a}{k^2}\right) \mathrm{erfc}\left(\frac{h_f\sqrt{\alpha t_a}}{k}\right)}{1 - \exp\left(\frac{h_f^2 \alpha t_b}{k^2}\right) \mathrm{erfc}\left(\frac{h_f\sqrt{\alpha t_b}}{k}\right)} \tag{4.12}$$

and $\eta$ can be then calculated by replacing $h_f$ in either Eqn. 4.10 or Eqn. 4.11. But a true step change in the temperature of the jet flow could not be achieved in the experiments, so that the temperature of the jets was actually a function of time, $T_2 = T_2(t)$. This information was incorporated in the solution to the transient heat transfer problem, described by Eqn. 4.8,

by a method similar to that described in [36] where the actual temperature rise was obtained from a superposed set of incremental steps. The fundamental solution becomes:

$$T_w(t) - T_\infty = \sum_{i=1}^{N} \left\{ 1 - \exp\left[ \frac{h_f^2 (t - \tau_i)}{\rho c k} \right] \mathrm{erfc}\left[ \frac{h_f \sqrt{t - \tau_i}}{\sqrt{\rho c k}} \right] \right\} \eta (\Delta T_2)_i \qquad (4.13)$$

The number of time steps in Eqn. 4.13 was taken to be equal to the number of video frames, so that N=150. A new algorithm was developed in this study to calculate the values of $h_f$ and $\eta$, and this procedure is further described. For any arbitrary time event pair, $t = t_a$ and $t = t_b$, two equations in the form of Eqn. 4.13 combine to give one non-linear equation for the unknown variable $h_f$ in the form:

$$\frac{T_w(t_a) - T_\infty}{T_w(t_b) - T_\infty} = \frac{\sum_{i=1}^{N_a} \left\{ 1 - \exp\left[ \frac{h_f^2 (t_a - \tau_i)}{\rho c k} \right] \mathrm{erfc}\left[ \frac{h_f \sqrt{t_a - \tau_i}}{\sqrt{\rho c k}} \right] \right\} (\Delta T_2)_i}{\sum_{i=1}^{N_b} \left\{ 1 - \exp\left[ \frac{h_f^2 (t_b - \tau_i)}{\rho c k} \right] \mathrm{erfc}\left[ \frac{h_f \sqrt{t_b - \tau_i}}{\sqrt{\rho c k}} \right] \right\} (\Delta T_2)_i} \qquad (4.14)$$

and $\eta$ can be thus calculated from the wall temperature response at either time event, $t = t_a$ or $t = t_b$, for example:

$$\eta = \frac{T_w(t_a) - T_\infty}{\sum_{i=1}^{N_a} \left\{ 1 - \exp\left[ \frac{h_f^2 (t_a - \tau_i)}{\rho c k} \right] \mathrm{erfc}\left[ \frac{h_f \sqrt{t_a - \tau_i}}{\sqrt{\rho c k}} \right] \right\} (\Delta T_2)_i} \qquad (4.15)$$

Equation 4.14 and Eqn. 4.15 are solved numerically for a series of time event pairs and the final values of $h_f$ and $\eta$ are obtained by averaging. The grid cells on the surface where the temperature change is less than the estimated average error in temperature of $\pm 0.155^0 C$ (see Fig. 3.17 on page 101) are excluded from the calculations. These are regions uncovered by the film cooling jets, so that the film cooling effectiveness is basically zero and the transient heat conduction approach does not apply. Any attempt to solve Eqn. 4.14 and Eqn. 4.15 here would produce an error and the program will stop. The heat transfer coefficient is also assigned a value of zero in these regions, so that $h_f = 0$ and $\eta = 0$ here and these values are not produced by computations.

## 4.5 The Time Event Pairs

An important issue is to be raised at this point, with respect to the choice of the time event pair, $t = t_a$ and $t = t_b$. In previous studies of impulsively started transient conduction it was assumed that, $h_f$ and $\eta$ being theoretically independent of time, any time event pair could be used and the choice was one of convenience only.

The investigation will proceed for the simplest case of a sudden change in temperature for which the solution is in the form of Eqn. 4.12, but the argument also applies to the present situation described by Eqn. 4.14. The left hand side only of Eqn. 4.12 represents data obtained by measurement ($T_w(t)$ from the resolved local colour and $T_\infty$ measured by a thermocouple) and will be further referred to by the symbol $\bar{\Psi}$, while the right hand side accounts for the effects of time and physical properties of the material used.

$$\bar{\Psi} = \frac{\Psi_a}{\Psi_b} = \frac{T_w(t_a) - T_\infty}{T_w(t_b) - T_\infty} \tag{4.16}$$

Time is measured indirectly by setting the duration of the transient for both video sequence capturing, at specified frame rate, and jet flow temperature recording, at specified sampling frequency. The right hand side of Eqn. 4.12 represents a non-dimensional wall temperature profile and will be further referred to by the symbol $\bar{\Theta}$:

$$\bar{\Theta} = \frac{\Theta_a}{\Theta_b} = \frac{1 - \exp\left[\frac{h_f^2 t_a}{\rho c k}\right] \mathrm{erfc}\left[\frac{h_f \sqrt{t_a}}{\sqrt{\rho c k}}\right]}{1 - \exp\left[\frac{h_f^2 t_b}{\rho c k}\right] \mathrm{erfc}\left[\frac{h_f \sqrt{t_b}}{\sqrt{\rho c k}}\right]} \tag{4.17}$$

Equation 4.17 is graphed in Fig. 4.3 as a function of $h_f/\sqrt{\rho c k}$, for different time event pairs relevant to the transients used in this study; one of the time events was fixed at $t_b = 30$ s and the product $\sqrt{\rho c k} = 571$ $\mathrm{Ws^{1/2}/(m^2K)}$ for the Plastic G used.

As a general trend, the slope for all curves in Fig. 4.3 decreases at higher values of $h_f$, and the effect is more pronounced when the two time events are closer. This in turn, has direct implications for the accuracy with which the heat transfer coefficient can be determined. Small experimental errors in the measurement of $\bar{\Psi}$ can produce large errors in

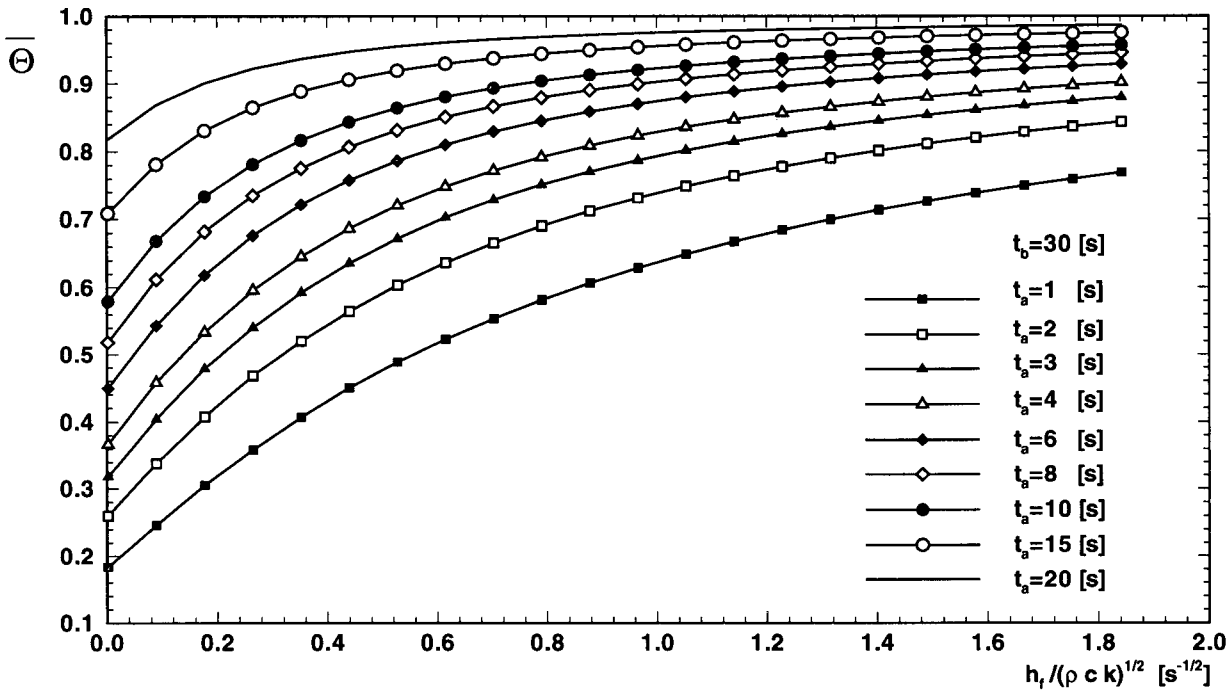


Figure 4.3: Non-dimensional wall temperature profiles.

the calculation of $h_f$, especially for higher $h_f$ and for closer time events. For example, for the curve $t_b = 30$ s and $t_a = 20$ s, a value of $\bar{\Psi} = \bar{\Theta} = 0.96 \pm 1\%$ would produce a heat transfer coefficient $h_f = 341 \pm 93$ W/(m$^2$K). This is due to the fact that the closer the time events are, the smaller the change in the temperature of the surface at any one point is. This effect is magnified by the behaviour of the low thermal diffusivity material used, in particular the product $\sqrt{\rho ck}$ acts as a heat transfer coefficient damping factor in the solution of the transient problem.

To further exemplify the errors in the determination of $\eta$, the simpler case described by Eqn. 4.10 on page 115 is considered. For the same situation with $t_a = 20$ s and a non-dimensional temperature ratio determined within $\pm 1\%$ that produced a heat transfer coefficient of $h_f = 341 \pm 93$ W/(m$^2$K), the right hand side of Eqn. 4.10 is determined with an error of around $\pm 5\%$ only. The error in $\eta$ can be thus calculated as $\epsilon_\eta = \sqrt{(\pm 1\%)^2 + (\pm 5\%)^2} = \pm 5.1\%$. In this example, the film cooling effectiveness was calculated more accurately than the heat transfer coefficient.

In conclusion, the time events in Eqn. 4.14 have to be as far apart as possible to minimize

the error in heat transfer coefficient. The maximum value for the time $t_a$ is set by the requirement that there be a measurable temperature change at the farthest downstream points in the region of interest, while the value for $t_b$ is set to ensure the semi-infinite wall assumption that the thermally affected region of the wall be less than the wall thickness.

The minimum time required for a finite temperature change, at any distance into the wall, can be calculated by assuming that the surface temperature is suddenly increased from $T_i = T_\infty$ to the maximum measured jet temperature. This is equivalent to modified boundary conditions which include infinite heat transfer coefficient ($h_f = \infty$) and film cooling effectiveness value of one ($\eta = 1$). The solution to the transient one-dimensional conduction equation then becomes (adapted from [25]):

$$\frac{T_w(t) - T_\infty}{max(T_2) - T_\infty} - \text{erfc}\left[\frac{z}{2\sqrt{\alpha t}}\right] = 0 \tag{4.18}$$

Equation 4.18 is solved numerically for an imposed $\delta T = T_w(t,z) - T_\infty$ to give the minimum time required for a $\delta T$ temperature increase to appear at the specified $z$ coordinate. The actual period of time is always longer due to the finite $h_f$, $\eta < 1$, and the time required for the jet temperature to reach its maximum value during any one experimental run. For example, the value $t_b = 30$ s used in the previous analysis corresponds to the minimum time it takes to increase the temperature in the middle of the $\frac{1}{2}$ inch thick wall ($z = d/2 = \frac{1}{4}$ inch) by $0.2^0C$. The minimum time required for a $0.01^0C$ temperature increase at the plenum side of the wall (or $z_{max} = d = \frac{1}{2}$ inch) is 65 seconds. Therefore, the value $t_b = 30$ s corresponds to a thermally affected region of less than half the wall thickness during the actual runs.

## 4.6 Experimental Results

Three cases were investigated corresponding to the mass flow ratios M=0.5, 1.0, and 1.5, and the spanwise values of $\eta$ were compared, at the same downstream locations, with the values from [17]. The heat transfer coefficient is reported in dimensionless form as the Stanton number, $St = \frac{h_f}{(\rho c_p U)_\infty}$. The reported local values of $\eta$ and $h_f$ actually represent

averaged values over the investigated two adjacent jets, jet number 3 and jet number 4 respectively, shown in Fig. 4.2 on page 112. The reported results account in this way for possible non-uniformities in the TLC's layer thickness, and large scale unsteadiness of the velocity field [2], [21]. The averaging process was done on the recorded colour information of the region of interest. This differs slightly from the approach in [17] where the jet number 3 only was used in the investigation. A periodicity check of the velocity field for these two jets was done in [17] and the results showed that the jets can be considered as part of an infinite row. The film cooling effectiveness results from [17] were obtained using a flame ionization detector technique, similar to that described in section 2 of the present study. Local values of $\eta$ from [17] represent averages of 2000 data points sampled within 15 s.

In the present investigation, the time history of the jets was incorporated by using the multiple sampling technique with $t_a$ covering the first 8 s of the transient in 0.2 s increments, while $t_b = 30$ s for all cases. The final results were obtained by averaging over all the results within the 8 s of computed time history if a solution was available for at least 2 time event pairs. A maximum of $2 \times 36$ data points were thus included in the averaging process.

### 4.6.1 General Trends

Figure 4.4 shows contours of $\eta$ and Fig. 4.5 shows contours of $h_f$ in dimensionless form. Grid cells where a solution was attempted but was not found for at least 2 time event pairs, were discarded and are shown as blank cells in the contour plots.

Interestingly enough, a solution was not possible for all the pixel cells at all time event pairs. As Fig. 4.3 on page 118 shows, once the time event pair is fixed, a solution is only possible if the measured value of $\bar{\Psi}$ intersects the corresponding $\bar{\Theta}$ curve, so that:

$$\bar{\Psi} - \bar{\Theta} = 0 \tag{4.19}$$

The contour plots give a very good indication of the respective area coverage for each of the three mass flow ratios. It is clear that the best coverage is achieved in the M=0.5

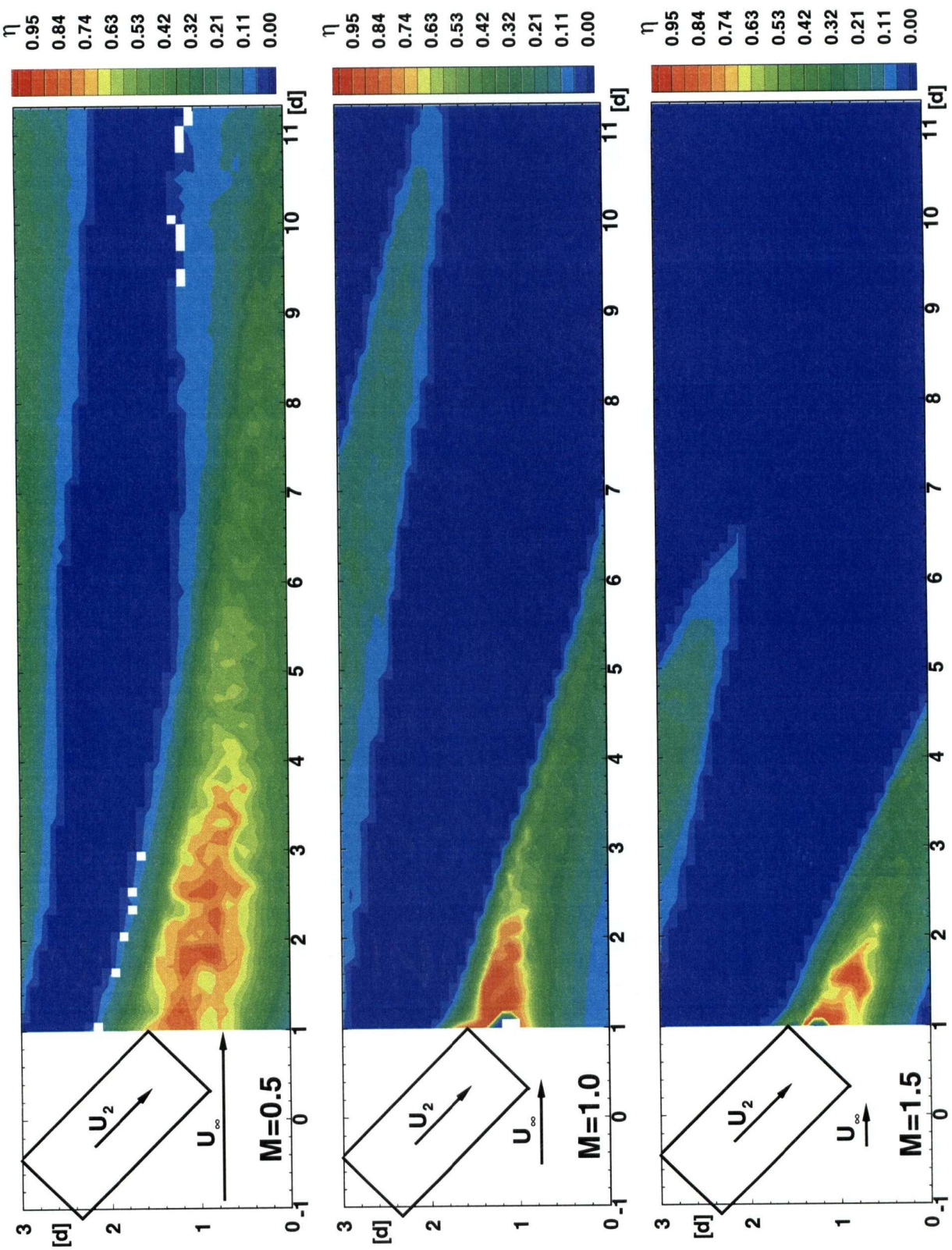


Figure 4.4: Contours of film cooling effectiveness.

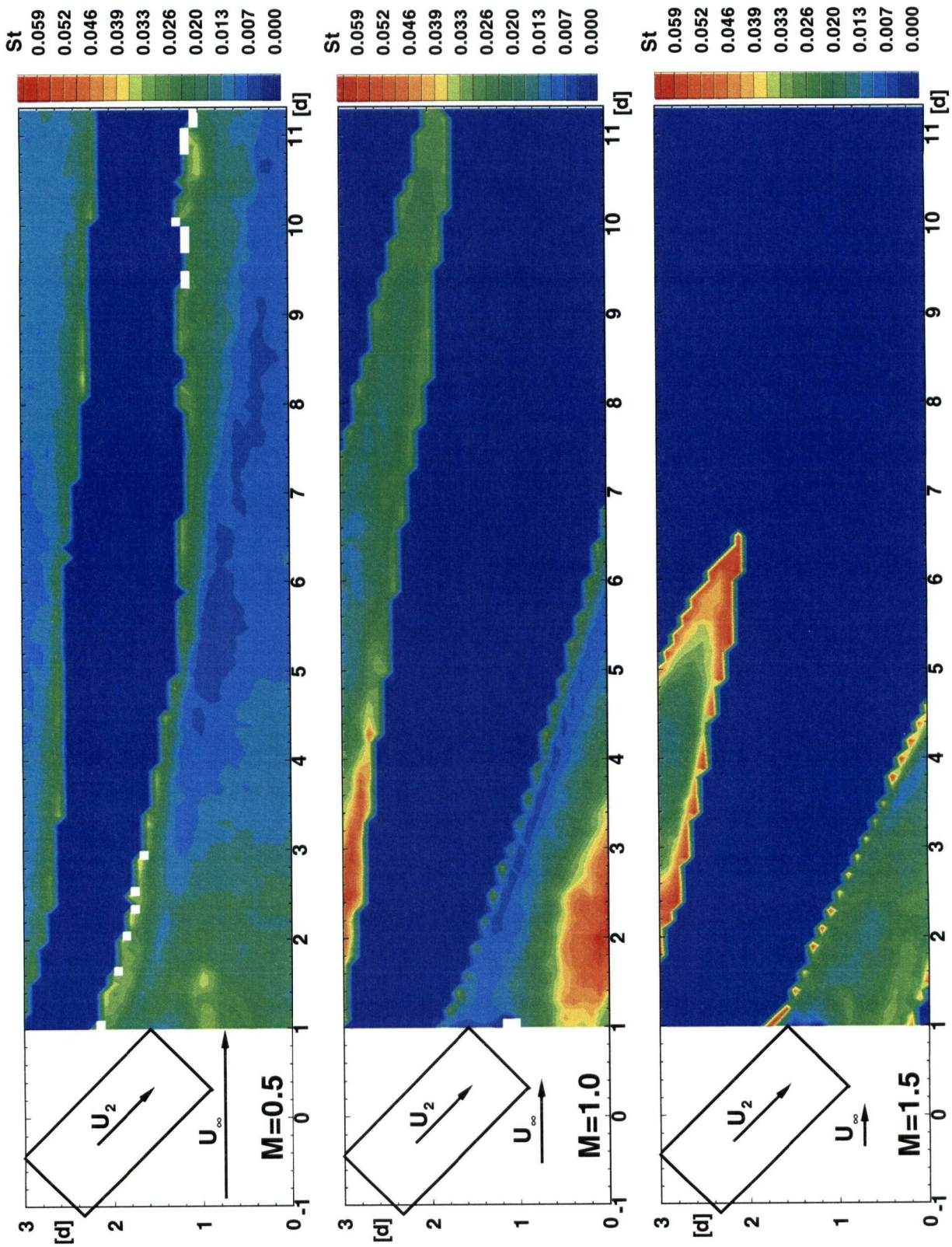


Figure 4.5: Contours of heat transfer coefficient - Stanton number.

case, when the jet is strongly deflected towards the floor by the crossflow. The coverage progressively deteriorates for the M=1.0 and M=1.5 cases, with the poorest coverage in the M=1.5 case. The jet seems to separate from the surface at the higher mass flow ratio, therefore providing extremely low protection of the surface. The region with higher $\eta$ is also significantly larger in the M=0.5 case than in the other two cases. Based on the $\eta$ data alone, the best performance is achieved at M=0.5 for this compound angle configuration.

For all cases, $h_f$ is higher around the sides of the jet, consistent with regions of stronger interaction between the jet, crossflow, and the surface. These regions at the sides of the jet are also characterised by the lowest $\eta$ values. Within the area covered by the jet there are also regions of higher $h_f$; such a region, located immediately downstream of the duct exit in the M=0.5 case, shifts towards one side of the jet in the other two cases with the highest values of the $St$ number in the M=1.0 case. For all cases, regions with lowest $h_f$ are present within the area covered by the jet, rather than on its sides, and at some distance downstream of the injection site, as expected. This trend is more obvious in the M=0.5 case, where there is such a large central region with lowest values of the $St$ number, starting at about 4 diameters downstream of the injection site. The heat transfer coefficient is still at high levels as far as 11 diameters downstream around the sides of the jet for the M=0.5 and M=1.0 cases.

Another important conclusion that can be drawn from Fig. 4.4 and Fig. 4.5, is that regions with highest $\eta$ do not correspond to regions of lowest $h_f$, and regions with highest $h_f$ do not necessarily correspond to regions of lowest $\eta$. This clearly proves the need to determine both $\eta$ and $h_f$ to completely specify the film cooling performance on a surface of interest.

### 4.6.2 Mass Flow Ratio M=0.5

Since the vertical thermal penetration into the wall is less than a half jet diameter everywhere, it was expected that the semi-infinite assumption holds up to locations a half jet diameter around the upstream duct exit corner, where multi-dimensional conduction effects could be

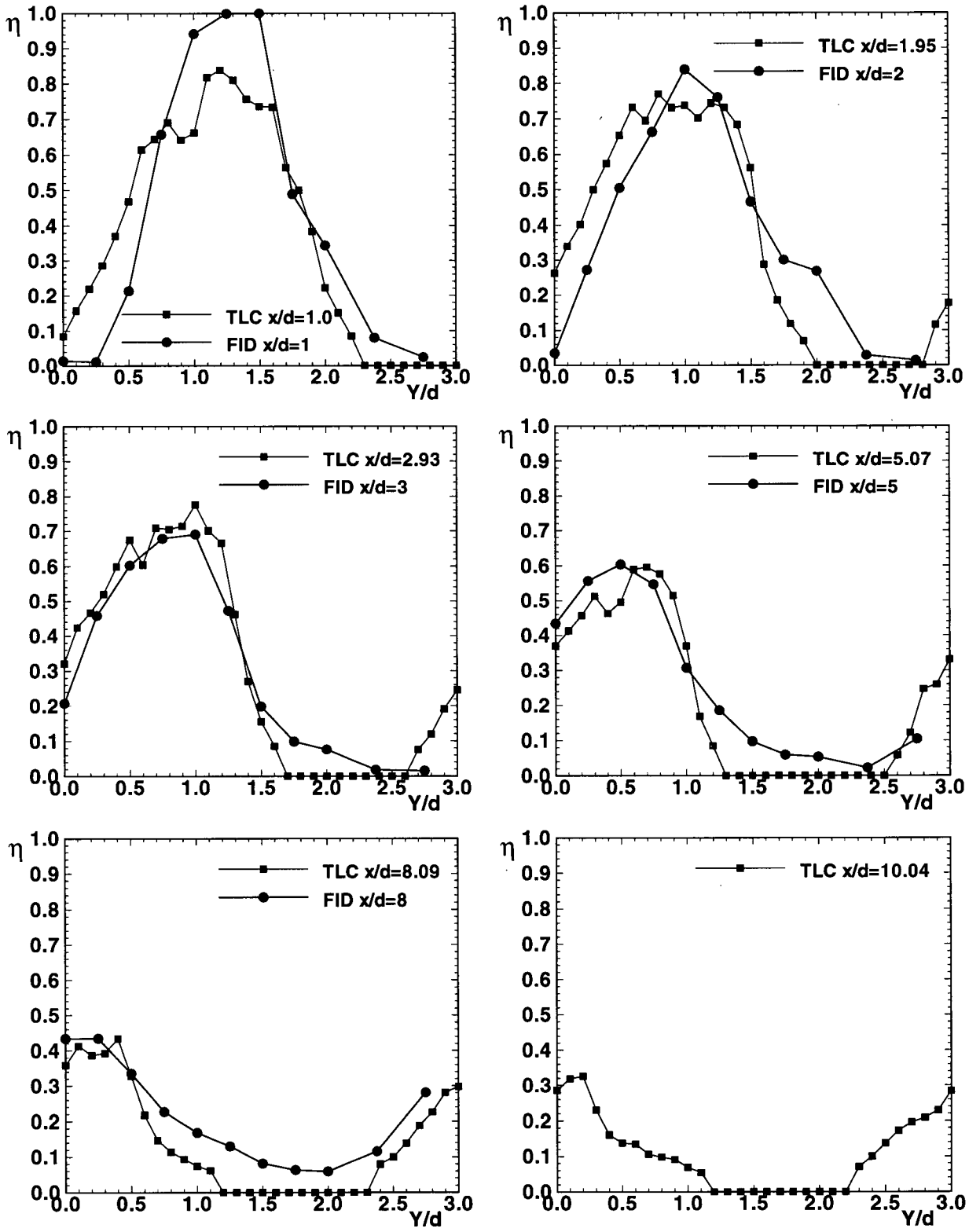


Figure 4.6: Comparison of $\eta$ obtained by the TLC technique with the FID data of Findlay [17], M=0.5.

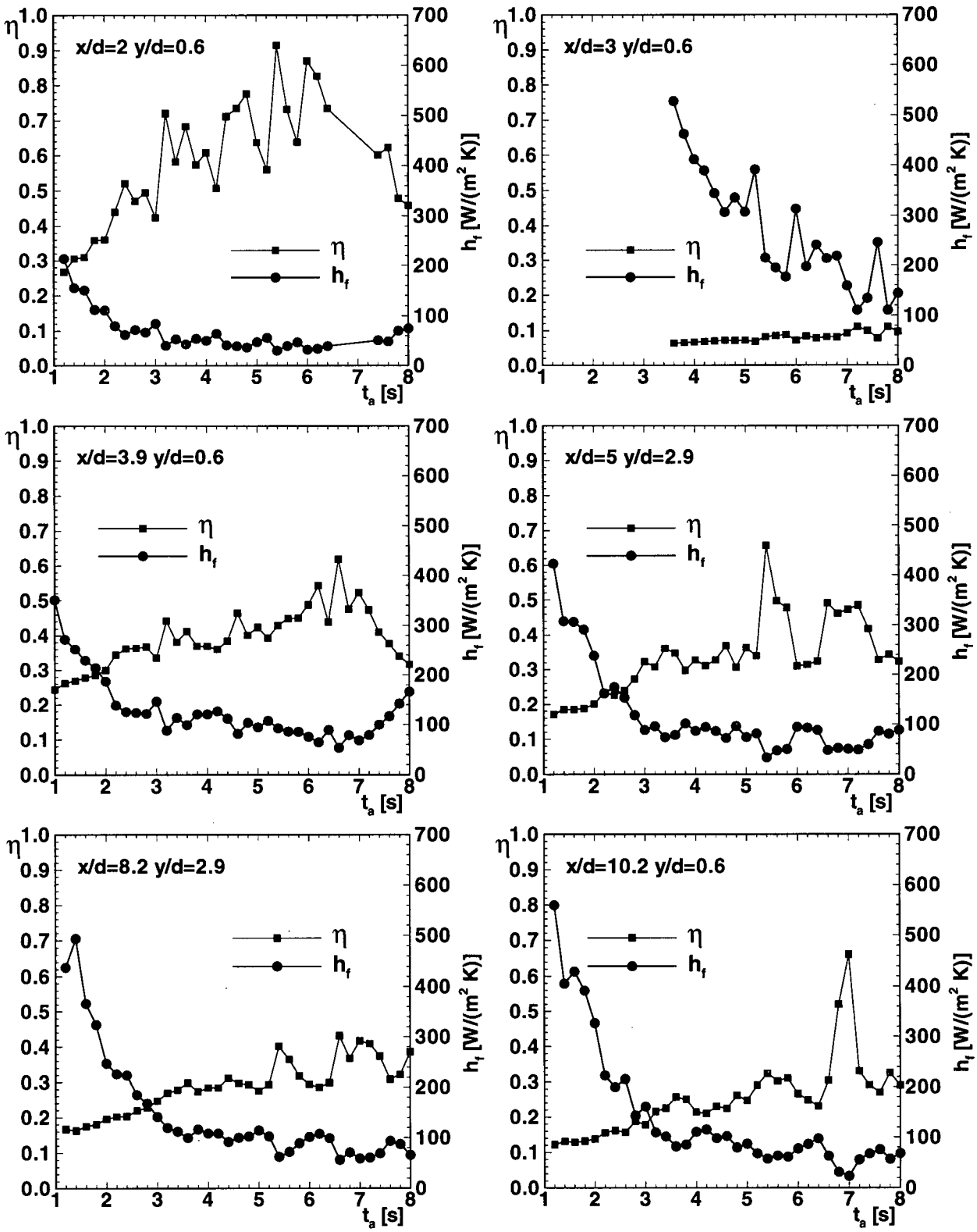


Figure 4.7: Time history of $h_f$ and $\eta$, M=0.5.

important. To further quantify these effects, and to verify the assumptions and the newly developed formulation based on liquid crystal thermography (TLC), comparison is made with film cooling effectiveness data obtained using a flame ionization detector technique [17] (FID).

Figure 4.6 compares spanwise values of $\eta$ at different streamwise locations on the surface. Again, all values of $\eta = 0$ for the TLC technique are not computed but assigned, being indicative of regions where the change in temperature is less than the measured experimental error. Overall, the agreement is very good. Even at the streamwise location $x/d = 1$, in the immediate vicinity of the downstream duct exit, the trends are reproduced by the TLC technique but for a few points around the spanwise location $y/d = 1.5$, the location of the downstream duct exit corner, as expected. For the other downstream locations, the peak values of $\eta$ and their location are well reproduced. Film cooling effectiveness data is not available beyond the streamwise location $x/d = 8$ from the FID technique.

The time history of both $\eta$ and $h_f$ is considered in Fig. 4.7, at a few arbitrarily chosen locations on the surface. It is evident now from these plots, that the average from all time events can best characterise the complex three-temperature situation A single time event pair sampling, as used in the past, could not possibly capture all the details of the transient experiment.

Examination of Fig. 4.7 shows that there is significant scatter in both $h_f$ and $\eta$ parameters at the chosen locations on the surface. In particular, $h_f$ appears to be much higher at the beginning of the transient (the time event pair $t_a$ and $t_b$ further apart) and gradually settles around a more uniform value when the first event in the time pair becomes greater than about 4 seconds ($t_a > 4$ s). This trend is probably caused by the development of the jet flow in the early stages of the transient with the associated stronger perturbation of the crossflow boundary layer. The film cooling effectiveness is not affected by this behaviour of $h_f$ at small values of $t_a$, but appears very variable when corresponding values of $h_f$ are below around 50 [W/(m$^2$K)]. A definite conclusion cannot be inferred from these arbitrarily sampled locations alone, since they represent only about 0.2% of the calculated pixel cells on

the surface. If more details are required at some particular location, the time history at that pixel cell can be recovered easily from the time history files, and the appropriate treatment can be applied based on the observed trends.

These fluctuations of both parameters also indicate that lateral conduction effects are indeed negligible, since these would tend to even out the fluctuations, so that the local response can be considered one-dimensional. The wide scatter of the higher values of $h_f$ is not entirely surprising. Accompanying flow visualisation studies in [17] [2] clearly show that the generated flow field is turbulent, the jet flow developing into a strong vortical structure with oscillations present in particular at the interface between the jets and the crossflow. For the case of injection through a row of square jets perpendicular to the crossflow at a jet Reynolds number of $Re_2 = 4700$, a large scale unsteady flow structure was present and was estimated to be 30 times larger than typical turbulence structures [2]. For the present situation, the jet penetration of the crossflow boundary layer is also minimum at this lower mass flow ratio, so that the floor interaction between the jet and the crossflow is the most significant. The heat transfer coefficient is strongly dependent on the generated flow field and higher values of $h_f$ are indicative of regions of vigorous interaction between the jets and the crossflow. It is mainly in these regions that the observed flow oscillations would immediately translate into fluctuations of the heat transfer coefficient and probably higher average values of $h_f$.

The use of the first 8 seconds of the transient for the first event in the time pair, appears now as a legitimate choice since no deterioration of the results is observed at the later time events. This allows for the use of as many as $2 \times 36$ time event pairs in the calculation of both $h_f$ and $\eta$.

### 4.6.3 Mass Flow Ratio M=1.0

Figure 4.8 shows the comparison of $\eta$ for the M=1.0 case. Again, the agreement between the results obtained with the two methods, liquid crystal thermography (TLC) and flame ionization detector technique (FID) respectively, is good. At some of the positions shown

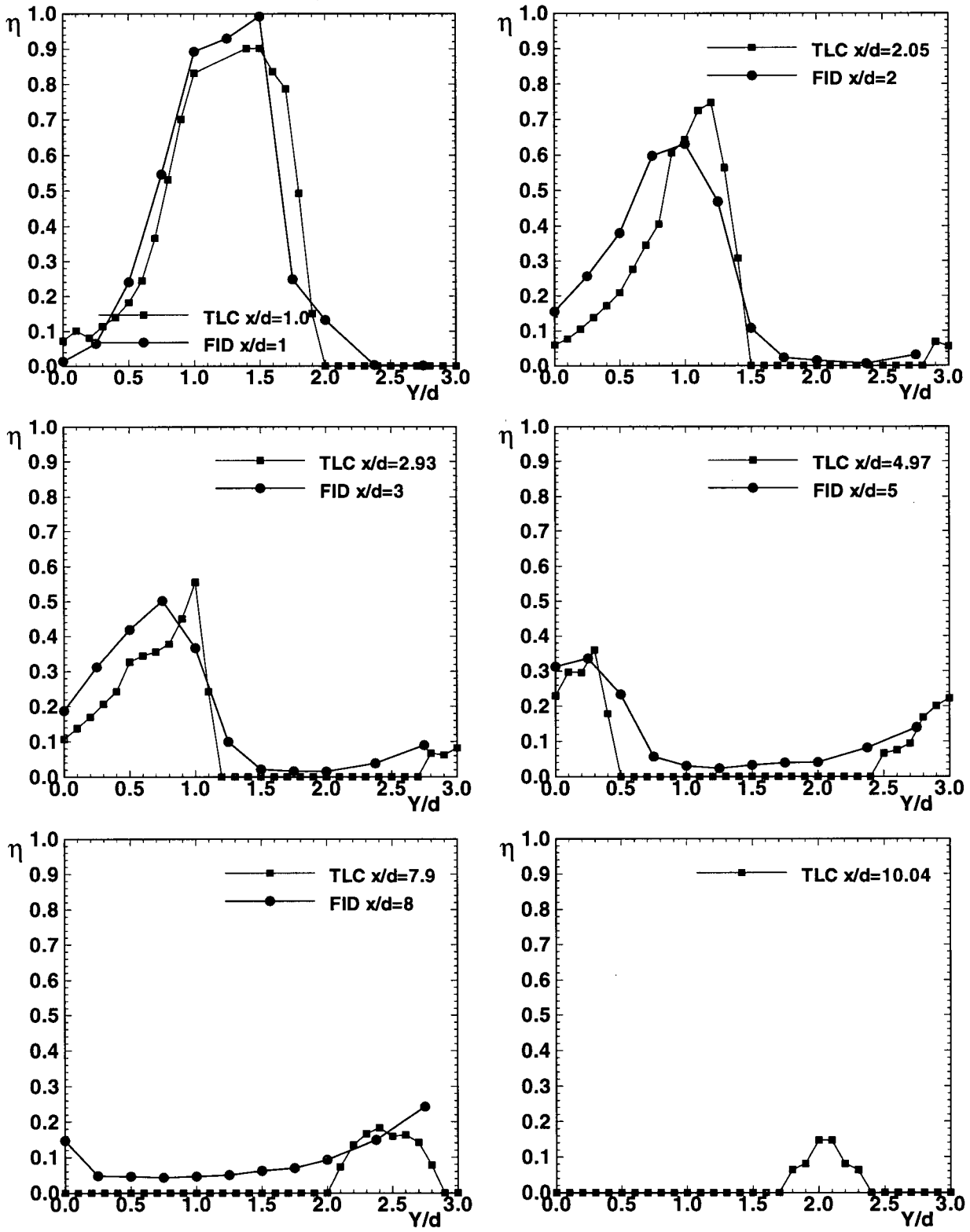


Figure 4.8: Comparison of $\eta$ obtained by the TLC technique with the FID data of Findlay [17], M=1.0.

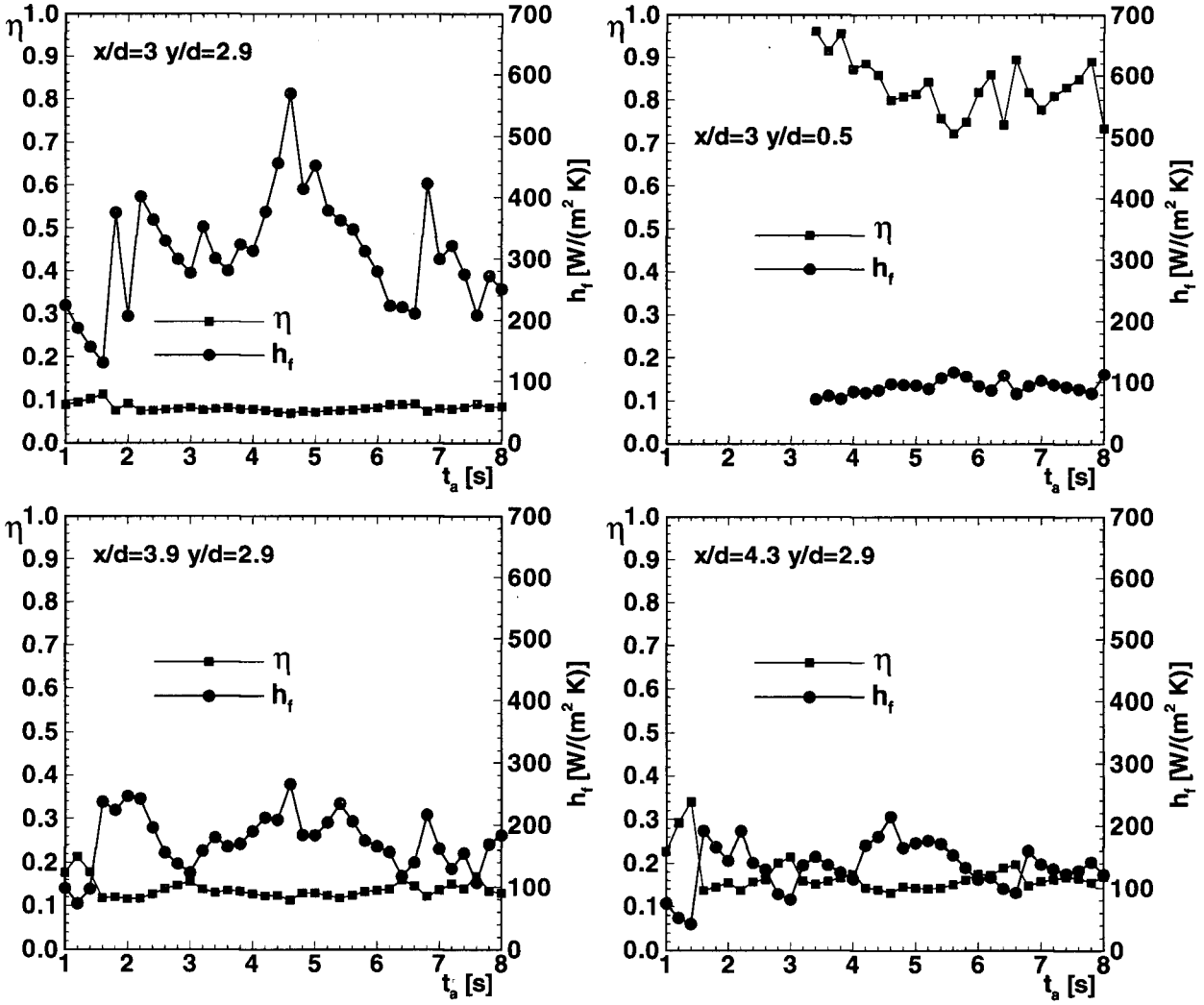


Figure 4.9: Time history of $h_f$ and $\eta$, M=1.0.

in Fig. 4.8, $x/d = 2$ and $x/d = 3$, a shift in the spanwise location of the jet is apparent. Within the experimental accuracy, the trends are nevertheless preserved as well as the peak $\eta$ values.

The best agreement is actually achieved at the streamwise location closest to the jet exit, $x/d = 1$, so that the region around the downstream duct exit corner is well represented by the one-dimensional formulation. This can be explained by the findings in [17], that the jet is mostly deflected towards the upstream side of the duct after negotiating the sharp corner at the duct entrance. This effect is more pronounced at higher mass flow ratios due to the increased vertical momentum of the jet, so that the region in the duct around the downstream exit corner is not immediately exposed to the jet flow.

For this case, the time history of $\eta$ and $h_f$ is shown in Fig. 4.9 at four arbitrary locations on the surface. No definite trend is present in the time variation of the two parameters, and the same conclusions presented for the M=0.5 case can be inferred here too regarding the lateral conduction effects and the choice of the time event pairs. Again, the use of the multiple sampling technique provides a better representation of the three-temperature situation. Overall, there is more scatter in the values of $h_f$ than in the values of $\eta$ except for the location $x/d = 3$ and $y/d = 0.5$. Film cooling effectiveness values appear to fluctuate more at lower values of $h_f$, as in the M=0.5 case. At some locations, the values of $\eta$ appear extremely stable although the scatter in the corresponding $h_f$ values is significant.

### 4.6.4 Mass Flow Ratio M=1.5

The last case used for comparison and validation is M=1.5, and spanwise distributions of $\eta$ at different streamwise locations are shown in Fig. 4.10. The FID results from [17] are again used for comparison. The agreement is good for this case too. The peak $\eta$ values and their location is also generally reproduced, and very good agreement is again achieved at the spanwise location immediately downstream of the duct exit as in the M=1.0 case. No data is produced by the liquid crystal technique at the streamwise $x/d = 8$ location. Not enough temperature change was observed at these points on the surface to attempt a solution, so a

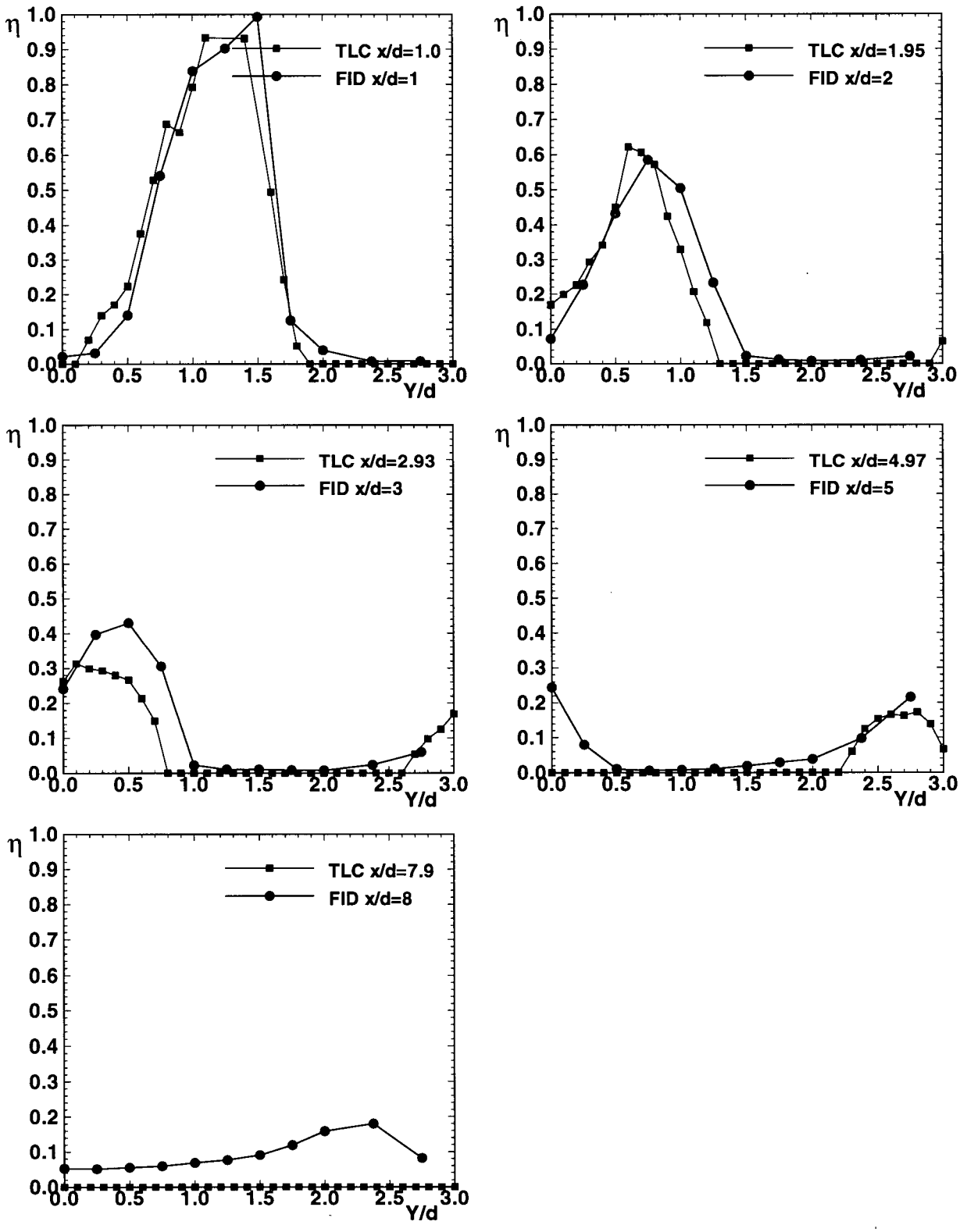


Figure 4.10: Comparison of $\eta$ obtained by the TLC technique with the FID data of Findlay [17], M=1.5.

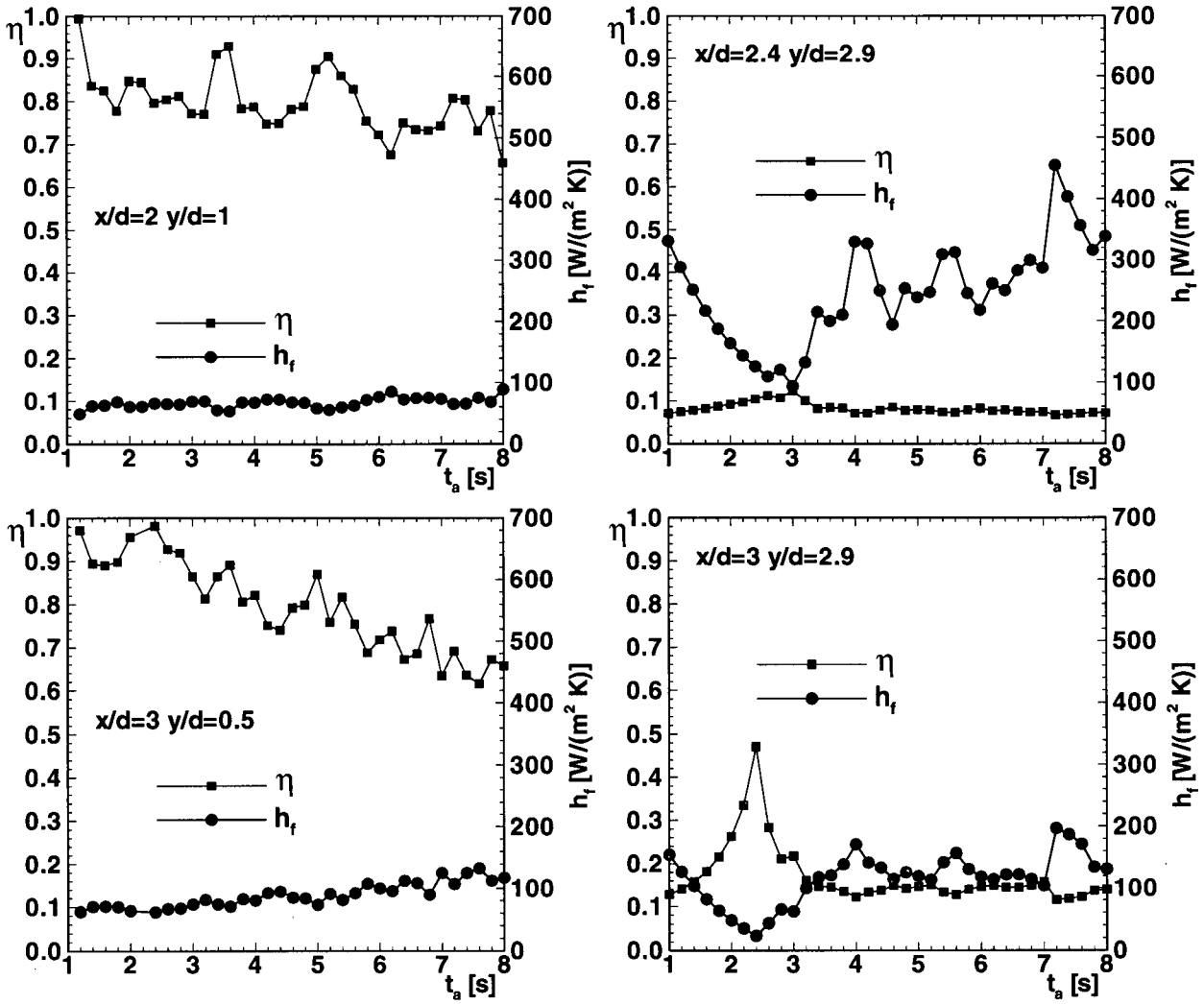


Figure 4.11: Time history of $h_f$ and $\eta$, M=1.5.

value of zero was assigned for all pixel cells in this situation ($\eta = 0$). A higher jet temperature would have been required to obtain a measurable temperature change farther downstream of the injection site when higher mass flow ratios are used and the jet is not immediately deflected towards the floor by the crossflow.

Time history data is shown in Fig. 4.11 at four arbitrarily sampled locations on the surface. No consistent trends are observed, so that the multiple sampling technique proves again to better represent the complicated three-dimensional flow field. The higher values of $h_f$ are also quite scattered while the corresponding $\eta$ values are quite stable. The lower values of $h_f$ seem to be more stable but the corresponding $\eta$ values then fluctuate more significantly.

## 4.7 Uncertainty Analysis

Two of the initial assumptions have yet to be verified, negligible effects due to buoyancy, and negligible radiation loss respectively. The buoyancy effects are considered negligible when $Gr/Re^2 << 1$ [46], where $Gr = gL^3(T_w - T_\infty)/(\nu^2 T_\infty)$ is the Grashof number for a perfect gas. The characteristic length $L$ is taken here to be the streamwise length of the liquid crystal instrumented patch, so that $L \approx 10d = 0.127$ m. The temperature of the surface varies, so that a measure of the maximum possible loss is obtained from the maximum recorded wall temperature $T_w \approx 30^0 C$. The temperature of the crossflow was around $T_\infty \approx 21.9^0 C$. Also, the minimum crossflow velocity is in the M=1.5 case, $U_\infty = 3.8$ m/s. This gives the ratio:

$$\frac{Gr}{Re_L^2} = \frac{gL(T_w - T_\infty)}{T_\infty U_\infty^2} = 0.0024 << 1 \tag{4.20}$$

so that the buoyancy effects can be neglected at the lowest crossflow velocity, and they are even less important at the higher crossflow velocity, or lower mass flow ratio.

The radiation exchange rate between the relatively small liquid crystal instrumented surface and its surroundings can be expressed per unit area as:

$$q_{rad} = \epsilon\sigma(T_w^4 - T_\infty^4) \tag{4.21}$$

where $\epsilon$ is the surface emissivity, and $\sigma = 5.67 \times 10^{-8}\mathrm{W/(m^2K^4)}$ is the Stefan-Boltzmann constant. It is difficult to appreciate the emissivity of the Plastic G/black paint/liquid crystal instrumented surface so that the maximum value $\epsilon = 1$ is used here (an estimated value of $\epsilon = 0.85$ was used in [4]). A direct comparison can be made with the values of $h_f$ when the radiation heat transfer coefficient $h_{rad}$ is employed:

$$h_{rad} = \epsilon\sigma(T_w + T_\infty)(T_w^2 + T_\infty^2) \tag{4.22}$$

The highest temperature of the surface, $T_w \approx 30^0C$, was recorded for the M=0.5 case at locations around $x/d = 1.5$ and $y/d = 0.8$. The values of the convective Stanton number at these locations are taken from Fig. 4.5 on page 122 to be around $St = 0.036$. A radiation Stanton number can be calculated based on $h_{rad}$ defined by Eqn. 4.22, so that:

$$St_{rad} = \frac{h_{rad}}{(\rho c_p U)_\infty} = 0.044 \times 10^{-2} \tag{4.23}$$

The radiation is therefore less than 1.2% of the forced convection heat transfer, and for most of the locations on the surface this value is actually much less since $T_w < 30^0C$.

This section is further addressing the sources of error in the determination of $h_f$ and $\eta$ by the liquid crystal thermography technique, in the investigated three-temperature situation. The goal here is to devise a method to estimate the errors in this complicated case, and to produce uncertainty maps for both $h_f$ and $\eta$. The methodology outlined in [1] will be followed whenever possible.

Three-temperature situations always require a minimum of two time events, with the corresponding surface temperatures, to calculate the two unknowns ($h_f$ and $\eta$) when the initial and gas temperatures are known. This produces two equations for two unknowns, different from a two-temperature situation when only one time event is required to calculate

the heat transfer coefficient if the initial temperature and the gas temperatures are known. For the two-temperature situation, the heat transfer coefficient is then directly calculated from Eqn. 4.6 by measuring the time it takes for the surface temperature ($T(z = 0, t)$) to reach a prescribed temperature that corresponds to the calibrated colour of a thermochromic liquid crystal. The two-temperature situation requires two time events if the initial surface temperature is unknown. This approach was first introduced by Jones [27] and the appropriate error analysis was addressed by Ireland and Jones [26]. The authors found the heat transfer coefficient to be extremely sensitive to the measured time ratio, and to small errors in a non-dimensional temperature, similar to that referred to in this study as $\bar{\Psi}$. Ireland and Jones estimated that a 3.3% uncertainty in this non-dimensional temperature ratio could produce an uncertainty in the calculated heat transfer coefficient of more than 22%. For a given test in their two-temperature situation, in which narrow band liquid crystals with fixed temperature sensitivities were used, the non-dimensional temperature was fixed but the time ratio varied with the location on the surface. Small errors in the measurement of this time ratio are also reported to produce large errors in the heat transfer coefficient, such that a solution was not actually possible everywhere on the surface. Ireland and Jones conclude their analysis of the so called *double crystal* method indicating that errors in the heat transfer coefficient could be substantially reduced by accurate measurement of the temperatures involved, and by appropriate choice of crystal temperatures.

In the present study, the time is known and the temperature information is correspondingly retrieved based on the recorded colour information, as needed. An initial time delay of no more than 0.033 s could be included to account for the scanning frequency of the NTSC video camera, and is constant for each test run. Such a time delay would only produce an absolute error in the time event ratio $t_a/t_b$ of less than 0.1% and no correction has been made for it. The use of a wide band liquid crystal for thermal mapping of the surface gives the flexibility of choosing the most suitable time event pair combination, and the corresponding non-dimensional temperature $\bar{\Psi}$, to minimize the errors in $h_f$ and $\eta$. The experimental uncertainty in the determination of the surface temperature was addressed in section 3.4 and

quantitative values are shown in Fig. 3.17 on page 101. The uncertainty is a function of the temperature of the surface and the average value of $\pm 0.155^0 C$ is further used in the analysis. The crossflow temperature is measured by a type K thermocouple connected to an OMEGA OMNI-CAL calibration unit so that its absolute value is known within $\pm 0.05^0 C$.

The uncertainty in $h_f$ is related to the uncertainty in the measured quantity $\bar{\Psi}$ and the choice of the time event pair, as shown in Fig. 4.3 on page 118. The closer the time event pair, the greater the uncertainty in $h_f$ especially at higher values of $h_f$. In fact, values of $h_f/\sqrt{\rho ck} > 1$ cannot be calculated with reasonable accuracy when the time events are close. To avoid overflow errors during the actual computations, and to implicitly reduce the error in the final results, an appropriate upper bound has to be set on $h_f$. This value could come from an error minimization procedure on the final results, and it was set here at $600\mathrm{W}/(\mathrm{m}^2\mathrm{K})$.

The highest computed value of $h_f$ still carries the largest uncertainty, while the lowest values of $h_f$ appear to be computed with the smallest uncertainty. An estimation of these uncertainty levels will be made for both $h_f$ and the associated $\eta$.

The uncertainty in $h_f$ due to the uncertainty in the measured value of $\bar{\Psi}$, for each time event pair, is calculated numerically from the corresponding variation on the $\bar{\Theta}$ curve at each time event pair. The slope of the $\bar{\Theta}$ curve, or $\tan\alpha$, determines the amplification factor on the uncertainty in $h_f$:

$$\frac{\Delta\bar{\Theta}}{\tan\alpha} = \frac{\Delta\bar{\Psi}}{\tan\alpha} = \Delta(h_f/\sqrt{\rho ck}) \tag{4.24}$$

at any location where a solution is possible, according to Eqn. 4.19 on page 120.

The uncertainty associated with the physical properties of the material used is estimated at $\delta\sqrt{\rho ck}/\sqrt{\rho ck} = \pm 2\%$. The bias errors in the temperature measurements are assumed to be totally correlated for each test run. The uncertainty in the non-dimensional temperature is calculated from the uncertainty in the measured temperatures, and propagates [1] through their functional relationship defined by Eqn. 4.16, so that:

$$\left(\frac{\delta\bar{\Psi}}{\bar{\Psi}}\right)^2 = \left(\frac{(T_w(t_b) - T_w(t_a))\delta T_\infty}{(T_w(t_a) - T_\infty)(T_w(t_b) - T_\infty)}\right)^2 + \left(\frac{\delta T_w(t_a)}{T_w(t_a) - T_\infty}\right)^2 + \left(\frac{\delta T_w(t_b)}{T_w(t_b) - T_\infty}\right)^2 \quad (4.25)$$

Equation 4.25 can be readily computed for each time event pair and for each pixel cell on the surface, to yield a new value of the heat transfer coefficient, $h_f/\sqrt{\rho ck}+\delta(h_f/\sqrt{\rho ck})$, and a new value of film cooling effectiveness, $\eta+\delta\eta$. This equation also shows that the uncertainty in the non-dimensional temperature is reduced if $T_w(t_b) >> T_\infty$, $T_w(t_a) >> T_\infty$, and if the two wall temperatures are close. This latter condition is contrary to the requirement that the two wall temperatures be well separated, as inferred from Fig. 4.3, a conclusion also reached in [26]. Minimum uncertainty in the results is then achieved when the three temperatures are in the relationship $T_w(t_b) > T_w(t_a) >> T_\infty$, and they are measured as accurately as possible.

The uncertainty in the physical properties of the material is accounted for, so that the uncertainty in $h_f$ is finally computed as:

$$\frac{\delta h_f}{h_f} = \sqrt{\left(\frac{\delta\sqrt{\rho ck}}{\sqrt{\rho ck}}\right)^2 + \left(\frac{\delta\bar{\Psi}}{\bar{\Psi}\tan\alpha}\right)^2} \quad (4.26)$$

and the uncertainty in $\eta$ is simply computed and reported as $\delta\eta/\eta$.

This procedure is repeated for each time event pair where a solution was initially obtained. Since the final results are computed as averages over the set of time event pairs, the associated uncertainty is calculated [1] and reported as:

$$\frac{\delta\eta}{\eta} = \sqrt{\frac{\sum_i^N (\frac{\delta\eta}{\eta})_i^2}{N}} \quad (4.27)$$

where $N$ is the number of time event pairs for which a solution was obtained. Detailed maps of the uncertainty associated with $\eta$ and $h_f$ are reproduced in Fig. 4.12, and Fig. 4.13 respectively.

For the M=0.5 case, the uncertainty in $\eta$ is less than 9.55% everywhere and is as good

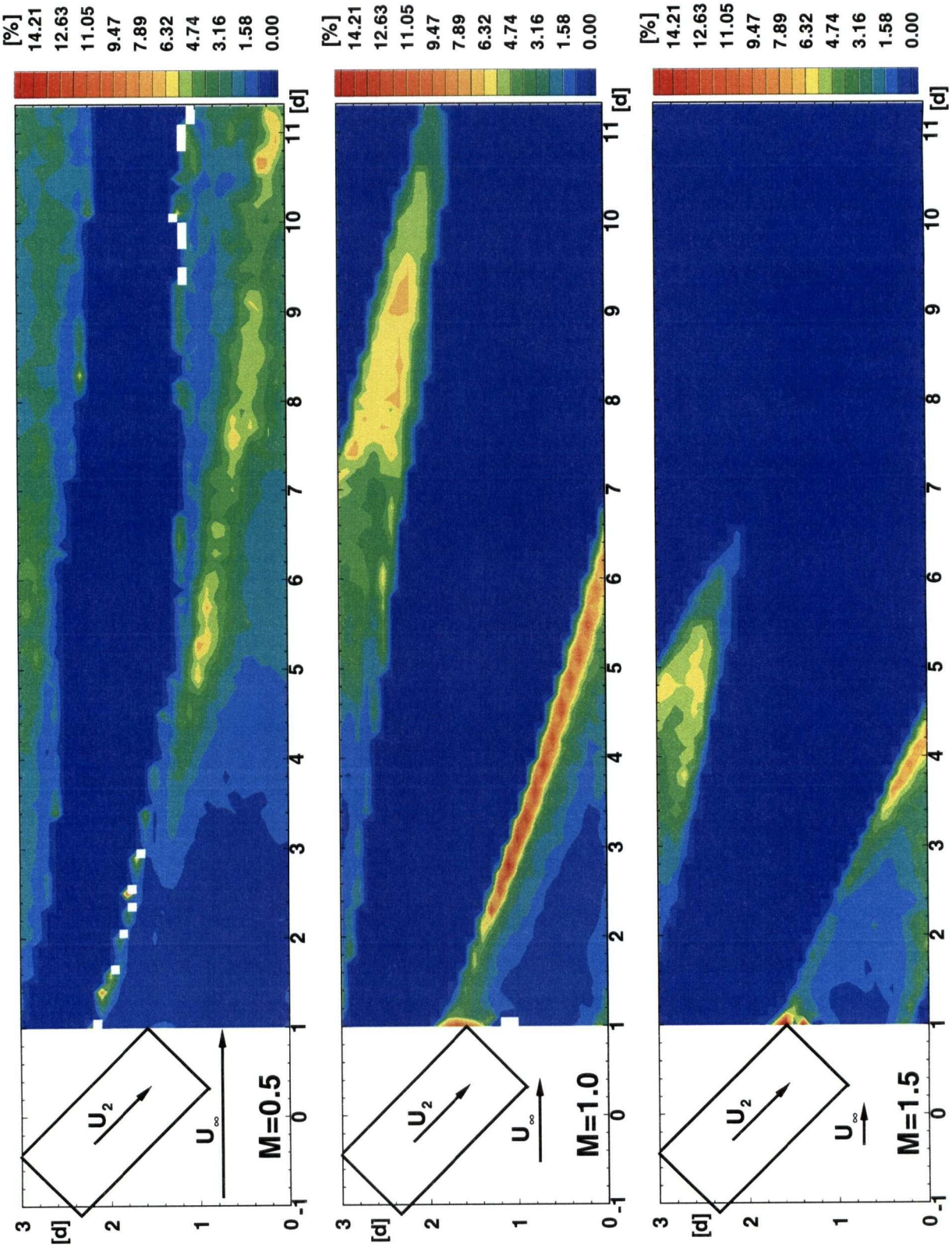


Figure 4.12: Map of the uncertainty in film cooling effectiveness data.

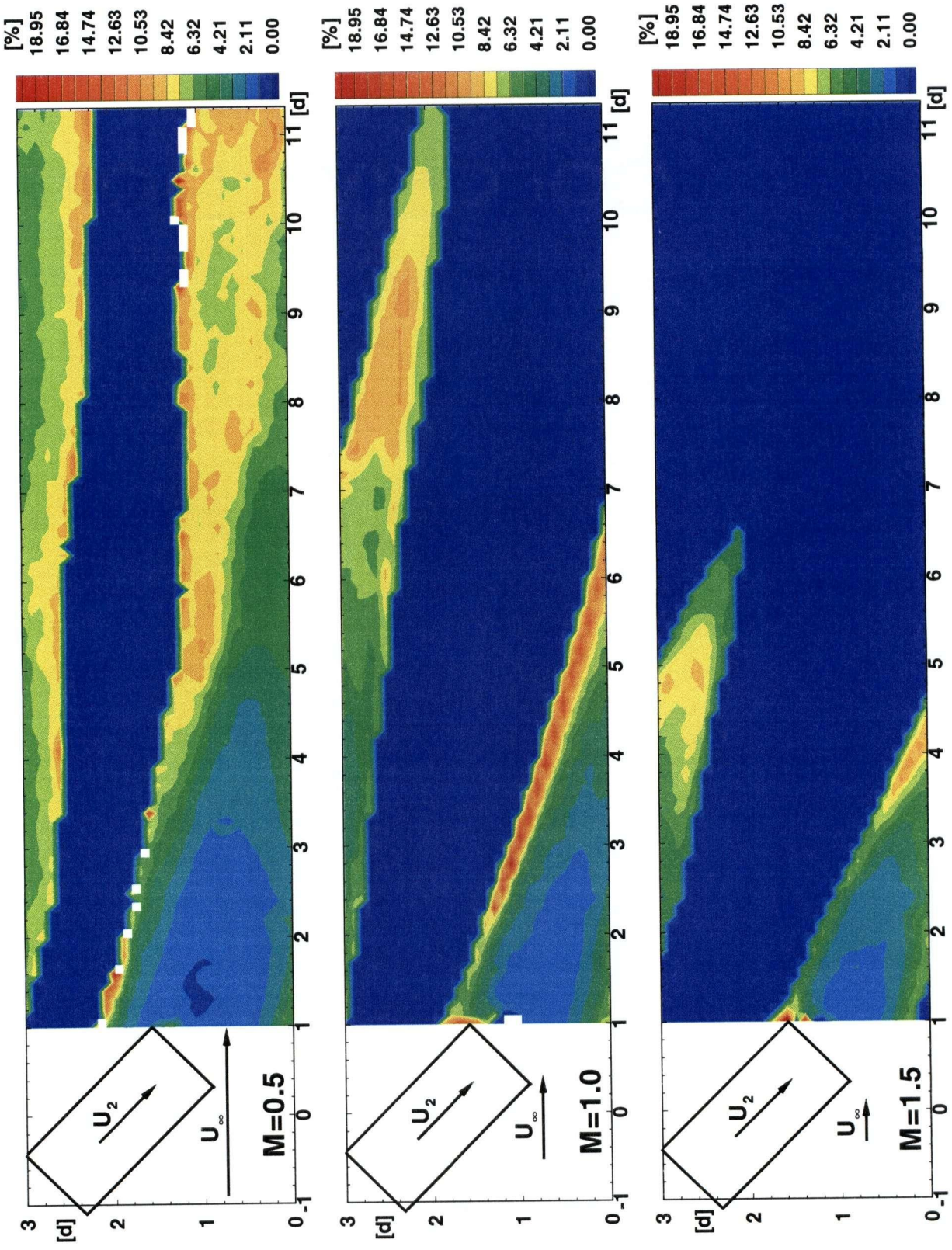


Figure 4.13: Map of the uncertainty in heat transfer coefficient data.

as 0.1%, and the uncertainty in $h_f$ is as high as 20.5% and as low as 1%, with typical values between 2% and 10%. For the M=1.0 case, the uncertainty in $\eta$ is as high as 15.2% towards one side of the jet, and is as low as 0.23%, with typical values between 1% and 7%. The uncertainty in $h_f$ is comparable with that in the M=0.5 case. For the M=1.5 case, the uncertainty in $\eta$ is less than 7% and that in $h_f$ is less than 10% everywhere but for a couple of cells around the downstream duct exit corner where the uncertainty runs as high as 21% for $\eta$ and 27% for $h_f$.

Overall, the uncertainty in $\eta$ is less than 7% and the uncertainty in $h_f$ is less than 10% everywhere except for small regions on the surface. The uncertainty in $\eta$ is also less than the corresponding uncertainty in $h_f$. The uncertainty in the results could be further reduced if a solution is kept only if its computed uncertainty is below some imposed levels, at selected time event pairs. The choice of the time event pairs could be also optimized according to the calculated uncertainty levels: even more time pairs could be considered when the uncertainty of the results is low, and only the time pairs that produce lower uncertainty values could be kept at higher $h_f$. The uncertainty in the time event averaged results could be then significantly improved, in particular for the regions with higher uncertainty levels identified in figures 4.12 and 4.13.

## 4.8 Summary

A complex three-temperature situation is present in compound angle square jets in crossflow. This particular geometry was used to validate a newly developed transient heat transfer technique based on wide-band liquid crystal thermography. The method allows for the simultaneous determination of the film heat transfer coefficient (defined by Eqn. 1.3 on page 10) and the film cooling effectiveness (defined by Eqn. 1.6). Available film cooling effectiveness data from [17] is used for comparison. The time scale and the sampling rates for the present investigation were different from the study in [17], and this might account for some of the differences in the reported results. Nevertheless, the film cooling effectiveness

data from the two methods is in very good agreement, and this provides confidence in the computed values of the film heat transfer coefficient obtained with the transient liquid crystal technique. The heat transfer coefficient is much more difficult to measure, especially in a complicated three-dimensional turbulent flow field, since it is inherently coupled with the flow and with the conditions in the boundary layer.

The solution algorithm for $\eta$ and $h_f$ was developed around the solution to the impulsive transient one-dimensional heat conduction response of a semi-infinite wall, subject to convective boundary conditions expressed by Eqn. 4.8 on page 107. The required change in the temperature of the surface is attempted by the use of heated jets. Since the change in the jet temperature is gradual, the total temperature change is obtained by superposition of incremental temperature steps. This approach has been also used in the past in single event sampling techniques.

The assumption that the surface is suddenly exposed to a uniform temperature field is the most problematic, since the temperature profile is not constant across the jets and the locations further downstream of the injection sites are not immediately exposed to this temperature field. In this situation, it appears to be more beneficial to suddenly change the temperature of the crossflow, such that the new thermal condition would be quickly convected downstream and in a more uniform fashion. The available hardware at the University of British Columbia does not allow for such an approach. Nevertheless, the use of a large scale model to ensure that the temperature pulse is contained well within the wall during the transients employed proved quite successful. With moderately heated jets, to justify the assumption of constant property flow and negligible buoyancy, the entire method provided accurate values of $\eta$ (and hence, by inference, of $h_f$) over almost all of the flow region examined ($x/d \leq 10$).

The novel approach in this study combines a real-time true colour imaging system for accurate colour rendition, with the use of a custom manufactured wide-band thermochromic liquid crystal and multiple event sampling for more accurate representation of $\eta$ and $h_f$. The

use of a wide-band thermochromic liquid crystal permits monitoring the temperature of the surface over the entire duration of the transients, and the multiple event sampling technique can be further optimized to provide improved accuracy of the results. This technique represents a significant improvement of the single event sampling procedure used in the past. Not only that the wide-band liquid crystal allows for all the information to be recorded during a single transient test, but the time history of $\eta$ and $h_f$ is available to provide a detailed representation of the heat transfer characteristics in complicated three-dimensional oscillating jets in crossflow.

The temperature of the surface is obtained from the high resolution, accurate true colour information, recorded in real-time with the use of a dedicated imaging system. This development was undertaken following the assessment of different other imaging systems, some of which (video tape recording for example) are often used in liquid crystal thermography. The present implementation uses the hue component from the RGB to HSL colour space transformation to directly quantify the corresponding temperature. Calibration of the wide-band liquid crystal over an even higher temperature range seems possible, and the use of different other colour transformations should be investigated in the future.

With all errors now minimized along the imaging system chain, the limiting factor in the accuracy of the surface temperature measurement becomes the uniformity and consistency of the liquid crystal layer. More advanced techniques and a specialized environment could be used to apply the liquid crystal in a thin layer on a variety of surfaces. A small improvement in the uncertainty of the surface temperature measurement proves extremely beneficial to the accuracy of the final results.

# Chapter 5

# Conclusions and Recommendations

## 5.1 Overall Summary

An investigation into the film cooling effectiveness of cylindrical leading edge geometries has been conducted. Two different existing cooling hole geometries were studied and they are referred to as the baseline geometry and the CA geometry respectively. A third leading edge geometry tested is referred to as the PVC geometry and represents an original design of an improved film cooling layout. In all cases the film cooling holes are disposed in four rows with two rows on each side of the geometrical leading edge. The holes are spaced at a certain spanwise distance apart in each row, and the holes in adjacent rows on either side of the geometrical leading edge are staggered with respect to each other, as well as about the geometrical leading edge.

Film cooling effectiveness measurements were made using a flame ionization detector technique and the mass/heat transfer analogy for fluids with constant properties. The effect of density differences between the cooling jets and the mainstream in an adiabatic heat transfer process was modelled by using either air or $CO_2$ as coolant gas in the analogous isothermal mass transfer process. The effect of mass flow ratio was examined for double and single row injection at a constant jet Reynolds number of approximately 4200 for all

cases. The effect of variable jet Reynolds number was studied for single row injection of the baseline geometry. These measurements give insight into the film cooling characteristics at the leading edge of turbine blades and provide new data for design purposes.

A film cooling effectiveness correlation was developed for the baseline geometry and double row injection with air and $CO_2$ as coolant gases based on an area-averaged film cooling effectiveness and on a newly defined blowing parameter. This correlation accounts implicitly for the specific geometrical layout of the baseline geometry and can be used in existing design procedures to estimate the minimum film cooling performance of this geometry under various operating conditions.

The development, implementation and validation of a transient heat transfer technique using wide-band TLC for thermal mapping were presented. Based on a comparison of different colour image capture techniques made in this study, a high performance imaging system was specified and implemented. Computer codes were also developed for processing and analysis of real-time true colour information recorded on a host PC's RAM.

Film cooling effectiveness and heat transfer coefficient were simultaneously calculated from one transient test using a multiple sampling technique to account in more detail for the surface time history. This approach has not been previously reported and is critical for the accurate calculation of the heat transfer characteristics in a typical film cooling application described by a complex turbulent three-dimensional flow field with large scale unsteadiness.

A flat plate film cooling geometry with compound angle jets was used for validation of the liquid crystal method by comparison of film cooling effectiveness data with the flame ionization data from Findlay [17]. The study in [17] uses a completely different technique based on flame ionization detector sampling in an isothermal mass transfer experiment. Such a direct comparison of fundamentally different experimental methods is difficult to find in the published literature. Very good agreement was achieved between the two sets of data

and represents a significant contribution of this thesis.

The new liquid crystal technique allows for accurate and cost effective assessment of both the heat transfer coefficient and the film cooling effectiveness in film cooling applications. The experimental costs are greatly reduced over more traditional heat transfer data acquisition methods, and the initial hardware and development costs can be quickly recovered. Post-processing of the recorded information provides a fast output of results, which allows for great flexibility in the research program. Extensive experimental investigation of the effect of various design parameters on the heat transfer characteristics of leading edge geometries is now within reach. The method can be applied in a variety of situations, such as the investigation of film cooling performance of different geometries, or for other industrial or more fundamental heat transfer research.

## 5.2 Leading Edge FID Measurements

### 5.2.1 Conclusions

The spanwise-averaged film cooling effectiveness ($\bar{\eta}$) was used to quantify the relative performance of the baseline geometry, the CA geometry, and the PVC geometry.

For the case of double row air injection and constant jet Reynolds number, $\bar{\eta}$ downstream of row $\theta_2$ of cooling holes typically decreased with increasing mass flow ratio. An exception was for the PVC geometry where $\bar{\eta}$ for $M = 0.8$ was slightly greater than $\bar{\eta}$ for $M = 0.6$ for the streamwise region from $x/(\pi D/4) = 0.58$ to $x/(\pi D/4) = 0.96$. Overall, $\bar{\eta}$ was significantly higher for the CA geometry than for the baseline geometry for all mass flow ratios investigated from $M = 0.5$ to $M = 1.2$. For mass flow ratios below $M = 0.8$, the CA geometry produced higher $\bar{\eta}$ than the PVC geometry, but for mass flow ratios above $M = 0.8$ the PVC geometry is superior. At the higher mass flow ratio $M = 1.4$ the PVC geometry still produces higher $\bar{\eta}$ than the baseline geometry at $M = 1.2$. These results prove that the

design goals set in the development of the PVC geometry have been achieved; a safe backflow margin can be kept by using higher coolant discharge while maintaining a relatively good film cooling effectiveness.

For the case of single row air injection at constant jet Reynolds number, measurements of $\bar{\eta}$ were made for the baseline and PVC geometries. The local mass flow ratio correlates the spanwise-averaged film cooling effectiveness reasonably well immediately downstream of rows placed at different angles from the stagnation line around the cylindrical leading edge. Nevertheless, for the same local mass flow ratios $\bar{\eta}$ was slightly higher immediately downstream of row $\theta_2$ of cooling holes (farthest from the stagnation line) than immediately downstream of row $\theta_1$ (closest to the stagnation line). The trends in the variation of $\bar{\eta}$ were similar for the two geometries where a peak $\bar{\eta}$ occured at around $M_\theta = 0.3$ and $\bar{\eta}$ further decreased with increasing local mass flow ratio. Farther from the cooling holes, for the baseline geometry, $\bar{\eta}$ was higher downstream of row $\theta_2$ than downstream of row $\theta_1$ of cooling holes.

For the case of $CO_2$ injection and constant jet Reynolds number, FID measurements of film cooling effectiveness were made for the baseline geometry. For the case of double row injection, $\bar{\eta}$ downstream of row $\theta_2$ of cooling holes decreased with increasing mass flow ratio from $M = 0.5$ to $M = 1.2$. The use of $CO_2$ coolant, whose density is about 1.5 times that of air, produced higher $\bar{\eta}$ than injection of air coolant for the same momentum flux ratios.

For the case of single row injection, $\bar{\eta}$ downstream of row $\theta_1$ of cooling holes was higher for $CO_2$ injection than for air injection for all local mass flux ratios used. Immediately downstream of row $\theta_2$ of cooling holes a peak $\bar{\eta}$ occured at a slightly lower local mass flux ratio for air injection than for $CO_2$ injection, but injection of $CO_2$ produced higher $\bar{\eta}$ for higher local mass flux ratios. Farther downstream of row $\theta_2$ of cooling holes, $\bar{\eta}$ was the same for air and $CO_2$ injection at lower local mass flux ratios, but $CO_2$ injection again produced higher $\bar{\eta}$ for higher local mass flux ratios.

For the baseline geometry with double row air and $CO_2$ injection at constant jet Reynolds number, the film cooling effectiveness data were correlated based on a newly defined blowing parameter ($\xi$) and an area-averaged film cooling effectiveness ($\bar{\bar{\eta}}$) which represents the minimum expected film cooling effectiveness for some region downstream of the cooling holes.

The effect of the jet Reynolds number on $\bar{\eta}$ was investigated for single row air injection at different mass flow ratios using the baseline geometry. Downstream of row $\theta_1$ of cooling holes, $\bar{\eta}$ decreased with increasing jet Reynolds number for the lowest mass flow ratio used, but no significant effect of the jet Reynolds number was further observed with increasing mass flow ratios. The effect of the jet Reynolds number was more significant immediately downstream of row $\theta_2$ of cooling holes where the peak $\bar{\eta}$ clearly decreased with increasing jet Reynolds number. The peak $\bar{\eta}$ occured at a lower mass flow ratio for the lowest jet Reynolds number used and at a higher mass flow ratio for the highest jet Reynolds number used. Overall, no significant effect of the jet Reynolds number was observed at higher mass flow ratios.

### 5.2.2 Recommendations

Recommendations for future work refer mainly to the PVC geometry. In the present layout, the PVC geometry produced higher spanwise-averaged film cooling effectiveness and better coverage than the baseline and CA geometries for higher mass flow ratios typical of those used in gas turbines.

1. The set of film cooling effectiveness data from air injection should be complemented by $CO_2$ injection data to simulate the use of jets cooler than the mainstream, modelling the real application more closely.

2. The new heat transfer technique based on liquid crystal thermography developed in this study should be applied to the PVC geometry to obtain the complete heat transfer

characteristics of this geometry. The measured film cooling effectiveness results from the heat transfer technique could be then compared directly with the measured results from the FID technique.

3. Further development of the PVC geometry should also be considered. The use of flared holes or other more complicated hole exit geometries should be investigated. The transient heat transfer technique developed in this study can be readily used on these geometries for detailed assessment of their heat transfer characteristics, namely the film cooling effectiveness and the heat transfer coefficient.

4. Correlations of film cooling effectiveness and heat transfer coefficient must be constructed for all cases so that the results could be used directly in existing design procedures.

## 5.3 Liquid Crystal Thermography

### 5.3.1 Conclusions

The transient heat transfer technique was tested in a three-temperature application using a flat plate with a row of square compound angle jets. This geometry was previously used in the FID study by Findlay [17]. Three different mass flow ratios of $M = 0.5$, 1.0, and 1.5 were investigated with a constant jet Reynolds number of around 5000. Detailed quantitative comparisons of spanwise film cooling effectiveness profiles were made for all mass flow ratios examined. Overall, the film cooling effectiveness calculated from the heat transfer experiments were in very good agreement with the film cooling effectiveness from the mass transfer experiments used in [17].

The best coverage was obtained for the lowest mass flow ratio investigated of $M = 0.5$ when the jet was deflected towards the floor by the crossflow, and the coverage deteriorated progressively with increasing mass flow ratio. A larger region of higher film cooling effective-

ness was present within the area covered by the jet for the lower mass flow ratio $M = 0.5$ than for the higher mass flow ratio $M = 1.5$. The film cooling effectiveness was higher for regions closer to the injection sites and decreased farther downstream of the cooling holes for all mass flow ratios used.

The Stanton number ($St$) based on the mainstream conditions was used to represent the variation of the heat transfer coefficient on the film cooled surface. Higher values of the Stanton number were present typically around the sides of the jet for all mass flow ratios tested. The highest Stanton number values occured for the mass flow ratio $M = 1.0$ on one side of the jet relatively close to the cooling holes and for the mass flow ratio $M = 1.5$ around the edges of the jet away from the injection sites. A relatively large region of lower Stanton number was present farther downstream of the cooling holes for the mass flow ratio $M = 0.5$. The region of lower Stanton number was significantly reduced for the mass flow ratio $M = 1.0$ and occured much closer to the injection sites.

For all mass flow ratios examined, the regions with highest film cooling effectiveness did not correspond to regions of lowest heat transfer coefficient, but the regions with lowest film cooling effectiveness (which occured on the sides of the jets) did correspond to regions of high heat transfer coefficient. The uncertainty associated with both film cooling effectiveness and heat transfer coefficient was typically higher at the sides of the jets farther away from the cooling holes.

### 5.3.2 Recommendations

A few recommendations for future work refer to further improvement of the transient heat transfer measuring technique and liquid crystal thermography.

1. A comparative assessment of different colour space transformations should be pursued to determine the optimum colour/temperature transformation to extend the useful calibration range of the liquid crystal. This analysis can be done on the present set

of calibration data by implementing various colour space transformations. The uncertainty levels and the useful calibration range can be determined based on the standard deviation values associated with a specific colour component as described in this study. This will allow for the efficient use of available very wide-band liquid crystal [60] in film cooling applications.

2. The use of higher image transfer rates should be considered for future experiments to capture the large scale unsteadiness present in typical applications of jets in crossflow in more detail. The implementation of higher image transfer rates is expected to be less costly in the near future considering the present fast improvement in computer imaging hardware.

3. The multiple event sampling technique developed in this study should be optimized to further reduce the uncertainty of the output heat transfer data. For example, computed results with associated high uncertainty levels and results that are not within a few standard deviations from the mean value could be discarded in the analysis based on selected confidence intervals.

4. The new measuring technique can be used for quick evaluation of different leading edge design configurations without the need for intermediate, and very expensive, rig testing. Modifications and subsequent developments of different geometries can be directly and immediately assessed.

# Appendix A

# Colour Space Conversion

**RGB to HSL** (Foley and VanDam)

max = maximum of RGB

min = minimum of RGB

l = (max + min) / 2

if max = min, S = 0, H = undefined

if l $\leq$ 0.5, S = (max - min)/(max + min)

else, S = (max - min)/(2 - max - min)

delta = max - min

if R = max, H = (G - B)/delta

if G = max, H = 2 + (B - R)/delta

if B = max, H = 4 + (R - G)/delta

H = H * 60

if H < 0, H = H + 360

**HSL to RGB** (Foley and VanDam)

if L $\leq$ 0.5, m2 = L * (1 + S)

else m2 = L + S - L * S

m2 = 2 * L - m2

```
    if S = 0 and H = undefined, R = G = B = L
    R = value(m1,m2,h + 120)
    G = value(m1,m2,H)
    B = value(m1,m2,h - 120)
where value(a,b,c) is the following function:
value(n1,n2,hue)
    if hue >360, hue = hue - 360
    else if hue <0, hue = hue + 360
    if hue <60, value = n1 + (n2 - n1) * hue / 60
        else if hue <180, value = n2
        else if hue <240, value = n1 + (n2 - n1) * (240 - hue) / 60
        else value = n1
return value
```

# Appendix B

# Wind Tunnel Setup

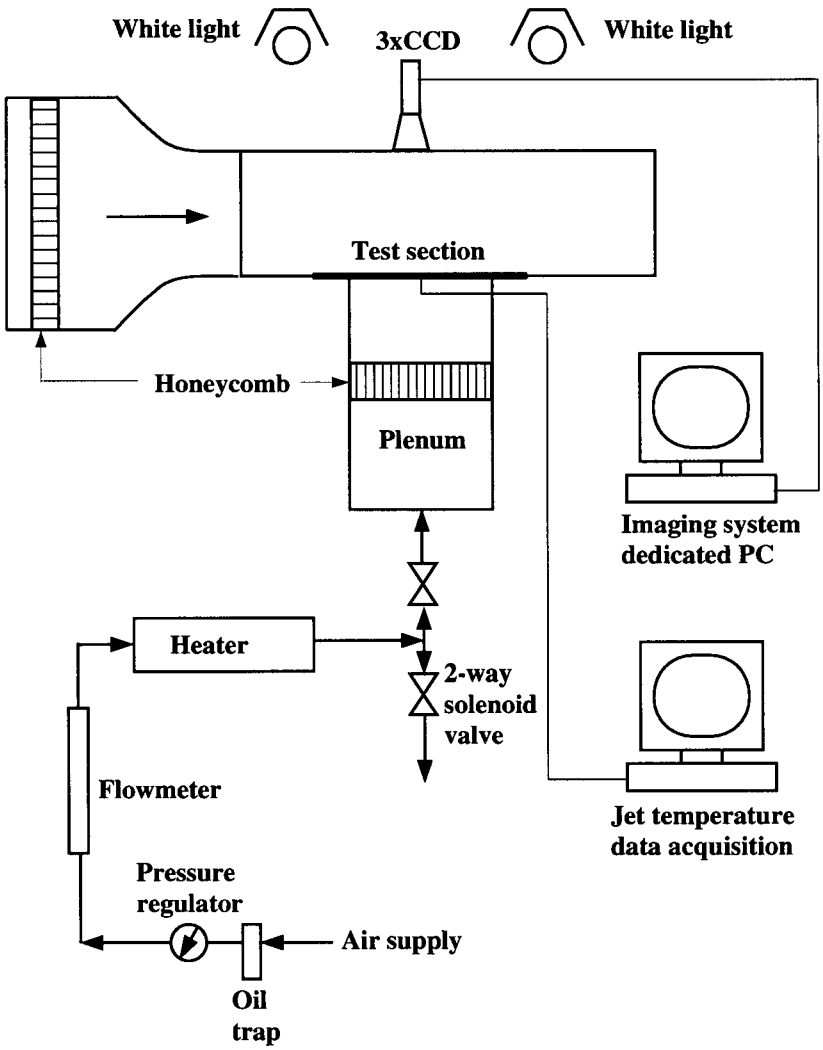

# Bibliography


[1] Abernethy R.B., Benedict R.P., Dowdell R.B., "ASME Measurement Uncertainty", June 1985, J. of Fluids Engineering, Vol.107, pp.161-163.

[2] Ajersch P., "Detailed Measurements on a Row of Jets in a Crossflow - With Applications", 1995, M.A.Sc. Thesis, Department of Mechanical Engineering, The University of British Columbia, Vancouver, BC, Canada.

[3] Aviation Week & Space Technology, December 1996.

[4] Butler R.J., Baughn J.W., "The Effect of the Thermal Boundary Condition on Transient Method Heat Transfer Measurements on a Flat Plate With a Laminar Boundary Layer", November 1996, J. of Heat Transfer, Vol.118, pp.831-837.

[5] Camci C., Kim K., Hippensteele S.A., "A New Hue Capturing Technique for the Quantitative Interpretation of Liquid Crystal Images Used in Convective Heat Transfer Studies", October 1992, J. of Turbomachinery, Vol.114, pp.765-775.

[6] Carslaw H.S., Jaeger J.C., "Conduction of Heat in Solids", 1959, Oxford University Press, 2nd edition.

[7] Chyu M.K., Yu Y., Ding H., Downs J.P., Soechting F.O., "Concavity Enhanced Heat Transfer In An Internal Cooling Passage", ASME Paper No. 97-GT-437.

[8] Clifford R.J., Jones T.V., Dunne S.T., "Techniques For Obtaining Detailed Heat Transfer Coefficient Measurements Within Gas Turbine Blade And Vane Cooling Passages", ASME Paper No. 83-GT-58.

[9] Collings P.J., "Liquid Crystals: Nature's Delicate Phase of Matter", 1990, Princeton University Press.

[10] Cumpsty N.A., "Jet Propulsion", 1997, Cambridge University Press.

[11] Eckert E.R.G., "Analysis of Film Cooling and Full-Coverage Film Cooling of Gas Turbine Blades", January 1984, J. of Engineering for Gas Turbines and Power, Vol.106, pp.206-213.

[12] Ekkad S.V., Zapata D., Han J.C., "Heat Transfer Coefficients Over A Flat Surface With Air and $CO_2$ Injection Through Compound Angle Holes Using A Transient Liquid Crystal Image Method", 1997, J. of Turbomachinery, Vol.119, pp.580-586.

[13] Ekkad S.V., Zapata D., Han J.C., "Film Effectiveness Over A Flat Surface With Air and $CO_2$ Injection Through Compound Angle Holes Using A Transient Liquid Crystal Image Method", 1997, J. of Turbomachinery, Vol.119, pp.587-593.

[14] El-Masri M.A., "On Thermodynamics of Gas Turbine Cycles: Part 2 - A Model for Expansion in Cooled Turbines", January 1986, J. of Engineering for Gas Turbines and Power, Vol.108, pp.151-159.

[15] Fackrell J.E., "A system for turbulent concentration measurements", 1978, J. Phys. E: Sci. Instrum., Vol.11, pp.1015-1022.

[16] Fackrell J.E., "A flame ionisation detector for measuring fluctuating concentration", 1980, J. Phys. E: Sci. Intrum., Vol.13, pp.888-893.

[17] Findlay M.J., "Experimental and Computational Investigation of Inclined Jets in a Crossflow", 1998, Ph.D. thesis, Department of Mechanical Engineering, The University of British Columbia, Vancouver, BC, Canada.

[18] Funazaki K., Koyabu E., Yamawaki S., "Effect of Periodic Wake Passing on Film Effectiveness of Inclined Discrete Cooling Holes Around the Leading Edge of a Blunt Body", January 1998, J. of Turbomachinery, Vol.120, pp.70-78.

[19] Goldstein R.J., "Film Cooling", 1971, Advances in Heat Transfer, Vol.7, pp.321-379.

[20] Goldstein S. editor, "Modern Developments in Fluid Mechanics", 1957, Vol.II, Oxford University Press, Amen House, London.

[21] Haven B.A., Kurosaka M., "Kidney and anti-kidney vortices in crossflow jets", 1997, J. of Fluid Mechanics, Vol.352, pp.27-64.

[22] Heiser B., May B., "U.S. Air Force Engine Management; a Cradle-to-Grave Process", 1996, Global Gas Turbine News, Vol.36, No.2.

[23] Hill P.G., Peterson C., "Mechanics and Thermodynamics of Propulsion", 1992, Addison-Wesley, 2nd edition.

[24] Hippensteele S.A., Russell L.M., Torres F.J., "Local Heat-Transfer Measurements on a Large Scale-Model Turbine Blade Airfoil Using a Composite of a Heater Element and Liquid Crystals", October 1985, J. of Engineering for Gas Turbines and Power, Vol.107, pp.953-960.

[25] Incropera F.P., DeWitt D.P., "Fundamentals of Heat and Mass Transfer", 1990, John Wiley & Sons, 3rd edition.

[26] Ireland P.T., Jones T.V., "Note On The Double Crystal Method Of Measuring Heat Transfer Coefficient", 1987, University of Oxford, Department of Engineering Science Report No.1710/87, Oxford, UK.

[27] Jones T.V., Hippensteele S.A., "High resolution heat transfer coefficient maps applicable to compound-curve surfaces using liquid crystal in a transient wind tunnel", 1987, Developments in Experimental Techniques in Heat Transfer and Combustion, HTD-Vol.71, ASME publication, New York.

[28] Lander R.D., Fish R.W., Suo M., "External Heat-Transfer Distribution on Film Cooled Turbine Vanes", October 1972, J. Aircraft, Vol.9, No.10, pp.707-714.

[29] Langston Lee, "Market Drivers for Electric Power Gas Turbines: Reasons for the Revolution", 1996, Global Gas Turbine News, Vol.36, No.3.

[30] Licu D.N., "PVC Geometry Specifications", 1997, Technical Communications to Pratt & Whitney Canada.

[31] Louis J.F., Hiraoka K., El-Masri M.A., "A Comparative Study Of The Influence Of Different Turbine Cooling On Gas Turbine Performance", ASME Paper No. 83-GT-180.

[32] Mehendale A.B., Han J.C., "Influence of High Mainstream Turbulence on Leading Edge Film Cooling Heat Transfer", October 1992, J. of Turbomachinery, Vol.114, pp.707-714.

[33] Meher-Homji C.B., "The Development of the Junkers Jumo 004B-The World's First Production Turbojet", October 1997, J. of Engineering for Gas Turbines and Power, Vol.119, pp.783-789.

[34] Meinders E.R., van der Meer Th.H., Hanjalic K., Lasance C.J.M., "Application of Infrared Thermography to the Evaluation of Local Convective Heat Transfer on Arrays of Cubical Protrusions", February 1997, Int. J. of Heat and Fluid Flow, Vol.18, No.1, pp.152-159.

[35] Metzger D.E., Carper H.J., Swank L.R., "Heat Transfer With Film Cooling Near Nontangential Injection Slots", April 1968, J. of Engineering for Power, pp.157-163.

[36] Metzger D.E., Larson D.E., "Use of Melting Point Surface Coatings for Local Convection Heat Transfer Measurements in Rectangular Channel Flows With 90-deg Turns", February 1986, J. of Heat Transfer, Vol.108, pp.48-54.

[37] Mick W.J., Mayle R.E., "Stagnation Film Cooling and Heat Transfer, Including Its Effect Within the Hole Pattern", January 1988, J. of Turbomachinery, Vol.110, pp.66-72.

[38] Ou S., Han J.C., "Influence of Mainstream Turbulence on Leading Edge Film Cooling Heat Transfer Through Two Rows of Inclined Film Slots", October 1992, J. of Turbomachinery, Vol.114, pp.724-733.

[39] Ou S., Mehendale A.B., Han J.C., "Influence of High Mainstream Turbulence on Leading Edge Film Cooling Heat Transfer: Effect of Film Hole Row Location", October 1992, J. of Turbomachinery, Vol.114, pp.716-723.

[40] Pimsner V., "Motoare Aeroreactoare", 1983, Editura Didactica si Pedagogica, Vol.1, romanian edition.

[41] Pitas I., "Digital Image Processing Algorithms", 1993, Prentice Hall.

[42] Pratt & Whitney Canada, "Private Communications", 1997.

[43] Russo C.J., "Changing The Landscape Of Civil Aviation", 1997, Global Gas Turbine News, Vol.37, No.3.

[44] Salcudean M., Gartshore I.S., Zhang K., McLean I., "An Experimental Study of Film Cooling Effectiveness Near the Leading Edge of a Turbine Blade", January 1994, J. of Turbomachinery, Vol.116, pp.71-79.

[45] Salcudean M., Gartshore I.S., Zhang K., Barnea Y., "Leading Edge Film Cooling Of A Turbine Blade Model Through Single And Double Row Injection: Effects of Coolant Density", ASME Paper No. 94-GT-2.

[46] Schlichting H., "Boundary-Layer Theory", 1979, McGraw-Hill Inc., 7th edition.

[47] Shadid J.N., Eckert E.R.G., "The Mass Transfer Analogy to Heat Transfer in Fluids With Temperature-Dependent Properties", January 1991, J. of Turbomachinery, Vol.113, pp.27-33.

[48] Taylor R.P., Coleman H.W., Hosni M.H., Love P.H., "Thermal boundary condition effects on heat transfer in the turbulent incompressible flat plate boundary layer", 1989, Int. J. of Heat Mass Transfer, Vol.32, No.6, pp.1165-1174.

[49] Utz P., "Today's video: equipment, setup, and production", 1992, Englewood Cliffs, Prentice Hall, N.J.

[50] Valenti M., "Upgrading Jet Turbine Technology", December 1995, Mechanical Engineering, pp.56-60.

[51] Vedula R.J., Metzger D.E., "A Method for the Simultaneous Determination of Local Effectiveness and Heat Transfer Distribution in Three-Temperature Convection Situations", 1991, ASME Paper No. 91-GT-345.

[52] von Wolfersdorf J., Hoecker R., Sattelmayer T., "A Hybrid Transient Step-Heating Heat Transfer Measurement Technique Using Heater Foils and Liquid-Crystal Thermography", May 1993, J. of Heat Transfer, Vol.115, pp.319-324.

[53] Wang Z., Ireland P.T., Jones T.V., Davenport R., "A Color Image Processing System for Transient Liquid Crystal Heat Transfer Experiments", July 1996, J. of Turbomachinery, Vol.118, pp.421-427.

[54] Wilde G.L., "The Design and Performance of High Temperature Turbines in Turbofan Engines", 1977, Tokyo Joint Gas Turbine Congress, pp.194-204.

[55] Wyszecki G., Stiles W.S., "Colour Science - Concepts and Methods, Quantitative Data and Formulae", 1982, John Wiley & Sons, 2nd edition.

[56] Source: Analog Devices Inc., http://www.analog.com/

[57] Source: Commission Internationale de L'Éclairage, http://www.cie.co.at/cie/

[58] Source: Duro-Test Lighting, http://www.durotest.com/

[59] Source: Truevision TGA File Format Specification, version 2.2, download from the FTP site at http://www.truevision.com/Support/

[60] Thermographic Measurements Ltd. - Thermax, Bank House, Neston Road, Burton, South Wirral L64 5TA, England; http://www.thermax.com; e-mail: tmc@thermax.com